Fatigue Assessment of Repaired Highway Bridge Welds Using Local Approaches

by

Kasra Ghahremani

A thesis

presented to the University of Waterloo

in fulfillment of the

thesis requirement for the degree of

Doctor of Philosophy

in

Civil Engineering

Waterloo, Ontario, Canada, 2015

Author's Declaration

I hereby declare that I am the sole author of this thesis. This is a true copy of the thesis, including any required final revisions, as accepted by my examiners.

I understand that my thesis may be made electronically available to the public.

Abstract

This thesis aims to address a number of unanswered questions regarding repair and fatigue design of welded joints in bridges, including developing and evaluating repair methods for enhancing the fatigue behaviour of web stiffeners in steel bridge girders, using local stress-based methods for evaluating the effectiveness of various repair methods and predicting the fatigue life of welded joints, and studying the effectiveness of high frequency mechanical impact (HFMI) treatments under actual in-service loading conditions in the long fatigue life regime. Along with extensive fatigue testing programs and finite element (FE) analyse studies, a strain based fracture mechanics (SBFM) model is used to predict the fatigue behaviour of repaired welds under realistic loading conditions. Through this research, a methodology is developed for generating structural stress design curves for retrofitted highway bridge welds based on small-scale fatigue experiments, relatively simple and inexpensive fatigue tests of smooth specimens, conventional static materials tests, and laboratory measurements.

The idea of retrofitting web stiffener ends in steel bridge girders susceptible to distortion-induced fatigue using adhesively-bonded fibre reinforced polymer (FRP) angles is introduced through this research. The proposed retrofit method is relatively cheap and easy to use and does not require deck removal or any other severe modification to the steel girder. Fatigue tests were conducted on specimens designed to model the conditions in the region between a web stiffener and a flange in a steel girder bridge. Fatigue life increases on the order of several hundred percent were achieved by implementing the proposed retrofit. A coarse FE analysis is used to predict the effectiveness of the proposed retrofit methods in terms of the reduction in the structural stress value.

A comprehensive variable amplitude (VA) fatigue testing program and analysis was performed to address a number of concerns raised regarding the use of impact treatments for the fatigue enhancement of welds in the high cycle (> 10 million cycles) domain. The test results are then used to evaluate a number of available recommendations for the fatigue design of impact treated welds. The nominal, structural, and effective notch stress approaches are considered.

An SBFM model was lastly used to predict the effectiveness of an HFMI treatment applied to welded details. The model is evaluated using the experimental results and found to be capable of predicting the fatigue lives for both the as-welded and impact treated specimens for all of the studied loading conditions. The idea of using the analytical structural stress *S-N* curves to predict the fatigue behaviour of welded joints with a similar load carrying condition welds was then explored.

Acknowledgements

I would like to offer my most sincere gratitude and appreciation to my invaluable supervisors, Prof. Scott Walbridge and Prof. Tim Topper. Their patience, support, guidance, and encouragement made my Ph.D. experience not only memorable, but also enjoyable. I am grateful for their exceptional mentorship and assistance throughout my graduate studies at the University of Waterloo. I was also privileged to have the support of Prof. Adil Al-Mayah, Prof. Gregory Glinka, and Prof. Lei Xu, whom I also had the honor to attend their classes, as my Ph.D. committee members. I would also like to thank Prof. Caroline Bennett for agreeing to be the external examiner for my Ph.D. defence.

I would like to thank Doug Hirst, Richard Morrison, and Rob Sluban from the Structures Laboratory for their technical assistance during the experimental phase of this research program. A sincere thanks also goes to Dr. Al Conle for his help and patience with the testing frame software (Flex 10). Mark Griffett, Rick Forgett, Rob Kraemer, and Mark Kuntz are also gratefully acknowledged for their assistance.

Studying at the University of Waterloo provided me with the opportunity to meet incredible friends and colleagues to whom I am thankful. In particular, I would like to thank my friendly and trustworthy officemates Dr. Mahdi Safa and Benjamin Dow. Jeremie Raimbault and James St.Onje are also thanked for their assistance with the microstructure imaging and weld toe geometry measurements. Dave Pow and Brett Kilgour at Pow Engineering are thanked for contributing the HFMI treatment of the specimens tested in this study.

The National Sciences and Engineering Research Council of Canada (NSERC) and the Ministry of Transportation of Ontario (MTO) are gratefully acknowledged for providing the financial support for this thesis program.

Foremost, I would like to thank God and my family for their unconditional love and constant support throughout my life. I wish to express my endless gratitude to my dearest parents for their continuous encouragement during my seven years of graduate studies in Waterloo. You taught me the value and pride associated with hard work and you made it possible for me to make it this far. My thanks are also due to my brother, Mahmoud, who has been a mentor for me since I can remember. I feel blessed to have you on my side and I appreciate all your support and advice. My heartiest thanks go to the best thing that ever happened to me, my beautiful wife Solmaz. I am grateful for your endless love and patience. I am a better person with you and am yet looking forward to better years to come!

Dedication

To my family

Table of Contents

List of Figures

List of Tables

Chapter 1

Introduction

1.1 Background and Motivations

With an increasing amount of traffic and natural aging, existing steel bridges are faced with serious durability problems. Fatigue is considered as one of the main sources of deterioration for steel bridges. Fatigue cracking can happen due to both in-plane forces and out-of-plane displacements (the latter is so-called distortion-induced fatigue). To overcome fatigue problems, different rehabilitation methods have been proposed and implemented during the last few decades, e.g.: hole drilling, reinforcing, grinding and rewelding, and using post-weld treatments, such as grinding, dressing, or peening.

Residual stress-based post-weld treatments, including conventional peening methods and high frequency mechanical impact (HFMI) treatments (see Figure 1.1) are attracting increasing attention as low cost and reliable methods for extending the fatigue lives of existing welded steel bridge structures. The primary mechanism by which this life extension is achieved is through the introduction of compressive residual stresses near the surface of the treated weld toe, which has the effect of slowing down the growth of small fatigue cracks. HFMI treatment effectiveness has been verified in numerous laboratory testing and analytical fatigue studies, as well as several field trials. For civil structures, where a considerable portion of the total applied stress is due to permanent loads, it is reported that peening should be particularly effective. Some concerns have been raised regarding the effectiveness of HFMI treatments under actual in-service loading conditions, as most of the reported test-based studies only demonstrate the performance improvement either under constant amplitude (CA) loading conditions or under variable amplitude (VA) loading spectrums in the short fatigue life domain.

The *S-N* curves provided in various standards and design codes are normally used for determining the fatigue life of new welded components, and are normally based on the nominal applied stress and the weld detail category. However, for complex or unconventional connection details, determination of the nominal stress and/or detail category can be difficult or even impossible. Moreover, for rehabilitated structures, in which both the geometry and the stress state in the welding area are changed, a method capable of accounting for these changes should be used. Alternative approaches such as fracture

mechanics and local strain-life methods have been developed to overcome these problems. However, these methods generally involve an intense computational effort. Other local approaches, which are attracting more attention recently, include the structural and effective notch stress approaches. The structural stress (sometimes called the hot-spot stress) approach accounts for the dimensions and stress concentrating effects of the detail at the potential crack initiation site and avoids the difficulties associated with the nominal stress approach. This approach has been used for existing bridge fatigue evaluation under traffic using the finite element method. However, few studies have used this approach until now to address the assessment of repaired welded joints.

The largest category of fatigue cracks observed in steel bridges are those caused by out-of-plane distortion [1]. Web gaps between stiffeners and girder flanges are the most common locations of these cracks (Figure 1.1). Estimating fatigue life for the distortion-induced fatigue problem is still a challenge as the *S-N* curves provided in different codes and standards cannot be used for web stiffener ends where neither a fatigue detail category nor a nominal stress are defined. Thus, another approach is needed for the fatigue analysis of those details. Different repair/rehabilitation methods have been proposed and implemented during the past few decades to overcome such fatigue problems. However, most of them require deck (in most cases concrete deck) removal and/or closing the traffic during implementation at the top girder flange. Moreover, the application of residual stress-based post-weld treatments for the retrofitting of web stiffeners in steel girder bridges is not well studied.

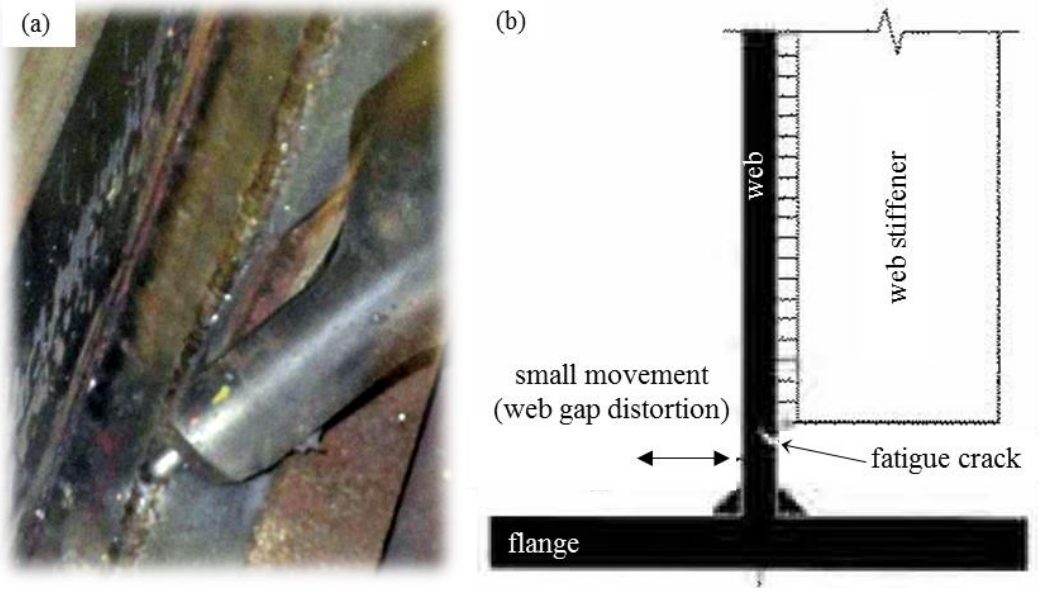

Figure 1.1: (a) HFMI treatment of a weld toe; (b) distortion-induced fatigue example [2]

Neither the nominal stress approach (sometimes called the classification method) nor the available local stress approaches provide precise information about crack size and crack growth in different stages of the structure's service life. Moreover, there are a number of fatigue rehabilitation methods, including HFMI treatments, which can only be fully understood by using analytical models that can account for all of the important parameters. A strain-based fracture mechanics (SBFM) approach can be used to account for non-linear material behaviour, which may be significant at the weld toe under high applied stress ranges. Thus, SBFM is suitable for considering the effects of the large overloads and underloads that may occur under in-service loading histories typical of bridges. Accurate SBFM modelling of fatigue crack growth, however, typically requires the determination of several material properties that cannot be obtained using conventional tests. In particular, the accurate modelling of crack closure effects, which play a key role in the variable amplitude loading behaviour of welds, is a challenging issue for a precise fracture mechanics analysis of the fatigue prone welded joints.

1.2 Research Objectives and Methodology

Based on the background presented in the preceding section, the research described in the current thesis was undertaken with the following objectives:

1) to evaluate the effectiveness of residual stress-based post-weld treatments for enhancing the fatigue behaviour of web stiffener ends in steel girder bridges;
2) to develop an alternative cost-effective and easy to implement repair method for distortion-induced fatigue damage, which does not involve deck removal;
3) to address concerns regarding the effectiveness of HFMI treatments under realistic in-service VA loading conditions in the long fatigue life domain (> 10 million cycles);
4) to use the local approaches (e.g. the structural and effective notch stress approaches) to evaluate the effectiveness of fatigue repairs and to predict the fatigue life of welded joints; and
5) to develop a methodology for obtaining or selecting suitable local stress design *S-N* curves from materials and small-scale testing for the fatigue analysis of welded joints.

To achieve these objectives, fatigue tests were designed and conducted at three different levels, namely: large- and small-scale weld details, and materials (smooth specimen) tests. The large-scale specimens were designed to model the conditions in the region between a web stiffener and a flange in a steel bridge girder. The small-scale specimens were designed to facilitate fatigue testing at very high frequencies of load carrying and non-load carrying welds in bridge structures. The smooth specimens

were used to derive the effective strain-life curve and the crack closure parameters for the structural steel that was used to fabricate the large- and small-scale specimens. The smooth specimen test results were validated by conducting crack growth measurements on compact tension (CT) specimens. The VA loading histories used in these fatigue tests were chosen to simulate the in-service traffic-induced loading that a typical bridge weld detail undergoes during its service life.

In conjunction with the conducted experimental research, the finite element (FE) method was used to obtain elastic stress distributions in the vicinity of the tested weld details analytically. A strain-based fracture mechanics (SBFM) analysis was then conducted using the derived material parameters and FE outputs and the analytical results were validated using the small-scale fatigue test results.

Using the investigated local stress approaches, the fracture mechanics analysis results are used to construct the structural and notch stress design *S-N* curves for the as-received and retrofitted weld details. These curves are then used to predict the results of the large-scale fatigue experiments. Based on the results of this research, *S-N* design curves for the fatigue analysis of treated welds are proposed, and recommendations are made concerning the use and limitations of these curves.

The benefits of using the experimental results to validate a fracture mechanics model and then using this model to establish or validate the local stress design curves, rather than simply using the test data to do this directly are worth noting at this stage. Briefly, the fracture mechanics model is a mechanistic model, rather than an empirical one, which means that once it is validated, it can be used with a higher level of confidence to extrapolate the test results to other loading histories and connection geometries. The model can also be used to better understand the behaviour of the weld specimens in the long life domain, where the test data is relatively sparse. This has significant implications in terms of the cost of the research, in comparison with the alternative of simply conducting many tests on large-scale weld details in both the medium and high cycle (> 10 million cycles) fatigue domains in order to validate an empirical model. The validated mechanistic model (the SBFM model, in this case) can also serve as a useful tool for better understanding the effects of the various model parameters on fatigue behaviour, since they can each be easily varied in the model to see the resulting effect.

Figure 1.2 provides a general description of the steps employed in this research project.

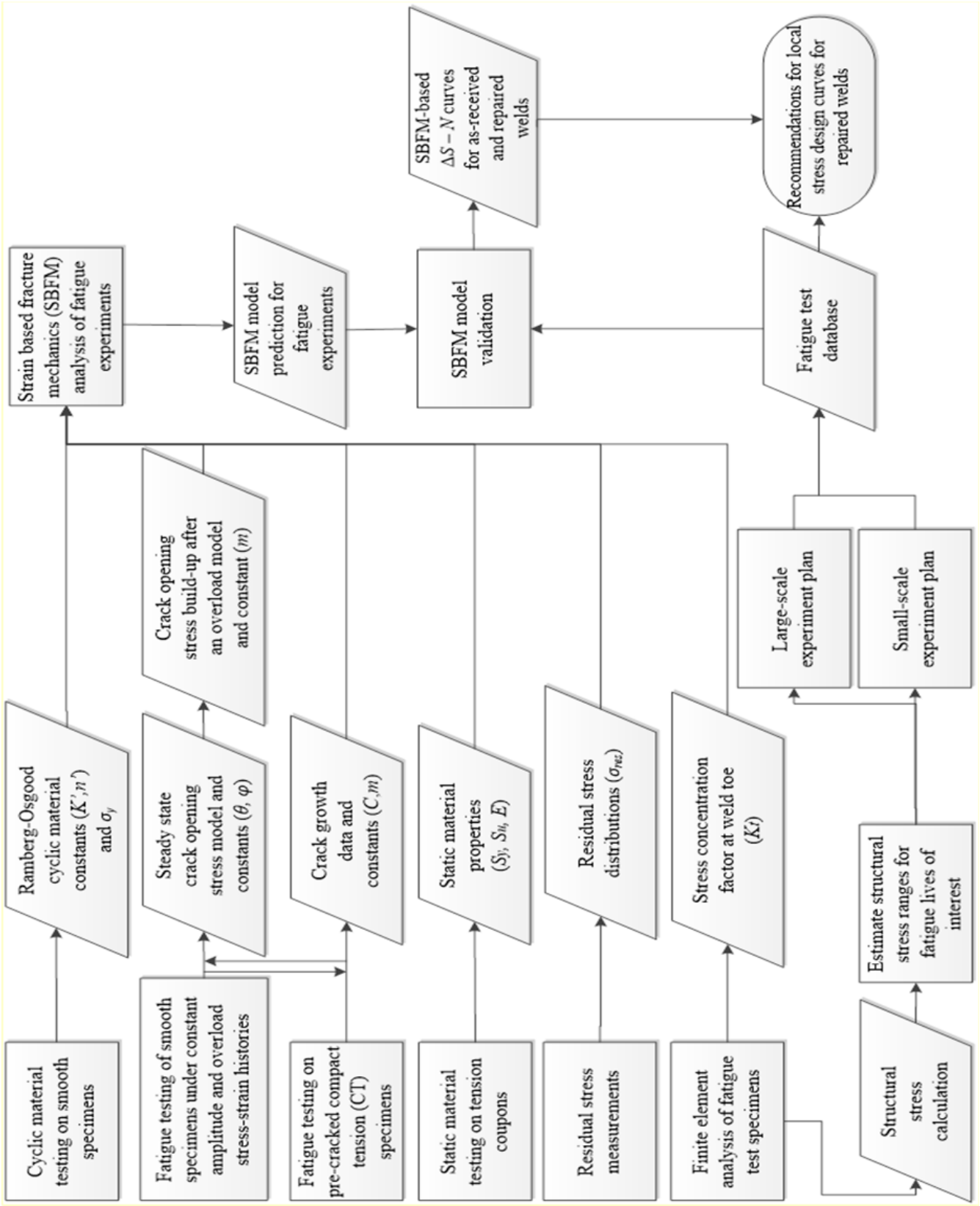

Figure 1.2: Steps employed to develop local stress design curves for repaired bridge welds

1.3 Scope

The fatigue tests for this study were conducted at the University of Waterloo (UW), using an MTS 322 Material Testing System with load capacity of 500 kN for large-scale specimens. A 100 kN MTS servo-controlled closed-loop electro-hydraulic testing machine with a process control computer controlled by a software developed at UW was used for small-scale and materials testing. The large-scale specimen represents a typical steel girder section built during 1970s in Ontario. The small-scale test specimen geometries include a load carrying lap joint and a stiffener detail, representing a non-load-carrying transverse web stiffener-to-flange connection in a bridge girder. All specimens were made from CSA 350W steel [3], which is a steel grade commonly used in Canadian bridges. The post-weld treatment methods investigated in this study include needle peening for the large-scale specimens, and HFMI treatment for the small-scale specimens. The weld treatments were applied following the procedure recommended by the International Institute of Welding (IIW), e.g. in [4, 5]. Other assumptions and calculations are based on the Canadian Highway Bridge Design Code [6].

1.4 Structure of the Thesis

This thesis is organized in six chapters. Chapter 2 summarizes the literature related to the distortion-induced fatigue problem in steel highway bridges and then presents the large-scale fatigue tests and FE analysis conducted within the scope of the current research project to investigate this problem. This chapter also describes and evaluates a novel repair method for this fatigue problem, which employs adhesively-bonded fibre reinforced polymer (FRP) stiffeners to reduce the local stresses at the stiffener end. The work in Chapter 2 appears in [7] and [8]. Chapter 3 summarizes the previous research on the effectiveness of residual stress-based post-weld treatments under VA loading conditions. The current design codes and specifications related to residual stress-based post-weld treatments are also discussed in this chapter. The small-scale fatigue tests are then described and the results are evaluated using two local stress approaches. Chapter 4 reviews the concept of crack closure and then presents the smooth specimen testing that was conducted to derive the fatigue crack closure and growth parameters. Residual stress measurements and weld toe geometry measurements are also presented in this chapter. This chapter also presents FE analyses performed to obtain the local stresses in the small-scale specimens. The SBFM model is described in Chapter 5. The validated model is then used to perform analyses under a wide range of in-service VA loading histories and to make design recommendations. Finally, in Chapter 6, the main findings and conclusions of this research are presented along with recommendations for future work in this field.

Chapter 2

Fatigue Testing and Finite Element Analysis of the Distortion-induced Fatigue Damage in Steel Girders

2.1 Introduction

The largest category of fatigue cracks observed in steel bridges are those caused by out-of-plane displacements [1]. Web gaps at web stiffener ends near the girder top flanges are the most common locations of these cracks. The top flange is held rigidly by the deck slab above, causing an abrupt change of stiffness and consequently a steep stress gradient. Distortion-induced fatigue is then caused by large secondary stresses in the weak web gap region between the top flange and the web stiffener. This problem can occur at non-load-carrying web stiffeners and at web stiffeners serving the dual role of stiffening the web and acting as a connection plate between the girder web and cross bracing. Different repair/rehabilitation methods have been proposed and implemented during the past few decades to overcome such fatigue problems, including reinforcing, hole drilling, grinding (and) rewelding, and the use of post-weld treatments (e.g. peening) [1-4]. Among these methods, reinforcement to create an alternative load path between the flange and web stiffener (or transverse connection plate) has been found to be highly effective in reducing the magnitude of the out-of-plane displacements, and consequently, mitigating distortion-induced fatigue damage [1, 5]. Connections between the reinforcement and the structure can be made by bolting. However, bolting or welding an angle to the stiffener and to the girder flange often requires removal of the deck (in most cases a concrete deck) and/or closing the ongoing traffic during implementation of the repair. Recently, a new angle-with-backing plate retrofit technique was developed as reported in [6], which does not require disturbance of the deck. However, distortion-induced fatigue damage often happens in locations that are not easily accessible for executing this retrofit approach. This highlights the need for an easy-to-implement and cost effective retrofit to inhibit fatigue cracking that does not require deck removal or access to the opposite side of the girder.

Fatigue assessment of repaired welded joints is another challenge in dealing with new and innovative retrofit methods. The classification method, which uses conventional S-N curves provided in different

standards and design codes, cannot be used for uncommon welded details or out-of-plane distortion fatigue problems where the nominal stress is difficult to characterize. Moreover, for rehabilitated structural details, in which both the geometry and the stress state in the weld area are changed, a more precise method capable of accounting for these changes should be used. The structural or hot-spot stress method is a promising one in this respect. The structural stress concept has been used previously to compare the efficiency of different retrofit techniques in reducing secondary stresses in the web gap regions [6]. Still, the potential of the structural stress method for predicting distortion-induced fatigue damage in steel bridges has not been fully explored. By establishing a fatigue class (or classes) for structural details susceptible to distortion-induced fatigue cracking, the corresponding structural *S-N* (design) curve can be used to estimate the fatigue life of those details. Moreover, the same design curve can be used to evaluate the effectiveness of different retrofit techniques in terms of reducing the magnitude of structural stress range at fatigue-critical locations. The structural stress range magnitude can be determined by direct (field) measurements, or by using a coarse finite element (FE) model following the procedures provided (for example) in [7].

Based on the background presented in the preceding paragraphs, the current study was undertaken with the goals of: 1) developing a cost-effective and easy-to-implement retrofit method for distortion-induced fatigue damage and evaluating its effectiveness, both analytically and experimentally, and 2) using the structural stress method to assess the fatigue capacity of both as-welded and retrofitted joints susceptible to distortion-induced fatigue damage.

2.2 Background

A major focus of the research on Fiber Reinforced Polymer (FRP) composites has been on strengthening concrete structures by various means, ranging from reinforcing concrete beams using FRP rebar to the confinement of concrete columns by using FRP wraps. FRP-strengthening of steel structures is not as common as for concrete structures because of steel's high elastic modulus and strength. Still, adhesively bonding FRP sections to steel has advantages that make this strengthening method attractive in a wide range of applications. Compared to welded steel plates, the use of adhesively-bonded FRP sections does not introduce unfavourable residual stresses and is less demanding in terms of heavy equipment requirements. A major focus of existing research in this field is enhancing the flexural capacity of steel beams by FRP strengthening. For example, Carbon Fiber Reinforced Polymer (CFRP) laminates were successfully used to strengthen steel composite beams in [8] and later to strengthen steel bridge sections

in [9]. In another popular retrofit method, bonded FRP plates are attached to the tension flange to strengthen steel girders [10, 11].

Fatigue retrofitting of steel members using FRP (non-prestressed or prestressed) under cyclic direct loading has also been studied and large fatigue life increases were observed. However, often this was for members with rivet holes or artificial notches [12, 13] where a significant fatigue life increase was easier to achieve with a minimal reinforcement of the structure. However, when applied to welded structures, FRP-retrofitting was found to be less efficient as reported in [14]. These less favourable results were related to high weld residual stresses and the fact that FRP was not much stiffer than steel. Recently, FRP overlay elements were also used to improve the fatigue performance of welded connections by increasing stiffness and reducing stress demand at fatigue-prone welds [15]. Increasing steel members buckling strength by using FRP-based retrofit techniques has also been studied [16-19]. Steel members and elements are typically very slender and a large benefit can be achieved with a relatively small change in the cross section properties. In [20], pultruded FRP sections were used to improve cross section properties and to inhibit local buckling in shear-controlled steel beams. Debonding has been found to be the most common failure mode in strengthened structures using this technique [21, 22]. Extensive research has been conducted on the bond behaviour of FRP strengthened steel sections and on failure behaviour of different adhesives, e.g. [23, 24].

In the current study, a retrofit method is proposed based on the idea of using FRP sections to solve a fatigue problem resulting from a lack of stiffness in a plate element. When applied to web stiffeners, a significant benefit can be achieved because a small change in the section properties at the location of the stiffener end can significantly influence local stress levels.

2.3 Fatigue Test Description

The specimen geometry employed in this study was designed to model the conditions in the region between the web stiffener and flange on a typical steel girder section built during the 1970s in Ontario, Canada (see Figure 2.1and Figure 2.2). The typical detail consisted of a 9.5 mm (3/8 in.) thick stiffener with a 50.8 mm (2 in.) web gap. The welds were specified as 4.8 mm (3/16 in.) fillet welds with no weld return at the stiffener end (see Figure 2.2). The specimen geometry and loading were designed to model the field conditions as realistically as possible, within constraints of time and budget appropriate for an initial or ‘proof of concept’ study. The specimens were designed with web gaps at each end (while there was only a web gap between the bottom flange and the stiffener in the original construction detail).

According to a preliminary, coarse FE analysis, loading one end at the proposed load levels has no significant effect on the web gap at the other end. This was also confirmed by direct measurements. Thus, two fatigue tests could be performed on a single specimen, significantly reducing the testing cost. All steel plates and stiffeners were fabricated from Canadian Standards Association (CSA) G40.21 350W steel. The specimens were fabricated using the FCAW (flux-cored arc welding) welding process.

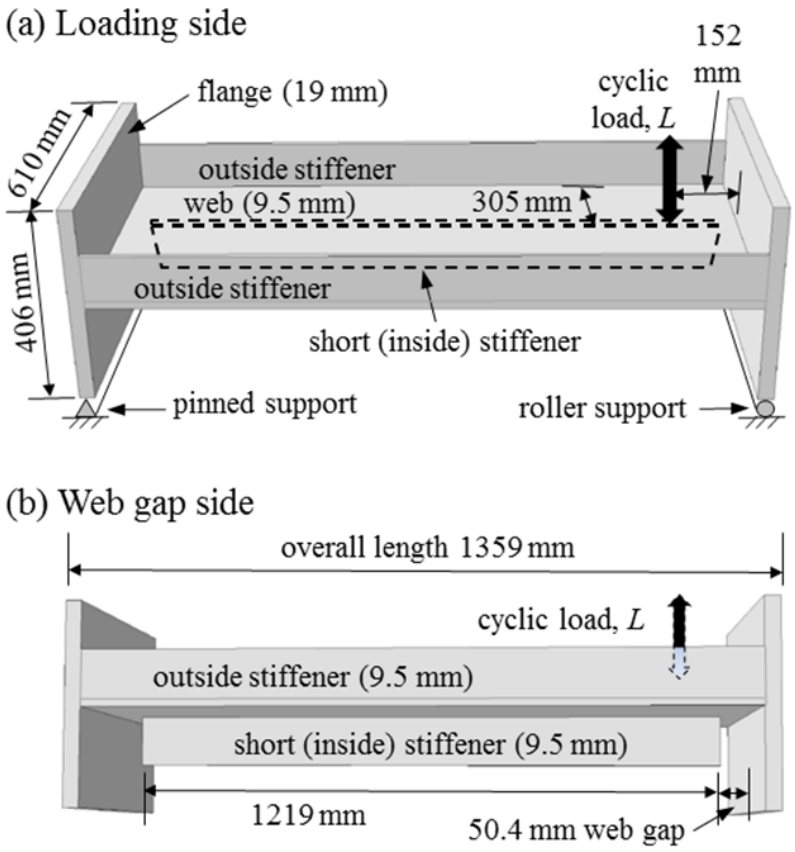

Figure 2.1: Fatigue test specimen: (a) loading side; (b) web gap side

Out-of-plane web gap movement was induced by the up and down movement of a jack, which was pushing against the specimen during testing (i.e. there were no load reversals). The loading was applied at a distance of 152 mm (6 in.) from the inside face of the near flange. Loading was applied using a custom-made ball bearing support. Using this system, the loading direction was always normal to the web, localized yielding was prevented, and the loading region was too far away from the crack location to undesirably affect crack growth. Displacement of the stiffener at a distance of 127 mm (5 in.) from the inside face of the near flange was measured by means of a direct-current differential transducer (DCDT) mounted under the specimen. Fatigue tests were performed at frequencies between 5 and 10

Hz, and strain data and displacements were recorded at 40 Hz. The tests were run until a through crack was detected on the opposite side of the specimen from where it initiated (i.e. the side where loading was applied).

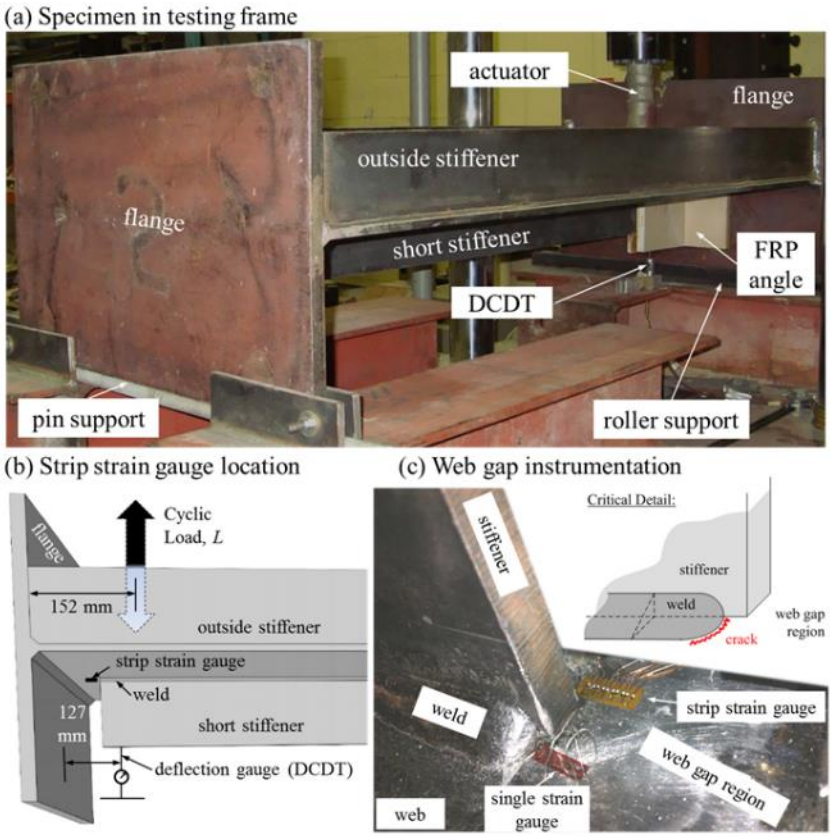

Figure 2.2: Fatigue test specimen and structural region instrumentation: (a) specimen in testing frame; (b) strip strain gauge location; (c) web gap instrumentation

To locate the fatigue critical locations, FE analysis with a relatively coarse mesh was again used. The stiffener weld toes on the web were found to be the most critical location for fatigue cracking, followed by the flange weld toe on the web on the opposite side of the stiffener. TML strip (QFXV-1-11-002LE) strain gauges were then attached to the specimen close to the weld toe on the web to measure the strain at multiple points during testing. Each strip gauge consisted of 5 strain gauges, each with a gauge length of 1 mm and a gauge pitch of 2 mm, lined up in the same direction to measure the surface strain normal to the weld toe. Two other TML single (FLA-5-11) strain gauges with a 5 mm gauge length were also attached close to the other stiffener weld toe on the web and to the flange weld toe on the web (see Figure 2.2).

To study the effect of loading spectrum, both constant amplitude (CA) and variable amplitude (VA) cyclic loading were considered. Tests were conducted under CA cyclic loading with a load ratio ($R = L_{min} / L_{max}$) of 0.1 and load ranges of 21, 28, and 35 kN. Tests were also conducted under VA cyclic loading at the same equivalent load ranges. The variable amplitude loading spectrum involved the repetition of 1000 cycle loading blocks, randomly extracted from a larger in-service loading history for the mid-span moment in a 40 m long, simply-supported girder. This loading history was generated using traffic data from Ontario, Canada obtained from a survey of truck axle spacings and loads conducted in 1995 with total number of 10198 trucks, as explained in [25]. Miner's sum was used to calculate the equivalent load range for the VA tests, assuming a slope of $m = 3$ for the design S-N curve (see Figure 2.3 and Table 2.1).

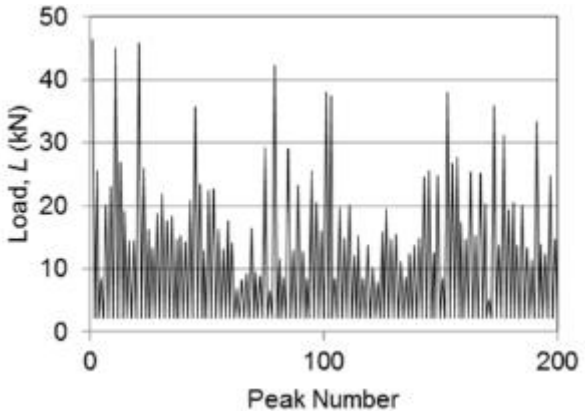

Figure 2.3: Sample from variable amplitude (VA) loading history

Table 2.1: Fatigue loading cases

Loading Type	Max. Load (kN)	Min. Load (kN)	Equivalent Load Range (kN)	Symbol
Constant Amplitude	23.3	2.3	21	C21
Constant Amplitude	31.1	3.1	28	C28
Constant Amplitude	38.8	3.8	35	C35
Variable Amplitude	46.4	2.3	21	V21
Variable Amplitude	63.2	3.1	28	V28
Variable Amplitude	78.9	3.8	35	V35

Fatigue testing in this study was conducted in three phases. Ten fatigue tests were conducted in the first phase including six tests on as-welded (AW) specimens and four tests on specimens retrofitted by needle peening (NP). Four fatigue tests were conducted in the second phase where cracked specimens were repaired using a conventional grinding-and-rewelding (GR) repair method. The procedure used in this

study is a modified version of the specification used by CN (Canadian National) Railway as follows: 1) preheat the base metal to 150°F, 2) gouge the crack from one side by grinding to approximately one half of the plate thickness, 3) clean the groove by rotary disc grinding, completing the required groove radius of 3/8" and angle of 20°, 4) after cooling, perform a visual inspection of the groove and groove edges. 5) preheat the base metal in the crack area to 250°F before welding, 6) complete root, intermediate, and final weld passes with a visual inspection upon completion of each pass, 7) remove slag inclusions after each pass, and 8) repeat process for the other side. Needle peening treatment was performed using a compressed air needle gun and following the procedure in [26]. All of the welding was performed by the same certified welder at the University of Waterloo's Engineering Machine Shop.

In the third phase of fatigue testing, nine cracked specimens were repaired using adhesively-bonded FRP angles and then cyclically loaded until further crack propagation was detected. Two more uncracked specimens were also reinforced in this phase using adhesively-bonded Glass Fiber Reinforced Polymer (GFRP) angles and fatigue tested until a through crack was detected. Table 2.2 presents the sequence and naming scheme for all fatigue tests conducted in this study.

Table 2.2: Sequence and ID of fatigue experiments on each specimen

Specimen	1st Test	2nd Test	3rd Test	4th Test	5th Test
1/A	AW-C35-1A	GRNP-C35-1A	FRP-1-C21-1A		
1/B	AW-C35-1B	GRNP-C21-1B	FRP-2-C21-1B	FRP-2-C28-1B	FRP-2-C35-1B
2/A	NP-C35-2A	GRNP-V21-2A	FRP-3-V21-2A		
2/B	AW-V35-2B	GR-C21-2B	FRP-4-C35-2B	FRP-4-V21-2B	
3/A	NP-V35-3A	FRP-5-V21-3A	FRP-5-V35-3A		
3/B	AW-C21-3B	FRP-5-V28-3B			
4/A	NP-C21-4A				
4/B	AW-V21-4B				
5/A	NP-V21-5A	FRP-6-V28-5A			
5/B	AW-C28-5B	FRP-6-V35-5B			
6/A	FRP-5-V28-6AU				
6/B	FRP-5-V21-6BU	FRP-5-V35-6BU			

Naming convention: retrofit method-loading case-specimen (see Table 2.1 for loading case). AW: as-welded, NP: needle peened, GR: gouged-and-rewelded, GRNP: gouged-rewelded and needle peened, FRP-#: FRP angle-adhesive combinations (see Table 2.5).

2.4 FRP Angle Retrofit Method

Considering anisotropic mechanical properties of FRP structural shapes, these sections are particularly strong and useful when they are subjected to loadings along their fiber orientation or lengthwise (LW)

direction. However, when subjected to a rather complicated loading case, such as the loading that an attached angle experiences in a distortion fatigue retrofit, sectional crosswise (CW) mechanical properties should be considered. In this study, FRP angles were cut from off the shelf glass fiber reinforced polymer (GFRP) I-beam sections. Pultruded Dynaform® Isophthalic Polyester Fire Retardant (ISOFR) Resin and Vinyl Ester Fire Retardant (VEFR) Resin fiberglass structural shapes were donated by Fibergrate Composite Structures Inc., Canada. These products were chosen because of their fairly high crosswise (CW) mechanical properties (see Table 2.3). The FRP angles were cut from a large wide flange beam. Two angles were then attached to the specimen's stiffener and flange using a structural adhesive, after roughening the bonding surfaces on both the FRP angles and the specimen using a compressed air needle gun and sand blasting, respectively.

Table 2.3: Mechanical properties of the GFRP angles

Mechanical Properties*	Direction	Units	Nominal Value*	Tension Coupon Test Results†
Tensile Strength	LW	MPa	206	350
	CW	MPa	48	48
Tensile Modulus	LW	GPa	17.2	24.7
	CW	GPa	5.5	9.0
Flexural Strength	LW	MPa	206	
	CW	MPa	68	
Flexural Modulus	LW	GPa	12.4	
	CW	GPa	5.5	

* as reported in the product data sheet [27]
† based on average of two tension coupon tests

Two types of structural adhesive were studied: a high strength, high modulus adhesive (Sika AnchorFix-3^{CA}) and a low strength, highly ductile structural methacrylate adhesive (SikaFast®-3131). Mechanical properties of these two adhesive types are summarized in Table 2.4. As instructed in the product data sheets [28,29], the adhesive was applied using a pneumatic dispense gun to both components and the bonded surfaces were then firmly clamped into place for a day, until the adhesive fully cured at room temperature. Figure 2.4 shows a retrofitted specimen. The FRP-retrofitted specimens were continuously inspected for further crack propagation on the loading side and for FRP / adhesive failure during fatigue testing.

Table 2.4: Mechanical properties of the adhesives [28, 29]

Mechanical Properties	Units	AnchorFix-3[CA]	SikaFast-3131
Bond strength	MPa	20	Not provided
Strength	MPa	75[1]	8.9[2]
Modulus	GPa	3.6[1]	0.1[2]
Elongation at break	%	1	50
Service temperature range	°C	Not provided	-29 to 85

[1] reported as compressive strength and compressive modulus in product datasheet
[2] reported as tensile strength and tensile modulus in product datasheet

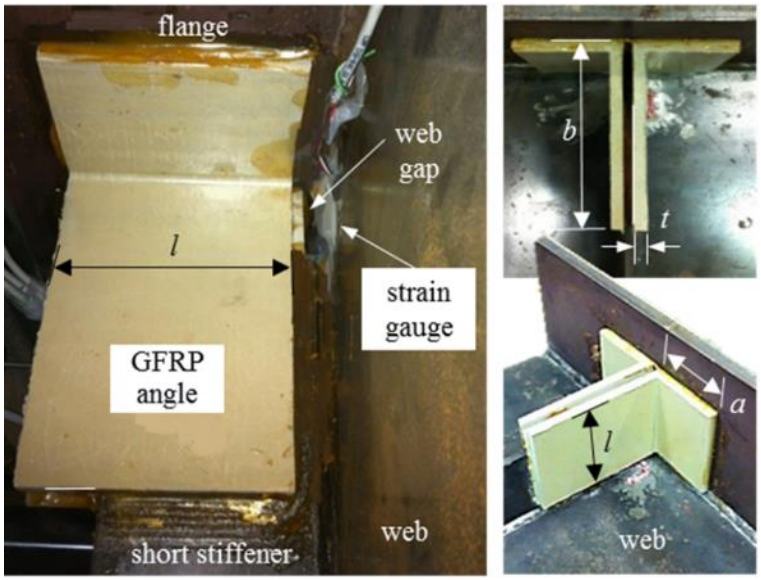

Figure 2.4: FRP-retrofitted test specimen

In absence of any comparative data, a trial-and-error development process was used to evaluate the effect of different parameters, both geometrical and mechanical, on the performance of the proposed retrofit. Within this process, a total of 7 fatigue tests were conducted on previously cracked specimens (Specimens 1 and 2). Initially, a dye penetrant was used to locate both surface and through cracks and specimens were then retrofitted using FRP angles. The marked cracked regions were then continuously monitored as the fatigue testing was continued. Fatigue loading was discontinued upon the detection of any signs of failure including: further crack propagation, failure in the FRP angle, evidence of adhesive debonding, or any increase in the maximum value of the measured out-of-plane displacement (Figure 2.5). Where no sign of failure was detected after 3 million cycles, loading was discontinued and a new test under a higher (more damaging) loading condition was started on the same specimen. Four different FRP-based retrofits were tested during this process (FRP-1 to 4 – see Table 2.5). Based on this process,

the retrofit FRP-5 was used to retrofit four stiffener ends: two initially uncracked (5/A and 5/B) and two cracked (3/A and 3/B). Considering the FRP-5 retrofit as a benchmark, another retrofit was tested to evaluate the effect of increasing the thickness of the FRP angles (FRP-6 retrofit). All of these FRP retrofits (angle-adhesive combinations) are summarized in Table 2.5.

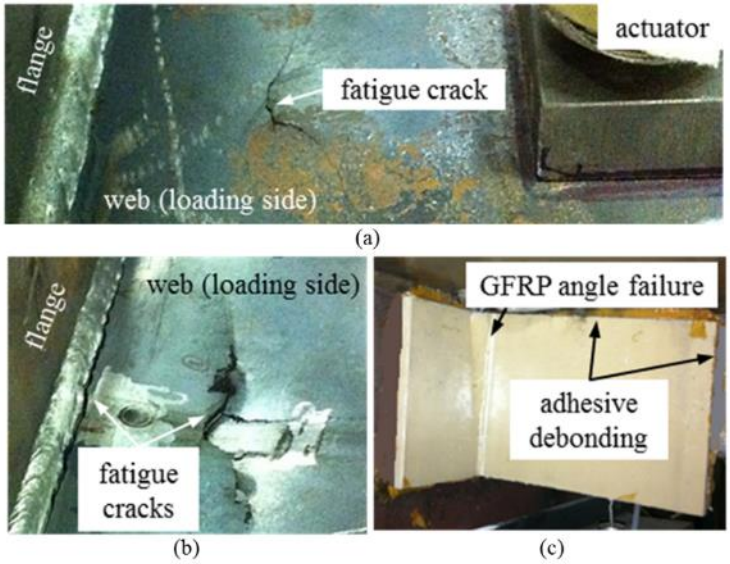

Figure 2.5: A typical detected through crack (a), propagated through cracks at the stiffener weld toe and the flange weld toe on the web (b), and FRP retrofit failure (c)

Table 2.5: FRP angle-adhesive combinations (also see Figure 2.4)

	FRP angle dimensions (all dimensions in mm)				
ID	*l*	*a* × *b*	*t*	Resin	Adhesive
FRP-1	102	79 × 140	6.4	ISOFR	AnchorFix
FRP-2	102	107 × 191	9.5	ISOFR	AnchorFix
FRP-3	102	107 × 191	9.5	ISOFR	SikaFast
FRP-4	102	107 × 191	9.5	VEFR	SikaFast
FRP-5	127	107 × 191	9.5	VEFR	SikaFast
FRP-6	127	107 × 191	12.7	VEFR	SikaFast

underline: changed parameter for each FRP retrofit compared to previous FRP retrofit

2.5 Fatigue Test Results

2.5.1 Fatigue Life Data

Fatigue lives (*N*), failure modes, structural stress (*HSS*) and displacement (*d*) ranges for all fatigue tests conducted in this study are presented in Table 2.6. Measured ranges at the equivalent load range are

reported for VA tests. These results are discussed in two different categories: fatigue tests on initially uncracked specimens, followed by the tests on cracked specimens.

Figure 2.6 presents all 16 fatigue tests conducted on initially uncracked specimens, including as-welded specimens, repaired specimens using conventional methods (i.e. needle peening and gouging-and-rewelding), and FRP-retrofitted specimens. As reported in [4], needle peening resulted in only a modest fatigue life increase within the tested load ranges, and the gouged-and-rewelded specimens generally had shorter fatigue lives than the as-welded specimens. The FRP-retrofitted specimens, however, had fatigue lives on the order of several hundred percent longer in many cases. As Figure 2.6 shows, a more than a 400% increase in the fatigue life was achieved in Test 15 (initially uncracked specimen, FRP-5 retrofit, V28 loading) compared to the average fatigue life curve for as-welded specimens at the same loading level. Under V21 loading with an average as-welded fatigue life of under half a million cycles, no failure was detected for Test 16 after 3 million cycles, when loading was discontinued. A second test (Test 17) was conducted on Specimen 6B by increasing the loading to V35 loading. A failure in the GFRP angles was subsequently observed after 20,000 cycles, followed by a through crack detection after a total of 80,000 load cycles. This test result is not shown in Figure 2.6 due to the mixed mode of failure, which makes it different than the other tests.

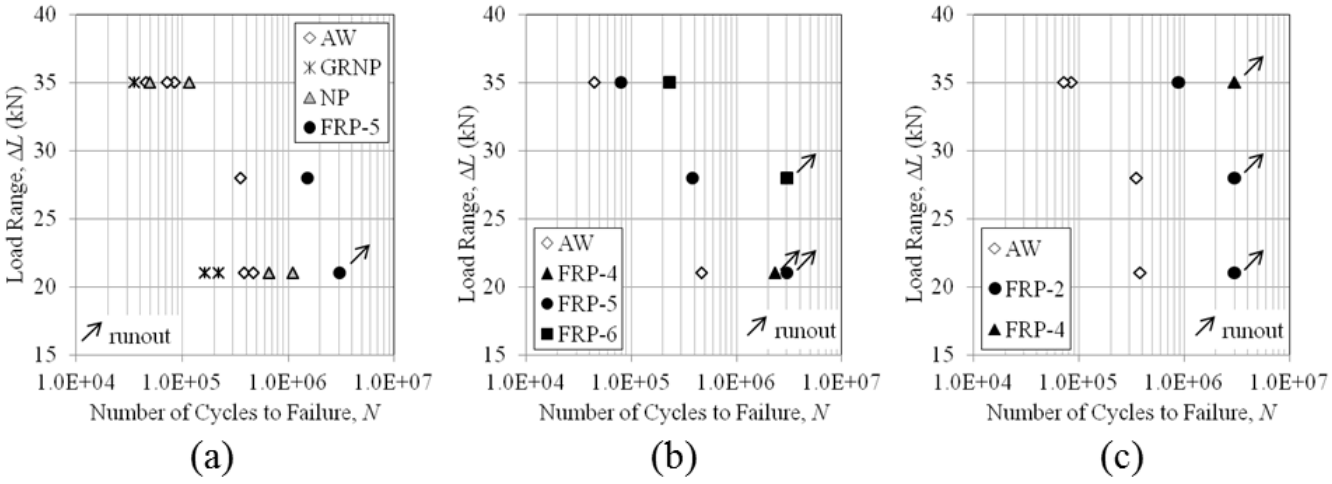

Figure 2.6: Fatigue test results: (a) initially uncracked specimens; (b) FRP-retrofitted specimens under VA loading; (c) FRP-retrofitted specimens under CA loading

Table 2.6: Fatigue test results

Test ID	Repair-*L*-Specimen	*N*	Failure mode(s)	*HSS* (MPa)	*d* (mm)	
1	AW-C35-1A	84,000	TC	458	0.53[1]	**Tests conducted on initially uncracked specimens**
2	AW-C35-1B	72,000	TC	478	0.56	
3	AW-V35-2B	45,000	TC	459	0.55	
4	AW-C21-3B	383,000	TC	314	0.34	
5	AW-V21-4B	461,000	TC	304	0.34	
6	AW-C28-5B	351,000	TC	360	0.49	
7	NP-C35-2A	116,000	TC	449	0.55	
8	NP-V35-3A	49,000	TC	439	0.59	
9	NP-C21-4A	1,100,000	TC	310	0.31	
10	NP-V21-5A	658,000	TC	305	0.34	
11	GR-C21-2B	650,000	TC	324	0.33	
12	GRNP-V21-1B	160,000	TC	330	0.32[1]	
13	GRNP-C35-1A	35,000	TC	464	0.51[1]	
14	GRNP-V21-2A	220,000	TC	265	0.36	
15	FRP-5-V28-6AU	1,520,000	AD-w, FA-f, TC	178	0.32	
16	FRP-5-V21-6BU	<u>3,000,000</u>	*N.A.*	134	0.23	
17	FRP-5-V35-6BU	80,000	FA-f, TC	212[2]	0.41[2]	
18	FRP-1-C21-1A	7,500	AD-w	*N.A.*	0.46[1]	**Tests conducted on cracked specimens**
19	FRP-2-C21-1B	<u>3,000,000</u>	*N.A.*	*N.A.*	0.45	
20	FRP-2-C28-1B	<u>3,000,000</u>	*N.A.*	*N.A.*	0.57	
21	FRP-2-C35-1B	888,000	AD-s	*N.A.*	0.79	
22	FRP-3-V21-2A	81,000	FA-s	*N.A.*	0.37	
23	FRP-4-C35-2B	<u>3,000,000</u>	*N.A.*	*N.A.*	0.43	
24	FRP-4-V21-2B	2,310,000	AD-s	*N.A.*	0.34	
25	FRP-5-V21-3A	<u>3,000,000</u>	*N.A.*	*N.A.*	0.25	
26	FRP-5-V35-3A	80,000	AD-s	*N.A.*	0.58	
27	FRP-5-V28-3B	380,000	AD-s	*N.A.*	0.53	
28	FRP-6-V28-5A	<u>3,000,000</u>	*N.A.*	*N.A.*	0.49	
29	FRP-6-V35-5B	230,000	AD-s, AD-f	*N.A.*	0.59	

<u>*underline*</u>: run-out, AW: as-welded, NP: needle peened, GR: gouged-and-rewelded, GRNP: gouged- rewelded and needle peened, N.A.: not applicable, TC: through crack, AD-s: debonding within the adhesive-steel interface at FRP-to-stiffener connection, AD-f: debonding within the adhesive-steel interface at FRP-to-flange connection, FA-s: FRP angle leg attached to stiffener failure, FA-f: FRP angle leg attached to flange failure

[1] Estimated numbers using displacement measurements by the testing machine due to DCDT malfunction during testing

[2] Structural stress and displacement ranges right after the beginning of the experiment, i.e. not stabilized

According to the results presented in Table 2.6, Test 17 resulted in a failure after only 80,000 cycles under V35 loading while no failure was observed in Test 23 with a lighter retrofit after 3 million load cycles under C35 loading. This suggests that the maximum load level is a more critical design factor than the equivalent load level. Thus, FRP-4, FRP-5, FRP-6, and FRP-6 retrofits were subsequently tested under VA loading histories.

Figure 2.6 summarizes all of the fatigue tests on FRP-retrofitted specimens. The fatigue capacity was improved in all cases, while higher improvements were achieved at lower loading levels. It can be seen that the fatigue crack propagation period for the FRP repaired specimens was longer than the initial fatigue capacity of the uncracked specimens in all cases, except for the FRP-2 retrofit. Generally, higher fatigue life improvements were achieved when stiffer FRP angles were used in combination with the more ductile adhesive. Finally, debonding of the adhesive-steel interface at the FRP-to-stiffener connection (AD-s) was the most common failure mode observed.

2.5.2 Measured Strain and Deflection Data

Inspection of the strain-load data from the tests revealed an essentially linear behaviour after the first cycle. Non-linear behaviour during the first load cycle can be explained by initial test setup compliances (e.g. support settlement) or the high magnitude of the tensile residual stresses present at the surface due to welding. The direct strain measurements for the 21 kN load range and the out-of-plane displacement ranges measured by the DCDT are summarized in Figure 2.7. The measured strains for the 28 kN and 35 kN load ranges had a similar trend to the measured strains for the 21 kN load range. In these graphs, results at the equivalent load ranges are reported for the variable amplitude loading tests. As can be seen in Figure 2.7, a strong linear relationship is observed in the results, and no significant difference is observed between the results for as-welded, peened, and gouged-and-rewelded specimens. On the other hand, the magnitudes of both the out-of-plane displacements and strains within the web gap region were significantly reduced by the proposed FRP retrofitting method. It can be concluded that the proposed method enhances distortion-induced fatigue behaviour of the studied detail through reducing the out-of-plane displacement of the stiffener end on the web, and consequently reducing the stress ranges experienced at the critical weld toe.

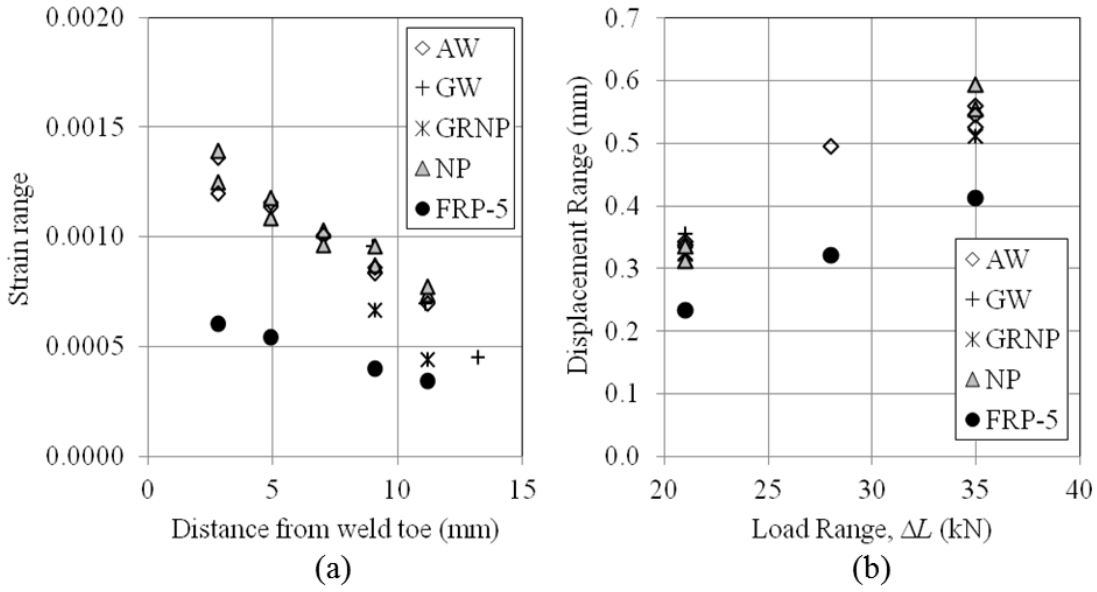

Figure 2.7: Measured strain ranges for C21 and V21 loading (a) and out-of-plane displacement ranges for all loading cases (b)

2.5.3 Structural Stress Analysis

Structural stresses for all fatigue tests on initially uncracked specimens were calculated according to [7] using linear extrapolation to determine the structural stress. Strains at distances of $0.4 \cdot t$ and $1.0 \cdot t$ (t = thickness of the web) from the weld toe were measured using strain gauges. However, the position of the five-element strip strain gauges in this study did not coincide exactly with those extrapolation points. Linear interpolation was therefore used to establish the required strains. The extrapolated structural stresses for all of the fatigue tests are presented in Table 2.6. After the structural stresses are extrapolated, fatigue test results can be expressed in terms of structural stress range vs. fatigue life and compared to structural stress design curves. Figure 2.8 presents all fatigue tests on initially uncracked specimens. A structural stress design S-N curve, the IIW FAT-100 curve, is also plotted for comparison purposes. The FAT-100 design curve is proposed for non-load carrying welds in [7]. The IIW FAT-90 curve is recommended for the structural stress design of load-carrying welds, and may be more appropriate in the case of web stiffeners at cross-bracing locations.

Results for as-welded, needle peened, and gouged-and-rewelded specimens were discussed in [4], highlighting the following observations: 1) the fatigue lives for all specimens lie above the IIW FAT-100 curve, 2) needle peening resulted in only a modest fatigue life increase within the tested structural stress ranges, and 3) the gouging-and-rewelding repair method was effective enough to restore the initial

design (FAT-100) fatigue capacity, although it resulted in shorter fatigue lives than seen for the as-welded specimens. While the effectiveness of FRP retrofitting cannot be evaluated using the S-N approach, it can be quantified in terms of the structural stress range. The average structural stress results for the unreinforced specimens and the FRP-retrofitted specimens for the 21 kN loading range are plotted in Figure 2.8. In this figure, the data points represent detecting a through crack on the loading side of the specimens. Moreover, according to this figure, the FRP retrofit resulted in a reduction in structural stress range greater than 50% in all cases.

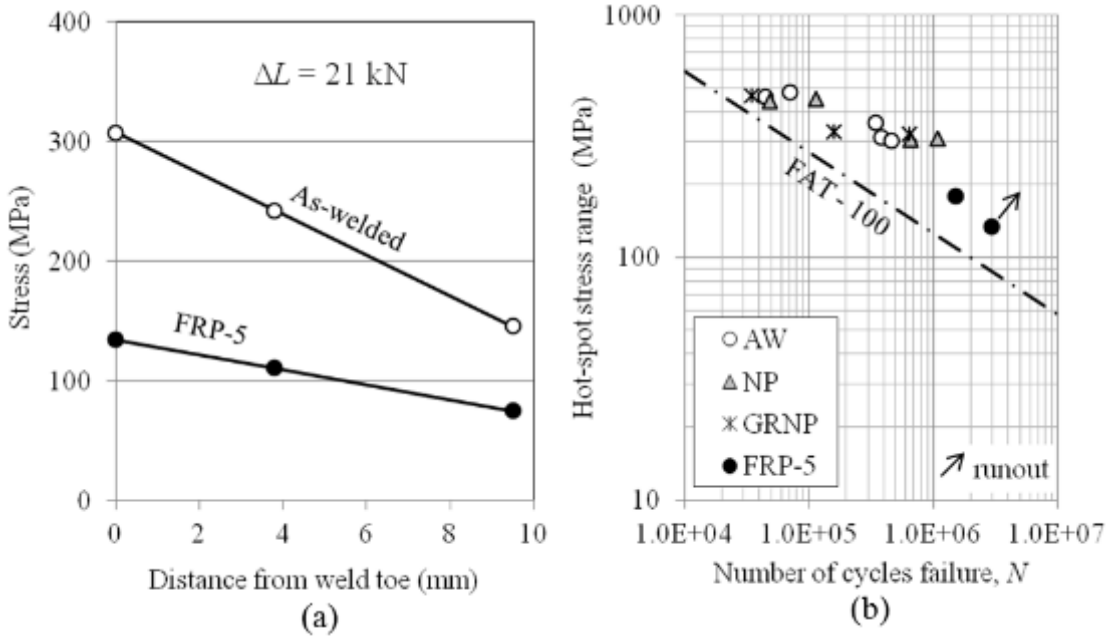

Figure 2.8: Measured structural stress range for 21 kN loading range (a) and fatigue test results for initially uncracked specimens (b)

In summary, for the load ranges tested herein, using the structural stress method with the IIW FAT-100 design curve resulted in a relatively conservative, but reliable prediction of the fatigue life of the web stiffeners. This is particularly important because there is no fatigue detail category for welded details similar to the one studied herein and the *classification method* (S-N approach) is therefore not capable of predicting the web stiffener fatigue life. It is suspected that the reason the fatigue test results from the current study are all above the IIW hot-spot stress design curve is that the web is being subjected to a loading with a high degree of bending, rather than axial loading.

2.6 Finite Element Analysis

2.6.1 Model Description

The FE analysis program ABAQUS was used to determine the local structural stress ranges by 3D static analysis of the fatigue test specimen. The specimen geometry (including welds) was modeled using 20-node quadratic brick elements. Meshing was based on recommendations in [7]. An elastic material with E = 200 GPa was assumed for the steel specimen and appropriate boundary conditions were applied. The fact that the secondary stresses within the web gap are induced by out-plane displacement of the web, which can be directly measured in the field, was considered in defining the loading step. Loading was applied so that a displacement range equal to the average measured range under CA loading was analyzed. For the as-welded specimens, the displacement ranges were 0.329 and 0.548 mm for 21 and 35 kN, respectively.

For design purposes, the structural stress can be determined by FE analysis with a relatively coarse mesh. When solid elements are used, according to [7], in most cases only one layer of elements across the plate thickness is sufficient to determine the structural stress. However, more precise results can be achieved by using a finer mesh. Herein, two layers of solid elements were used across the web thickness. A mesh study was also performed and the results are summarized in Figure 2.9. A good agreement (±5%) between the experimental and FE results was observed when finer elements (mesh type 4) were used. This meshing pattern was then chosen for this study. Default element in-plane dimensions of 30 mm by 30 mm were assumed. In the hot-spot regions, meshing was managed so that the extrapolation values for the structural stress calculation corresponded with nodal points.

A 3D static analysis of the FRP-5 retrofitted specimen was also performed. The GFRP section and adhesive layer were modeled as isotropic elastic materials with E = 5.5 and 0.1 GPa, respectively, based on the nominal properties in the product data sheets (Table 2.3 and Table 2.4). It should be noted that the GFRP modulus in the weak (CW) direction was conservatively assumed as a simplification in this analysis. While, in the actual attachment, a non-isotropic material is being subjected to a complex combination of bending and shear loading, it was thought that a simpler material model would be more feasible for the design of this type of retrofit in practice.

The FRP attachments were meshed using 20-node quadratic brick elements. The adhesive was modeled as a thin layer (0.5 mm thick) between the FRP section and the steel. Both the FRP attachments and

adhesive were meshed using a default element size similar to that of the steel specimen (30 mm by 30 mm). The adhesive layer was meshed using 8-node quadratic shell elements. The FRP sections, adhesive layer, and steel specimen were attached together using tie constraints.

Figure 2.9 shows the assembled model. As was done in the as-welded specimen analysis, structural stress ranges were calculated corresponding with the equivalent displacement ranges for the retrofitted specimens, i.e. 0.234 mm and 0.321 mm for 21 kN and 28 kN, respectively.

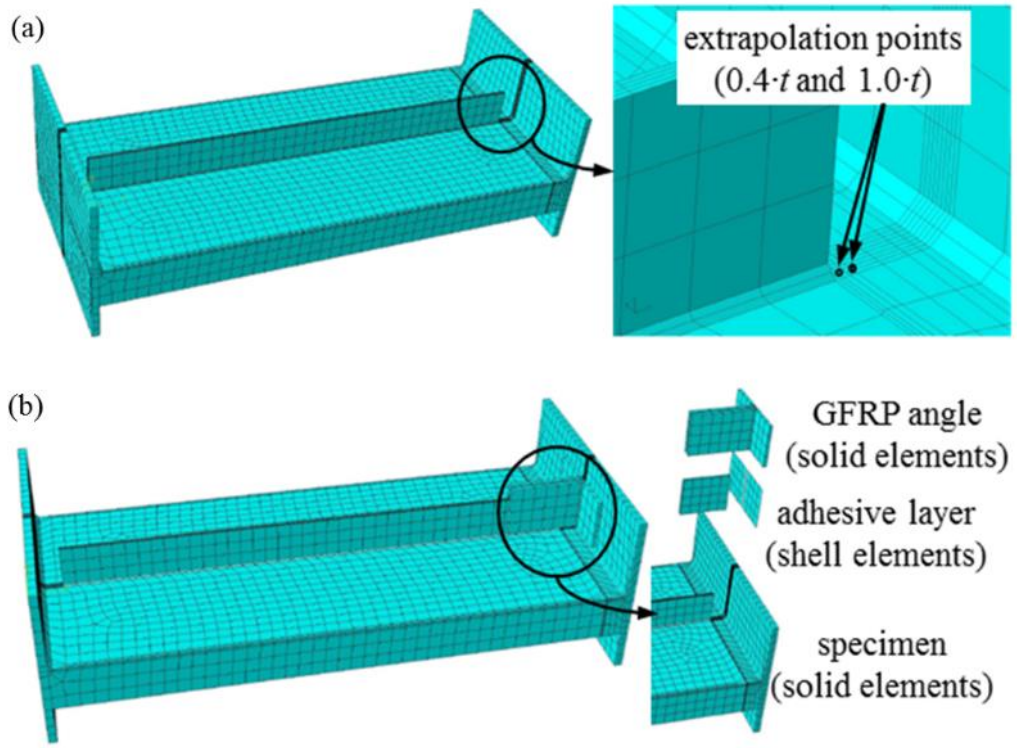

(c)

Mesh type	# of elements in each direction for each extrapolation point			Element size	
	Length	Width	Thickness	1st extrapolation point	2nd extrapolation point
1	1	1	1	0.4·*t* x *t* x *t*	0.6·*t* x *t* x *t*
2	1	1	2	0.4·*t* x *t* x 0.5·*t*	0.6·*t* x *t* x 0.5·*t*
3	2	1	2	0.2·*t* x *t* x 0.5·*t*	0.3·*t* x *t* x 0.5·*t*
4	2	2	2	0.2·*t* x 0.5·*t* x 0.5·*t*	0.3·*t* x 0.5·*t* x 0.5·*t*
5	3	3	3	0.13·*t* x 0.33·*t* x 0.33·*t*	0.2·*t* x 0.33·*t* x 0.33·*t*

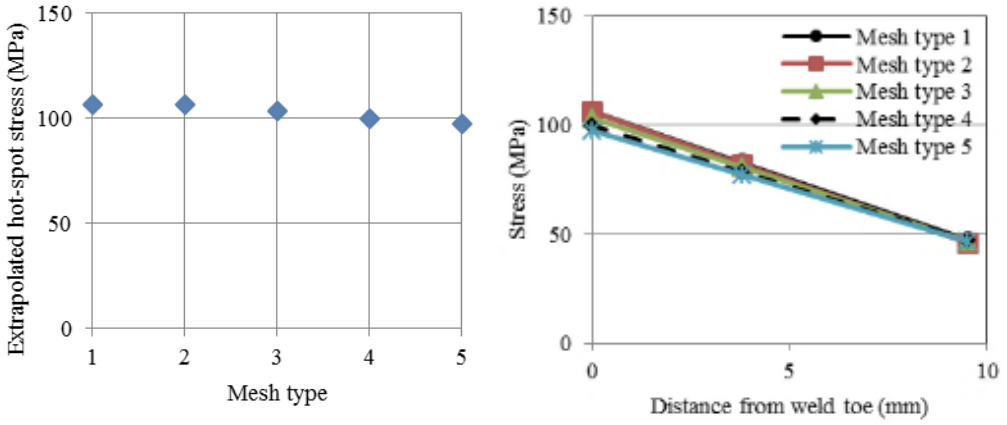

Figure 2.9: FE model assembly: (a) as-welded specimen; (b) FRP-retrofitted specimen; (c) mesh sensitivity analysis

2.6.2 Finite Element Analysis Results

Finite element analysis results consisting of the structural stress extrapolation for the as-welded specimens at the minimum (21 kN) and maximum (35 kN) load ranges tested in this study are shown in Figure 2.10. The structural stress ranges predicted using the FE analysis results were within 5% of the values obtained from direct strain measurements.

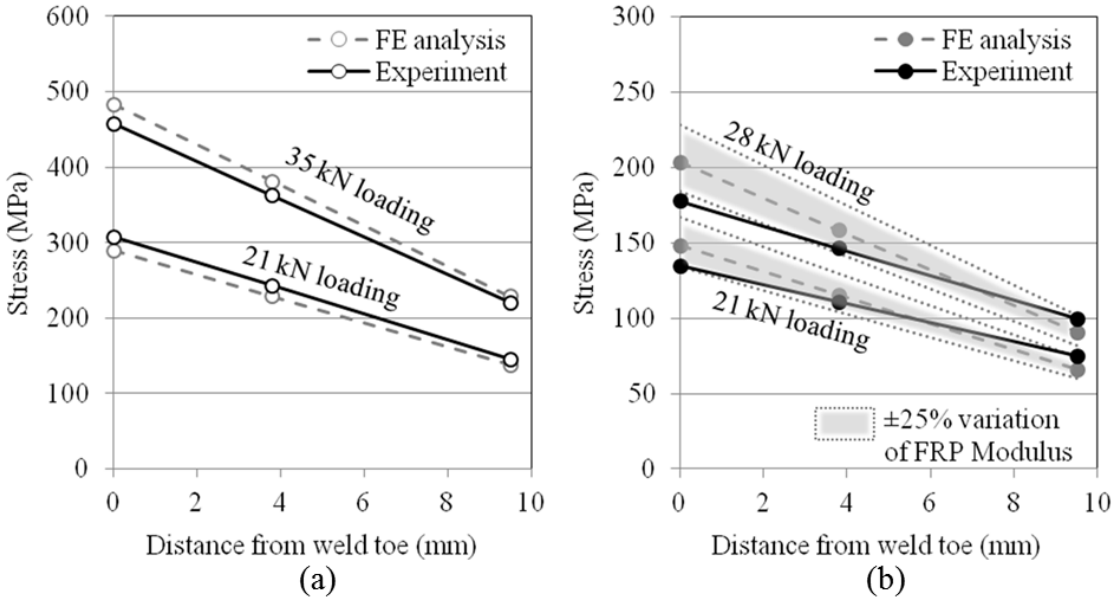

Figure 2.10: Structural stress extrapolation: (a) as-welded specimens; (b) FRP-retrofitted specimens

For the FRP-5 FE model, experimentally and analytically derived structural stress ranges for 21 kN and 28 kN load ranges are presented in Figure 2.10. As can be seen in this figure, the analytically derived structural stress ranges were close to the values calculated by direct strain measurements and conservative for both load levels. The higher error in the FE predictions of structural stress for the FRP-5 model compared to the unreinforced model may be attributed to the use of the nominal material stiffness in the weak (CW) direction for the GFRP material. Tension coupon tests performed for this study showed that the actual elastic moduli in the strong (LW) and weak (CW) directions were higher than the nominal values (see Table 2.3). In order to study the effects of the stiffness assumptions for the GFRP and adhesive on the predicted structural stress ranges, sensitivity studies were performed on these parameters. These studies showed that varying the stiffness or thickness of the adhesive layer over a wide range (covering the nominal elastic moduli of both tested adhesive products and an estimated

practical range for the adhesive layer thickness) had a negligible effect on the predicted structural stress. On the other hand, the predicted structural stress was seen to be significantly affected by the assumed GFRP elastic modulus. In Figure 2.10, the effects of varying this parameter over a range of ±25% are illustrated, showing the importance of this parameter. While further refinements to the FE analysis would be beneficial for gaining a better understanding of the behaviour of the GFRP angle and adhesive layer, with the presented results, it can be seen that the structural stress method in conjunction with a coarse FE analysis offers a practical and reasonably accurate means for verifying the fatigue performance of the critical welds before and after retrofitting.

2.7 Analytical Study of the Efficiency of the FRP Retrofit

A similar FE modelling scheme to that used in the previous section was then employed to study the effects of a number of the varied geometrical and mechanical parameters on the efficiency of the proposed FRP retrofit. These varied parameters included: direction of the applied cyclic loading (diagonal loading rather than vertical loading), the geometrical properties of the FRP angles, the elastic moduli of both the FRP angle and the adhesive material, and the location where the FRP attachments were employed (i.e. attachments bonded to the stiffener and web or to the web and flange instead of angles attached to the stiffener and flange). The FE model used for structural stress analysis of the FRP-retrofitted specimen in the previous section was considered as a benchmark (FE-B). Loading P was applied so that a structural stress equal to 100 MPa could be calculated for the FE-B specimen. The same load P was then applied to all subsequent analyses. The effect of each parameter was studied separately by using an FE model as described in the following paragraphs.

A diagonal load was applied in model FE-L. In the experimental study, a vertical cyclic load was applied through the up and down movement of a jack, as dictated by laboratory constraints. However, in actual steel bridges, out-of-plane web displacements are caused by cross frame members, which are often diagonal rather than vertical with respect to the web. In the FE-L model, a diagonal loading with the same magnitude of P in both the vertical and horizontal directions was applied.

The FE-M1 and 2 models were used to investigate the effect of the elastic modulus (E) for the FRP and adhesive material on the efficiency of the proposed retrofit method. In FE-M1 model, lengthwise (LW) flexural modulus of 12.4 GPa was used for the GFRP material (a 125% increase). For FE-M2, a high modulus adhesive (SikaFast®-3131) with E = 3.6 GPa was modeled (a 3500% increase).

The FE-G1 to 4 models were used to study the effects of geometrical properties of the FRP angle, as described in Table 2.7.

Table 2.7: Models FE-G1 to 4

FE model	Varied dimension	New value (in.)	% increase
FE-G1	*a* (short leg)	5.2	24
FE-G2	*b* (long leg)	8.5	13
FE-G3	*l* (length)	6	20
FE-G4	*t* (thickness)	0.5	33

Distortion-induced fatigue damage usually happens in locations that are not easily accessible for implementing retrofits. The proposed method may then not be applicable to some structural details. Still, FRP attachments can be used at other locations with the goal of reducing the stress demand in the web gap region. Two cases were studied herein. In the FE-WS model, FRP angles were attached to the stiffener and web to provide more connectivity between the stiffener and the web. In the FE-WF1 and 2 models, FRP angles were used to create a load path between the flange and web on the stiffener and opposite sides (see Figure 2.11).

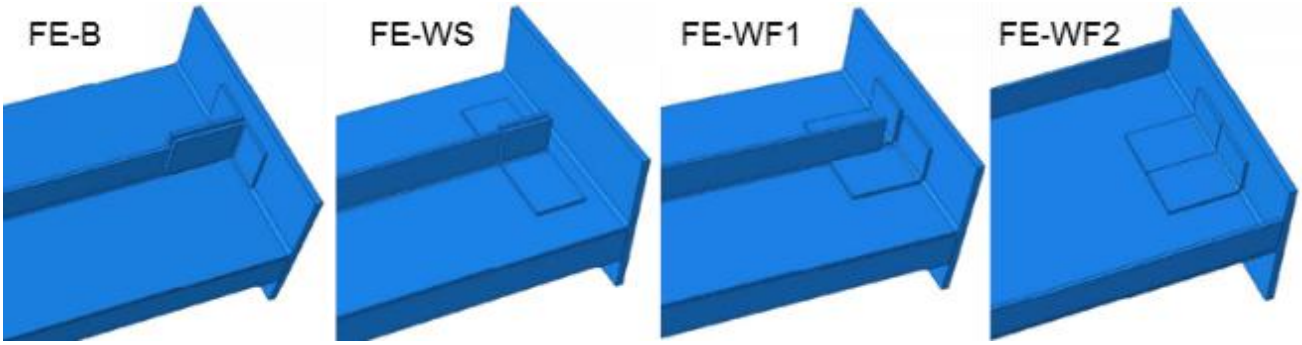

Figure 2.11: FE model geometries

Results for the FE-based parametric study are presented in Figure 2.12. In addition to the 11 FE models described earlier, FE results for an unretrofitted (as-welded) specimen are added for comparison (FE-AW). As can be seen, FE-M1 and FE-WS were the most and least efficient methods studied herein, respectively.

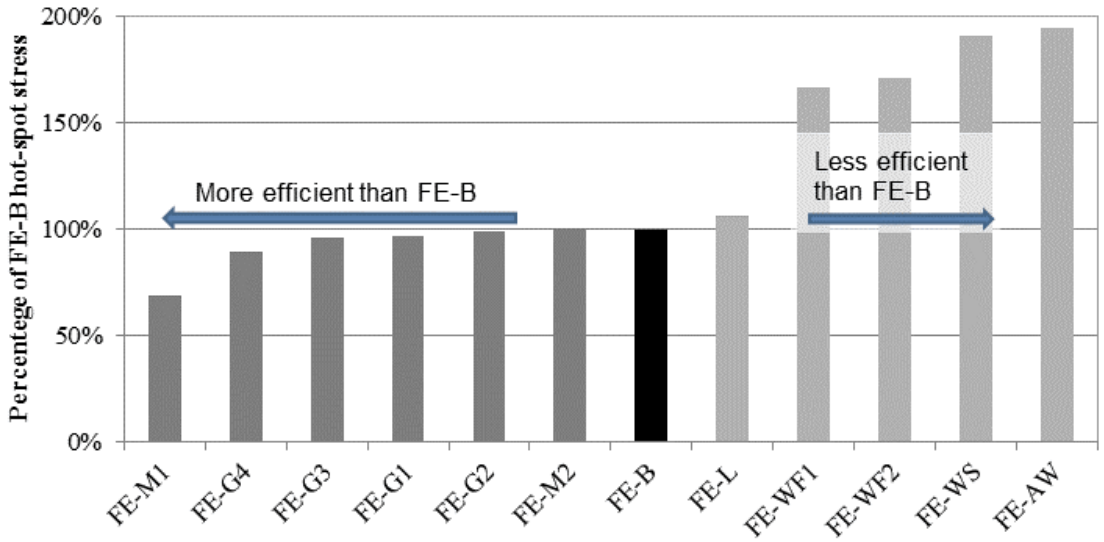

Figure 2.12: FE-based study results

Results are summarized in Table 2.8. For the FE-M and G models, the proportional benefit is defined as the percent variation in the structural stress value per one percent variation in the varied mechanical or geometrical parameter. For instance, according to the table, a 1% increase in FRP's elastic modulus resulted in a 0.25% decrease in the structural stress value in FE-M1.

Table 2.8: Fatigue tests results

FE model	% increase in the varied parameter (%)	*HSS* (MPa)	*HSS* reduction %	Proportional benefit (%)
FE-AW	N.A.	195	N.A.	N.A.
FE-B	N.A.	100	N.A.	N.A.
FE-L	N.A.	106	-6	N.A.
FE-M1	125	69	+31	0.25
FE-M2	3500	100	0	0
FE-G1	24	97	+3	0.12
FE-G2	13	99	+1	0.08
FE-G3	20	96	+4	0.20
FE-G4	33	89	+11	0.33
FE-WS	N.A.	191	-91	N.A.
FE-WF1	N.A.	167	-67	N.A.
FE-WF2	N.A.	171	-71	N.A.

Based on the results in Table 2.8, the following observations are made:

- The *HSS* increased slightly when a diagonal (45º) load was applied rather than a vertical load in FE-B. Although the structural stress did not change significantly, adding a force component parallel to the web was seen to induce additional stresses in both the FRP angle and adhesive.

- Using a higher modulus FRP material resulted in a significant increase in the efficiency of the proposed retrofit method.

- Using a higher modulus adhesive did not change the *HSS* value. When applied to in-service bridges, using a high modulus adhesive will generate higher stresses in the adhesive layer which, consequently, will make the retrofit vulnerable to a sudden failure of the adhesive.

- Among the geometrical properties of the FRP angle, the highest benefit was achieved by increasing the thickness, followed by increasing the length. Although increasing two other dimensions (*a* and *b*) did not affect the *HSS* value significantly, an angle with bigger legs may be needed to provide more bonding area between the FRP angle and steel.

- Attaching the FRP angles to the stiffener and web, resulted in an almost no reduction in *HSS* comparing to the unretrofitted case (FE-AW). This can be explained by the fact that no extra stiffness was provided to the weak web gap region as a result of this retrofit.

- Attaching the FRP angles to the web and flange was not as efficient as attaching the angles to the stiffener and flange. However, some improvement (up to 15% reduction in *HSS*) was achieved compared to the unretrofitted case. When attaching the FRP angles to the stiffener and flange is not possible due to geometrical constraints, this method can be used. It is expected that higher *HSS* reductions will be achieved when longer and thicker FRP attachments are used. Moreover, the modeled FE-WF2 retrofit can be used in combination with the retrofit discussed in FE-B.

2.8 Conclusions

The idea of using adhesively-bonded FRP angles as a retrofit method for distortion-induced fatigue problems associated with web stiffeners in steel bridge girders is proposed, tested, and analyzed in this chapter. Based on the presented research, the following conclusions are drawn:

- Significant fatigue life increases on the order of several hundred percent, depending primarily on the imposed loading range, were achieved by implementing this retrofit method.
- Debonding within the adhesive-steel interface was found to be the most common failure mode when the FRP angle retrofit method was used, followed by failure in the FRP angles. Using a highly ductile adhesive appeared to result in a delayed, gradual failure in comparison with the use of a high strength, high modulus adhesive.
- The hot-spot stress design curve was successfully used to estimate the fatigue life of the as-welded and retrofitted web stiffener ends. This is of paramount importance, considering the fact that the conventional S-N curves provided in different codes and standards are for as-welded joints only and cannot be used for unconventional welded joints such as web stiffener ends where neither a fatigue detail category nor a nominal stress are defined.
- The proposed FRP-based retrofit method was found to be significantly more efficient than two other conventional repair methods. While the other methods focus on improving the local fatigue properties at the weld toe, the FRP-based retrofit method reduces the stresses in the web gap region.
- The efficiency of the FRP angle retrofit method can be determined by using a coarse finite element (FE) model before implementation and by direct field measurements after implementation. This should enable bridge owners to design case-specific FRP angle retrofits, predict their effectiveness, and evaluate them after implementation.
- The effects of a number of the varied geometrical and mechanical parameters on the efficiency of the proposed retrofit method were studied using a finite element analysis. Generally, it was found that greater improvements, in terms of reducing the hot-spot stress, can be achieved when stiffer FRP angles are used than for other methods. Additionally, using a ductile structural adhesive, rather than a high modulus one, was recommended in order to reduce the stresses in the adhesive layer, and to avoid a sudden failure due to a possible severe overload.

Chapter 3

High Cycle Fatigue Behaviour of Impact Treated Welds under Variable Amplitude Loading Conditions

3.1 Introduction

The fatigue performance and durability of welded steel structures can be enhanced by post-weld treatments (PWTs). Residual stress-based PWTs (i.e. peening or impact treatments) are proven to be an effective, reliable, and economical means for extending the service lives of welded structures [1-3]. When these PWTs are applied, a compressive residual stress field is introduced near the surface of the treated weld toe, which delays, or even arrests, the growth of small fatigue cracks.

The effectiveness of a wide variety of PWTs, including conventional peening methods (e.g. needle or hammer peening) and high frequency mechanical impact (HFMI) treatments–also known as ultrasonic impact treatment (UIT), has been verified in numerous laboratory and analytical fatigue studies [4-8]. Using the same mechanism to improve the fatigue strength of welded connections as other residual stress-based PWTs, HFMI treatment tools provide a comfortable working condition with less noise and vibration compared to low frequency pneumatic tools. This makes HFMI tools easier to operate for longer periods of time and, consequently, HFMI treatment is a practical method for enhancing the fatigue performance of large welded structures with numerous fatigue-prone weld details. Methods for proper execution and quality control of HFMI treatments are being developed [9-11]. Field trials and tests of weld details on large-scale girders are reported in [12-14]. It is also being shown that impact treatments can be particularly effective when applied to existing structures (welds on steel bridges, for example), since the permanent stresses due to the self-weight are imposed prior to the treatment [15, 16].

Several experimental and analytical studies have been conducted with the goal of generating *S-N* design curves (in terms of both the nominal and structural stress) to include the beneficial effect of HFMI treatment in structural design codes [7, 12, 17-19]. The literature in this field includes experimental and analytical results for a wide variety of welded details and loading conditions in the mid- to high cycle domain (less than 10^7 cycles). Despite the extensive research conducted in this field, very few, if any, studies have investigated the behaviour of treated welds in the ultra-high cycle domain (beyond 10^7 cycles). Additionally, the proposed fatigue limits (also called endurance limits) for the treated welds are

chosen conservatively in the absence of experimental results. Considering the current design service life of steel structures such as bridges (75 to 100 years, with > 4000 truck passages per day possible), more experimental results within the 10^7 to 10^8 cycle range are needed.

Recently, the fatigue life increase resulting from impact treatments has been acknowledged in several design codes and standards (e.g. [20, 21, 22, 28, 29]). The IIW Recommendations [22, 29] explicitly permit an increase in the structural (or "hot-spot") stress class due to the treatment of non-load carrying welds from FAT-100 up to FAT-125. Recent experimental studies have shown these recommendations are reasonable in the mid-cycle domain [18], but 'too conservative' in other cases, especially in the high-cycle domain [7, 17]. More than 400 fatigue test results conducted in 18 separate studies were analysed in [7] and it was found that the slope of the best fit line through *S*-*N* data is typically greater than the m = 3 used in guidelines. m = 5 was proposed based on the collected constant amplitude (CA) test results, mostly with a stress ratio (S_{min} / S_{max} = R) of 0.1, and the need for more variable amplitude (VA) test results for updating the design curves was highlighted. In another study [19], the existing high stress ratio (R = 0.5 to 0.7) CA test results and the limited available VA results on steel specimens were evaluated with respect to proposed IIW guidelines [22]. The *S*-*N* slopes for the different joint types varied between 4.4 and 9.6. It was concluded that a shallower *S*-*N* slope is more suitable for the fatigue design of the treated weld toes in the mid to high cycle (10^4 to 10^7 cycle) domain.

Available test data and design curves are mostly based on CA loading fatigue studies. It is now well known that for a similar stress range, impact treatments effectiveness decreases under CA loading as R ratio increases [3, 9, 17, 19]. In other words, the treatment effectiveness is dependent on the mean stress of the fatigue loading and, thus, impact treatments may not be suitable for structures operating at applied high stress ratios. For VA loading, however, the extent of the improvement depends on the stress history at the weld toe and seems to vary from one application to another. The beneficial effect of impact treatment decreases as the maximum applied stress approaches the yield strength of the material and the occasional application of severe tensile or compressive stresses on welded components can be detrimental in terms of relaxing the compressive residual stress [23]. In the absence of any systematic guidelines or test data, it was suggested in [7] that the maximum stress in the VA loading spectrums be limited to 80% of the yield strength to ensure the effectiveness of HFMI treatments.

Interactions between load cycles of different stress ranges also influence the fatigue behaviour of a weld toe. Fatigue damage caused by a particular stress cycle under VA loading can be more damaging than

under CA loading [5, 24], mainly due to the crack closure mechanisms [25]. As a result, Miner's sum [26] or the root-mean-cube (RMC) method may lead to inaccurate (conservative or non-conservative) results. Some of the main parameters influencing the fatigue behaviour of structures under VA loading are the occurrence of periodic overloads (or underloads), load cycle arrangement in the load spectrum, and the maximum and minimum stress levels. Hence, when determining the effectiveness of impact treatments in a specific application, it is of paramount importance that the relevant VA load spectrum is considered. For example in highway bridges, where the in-service loading histories typically contain overloads (e.g. due to occasional very heavy trucks) followed by smaller load cycles, the frequency and magnitude of the overloads should be determined (e.g. by field measurement).

Another factor that limits the achievable level of fatigue improvement for treated welds is the possibility of alternative modes of failure (other than weld toe failure). Welding tensile residual stresses and the stress concentration due to the change in the geometry tend to make weld toes the most vulnerable location for fatigue crack initiation and propagation in welded joints. When residual stress-based PWTs are applied to the weld toe, the tensile residual stresses are replaced with compressive residual stresses and, in some cases, the stress concentration is also reduced [9], resulting in a fatigue strength improvement at the weld toe. After treatment of the weld toe, the critical failure mode of a welded detail may change (for example) to root cracking or fatigue crack growing from sub-surface fabrication flaws or material defects in the base metal. Secondary failure modes may then ultimately control the fatigue strength of the impact treated joint, particularly for joints containing load-carrying welds.

Transverse and longitudinal stiffeners are common non-load carrying weld details in steel structures. Most of the 414 data points reported in [7] for four specimen types with non-load carrying welds failed at the weld toe. In addition, a variety of other failure locations was observed in high strength steel (f_y > 400 MPa) specimens under CA loading condition with an R ratio of -1. Treated non-load carrying welds were reported to fail consistently at locations other than the weld toe in [14, 27]. The as-welded longitudinal fillet welded joints tested in [14] all failed at the weld toe whereas the treated joints all failed in the weld throat (cracks initiated at the weld root). The specimens in [14] were made from 30 mm thick mild steel (f_y = 390 MPa) plates. A similar observation was made in [27], where fatigue improvement of high strength steel (HSS) was studied. While all of the as-welded specimens failed at the weld toe, almost all of the treated specimens experienced other modes of failure under CA loading

including plate edge (base metal) failure, weld start/stop position failure, grip region failure, and root side failure. Under VA loading, however, the treated specimens failed at the weld toe.

Cover plates represent a common load carrying welded detail in steel structures such as bridges. A cover plate detail representing AASHTO [28] Det. Cat. E was tested in both the as-welded and treated condition in [12]. It was observed that in the high-cycle domain and for smaller weld sizes, fatigue cracks in the treated cover-plate welds originated at the weld root; a fatigue resistance corresponding with Det. Cat. D was still achieved for treated cover plates. As-welded and HFMI treated cover plates were also studied in [6] and an improvement in fatigue life of 25 times was observed. However, the treatment again shifted the crack initiation site. Surface cracks in the weld throat near one end of the transverse weld were observed in the treated specimens whereas the untreated specimens all experienced fatigue cracking at the weld toe. The results for the treated specimens were all well above AASHTO Det. Cat. D, which was previously proposed for the treated cover plates in [12].

Against this background, the current study was undertaken with the goals of: (1) examining the fatigue performance of treated structural steel welds in the high and ultra-high cycle domain under simulated in-service VA loading conditions, (2) using the experimental results to validate proposed guidelines in the literature, (3) using the structural stress approach and the effective notch stress approach to predict the fatigue life of the treated welded joints, and (4) making recommendations regarding the effectiveness of HFMI treatments when applied to welded steel structures subjected to VA loading conditions.

3.2 Fatigue Test Description

Two specimen types (load carrying and non-load carrying welds) subjected to as-welded and treated toe conditions were fatigue tested under three load histories including two VA loading spectrums and one CA loading with $R = 0.1$. All of the fatigue tests were conducted in a servo-controlled testing frame with the loading frequencies of 30 to 100 Hz, depending on the loading magnitude. The previous research had verified that the used range of testing frequencies did not affect the test results.

3.2.1 Specimens

The specimens were fabricated from 300 mm wide CSA G40.21 350W steel with a plate thickness t of 9.5 mm (3/8”). This steel is a mild, weldable structural steel grade with a nominal yield strength of 350 MPa (50 ksi) and an ultimate strength of 450-650 MPa (65-95 ksi). Tensile coupon testing was conducted and the material yield and ultimate tensile strengths were 390 and 606 MPa, respectively.

Two different specimen geometries were studied including transverse stiffener specimens with non-load carrying fillet welds (Type-X) and lap joint specimens with load carrying welds (Type-L). As-welded Type-X specimens represent a nominal detail category of FAT-80 according to [29], a hot-spot fatigue class of FAT-100 according to [30], and Det. Cat. C according to AASHTO [28]. As-welded Type-L specimens represent a nominal detail category of FAT-63 (parent metal) and FAT-45 (weld throat) according to [29], a hot-spot fatigue class of FAT-90 according to [30], and Det. Cat. E' according to AASHTO [28]. The attachments, i.e. transverse stiffeners and laps, were welded to the plates using the flux-cored arc welding (FCAW) process with a nominal weld size of 6.4 mm (1/4 in.). All of the welding was performed by the same certified welder at the University of Waterloo's Engineering Machine Shop. The welded plates (as-welded and treated) were then cut into 42 mm wide strips and ''dog-boned'' (see Figure 3.1) using a computer numerical control (CNC) cutting machine.

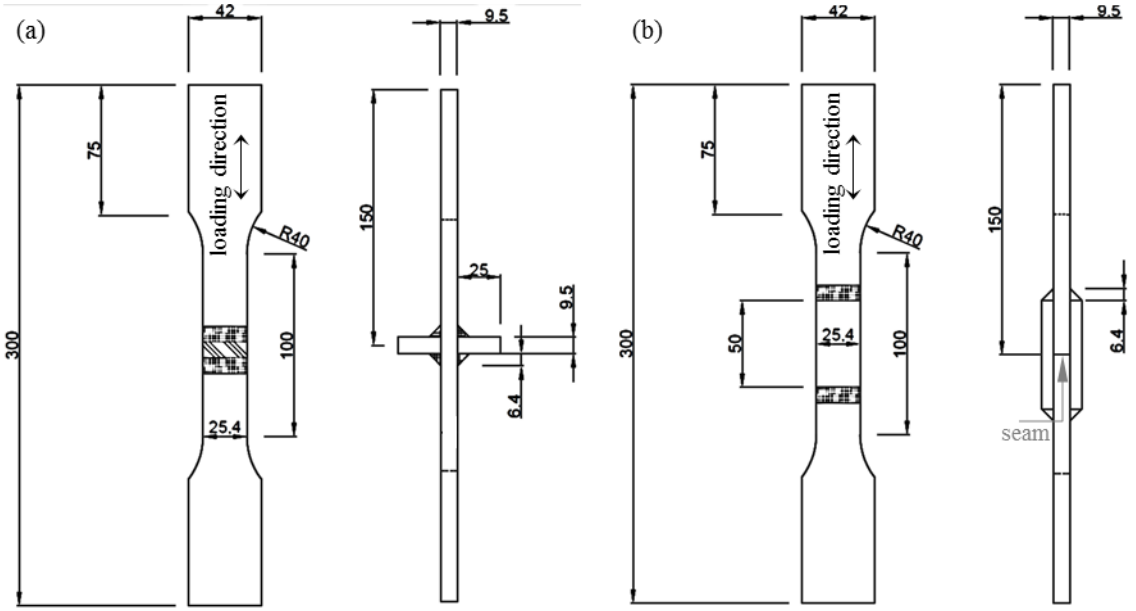

Figure 3.1: Fatigue specimen geometries (all dimensions in mm): (a) transverse stiffener (Type-X); (b) lap joint (Type-L)

3.2.2 Treatment

The treatments were performed manually in three 'passes' at angles (with respect to the larger plate) of 45º, 30º, and 60º with the HFMI tool set to an amplitude of 27–29 μm. The weld toes were inspected after the treatment to confirm that there was no visible line at the center along the location of the original weld toe (Figure 3.2). The treatment parameters, including the tool, amplitude, and inspection procedures, were set to simulate the field treatment of structural steel welds as a retrofitting measure.

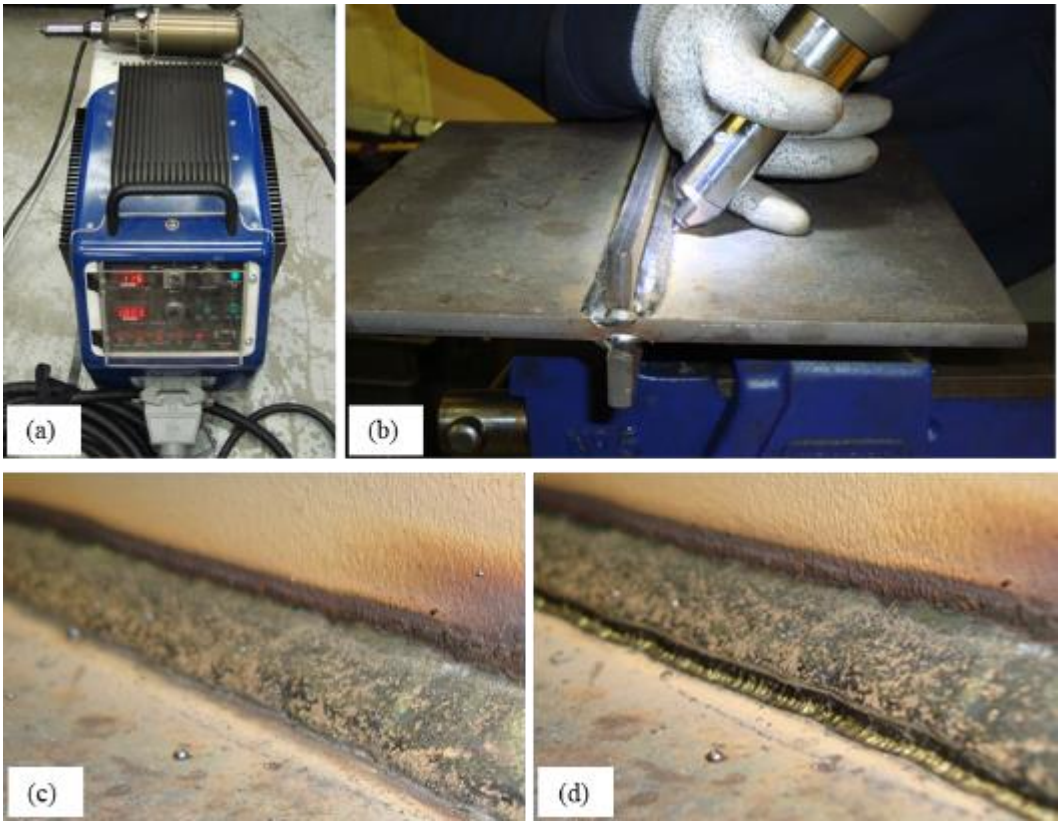

Figure 3.2: Impact treatment of weld specimens: (a) HFMI tool; (b) treating a weld toe; (c) as-welded weld toe; (d) treated weld toe

3.2.3 Loading

Three different types of fatigue loading were considered and scaled to vary the stress range, including: CA loading with $R = 0.1$, and two simulated in-service VA loading histories. Each VA loading block was repeated until the specimen failed. Testing was discontinued if no failure happened after roughly 100 million load cycles, at which point the test was considered a ‘‘runout”.

The VA histories were generated using traffic data from a survey of axle spacings and loads conducted in Ontario, Canada in 1995 [31], which included a total of 10,198 trucks. Randomly extracted VA spectrums blocks (1,000 cycles) of these load histories had been used previously in [5, 18, 32]. In the current study, the full VA loading histories were used. As explained in [5], these loading histories were generated by successively passing the trucks over influence lines for two locations on simply-supported bridge girders with different spans. The two cases considered in this study included the mid-span moment of a 40 m girder (VA1) with 10,195 load cycles in each block and the support reaction of a 15 m girder (VA2) with 6,470 load cycles in each block (after filtering to eliminate very small cycles less

than 1/3 of the CAFL). Rain-flow analysis was carried out for the two VA loading histories and the results are presented in Figure 3.3. Miner's sum was used to calculate the CA equivalent stress range (ΔS_{eq}) for the VA tests, assuming a slope of $m = 3$ for the *S*-*N* curve.

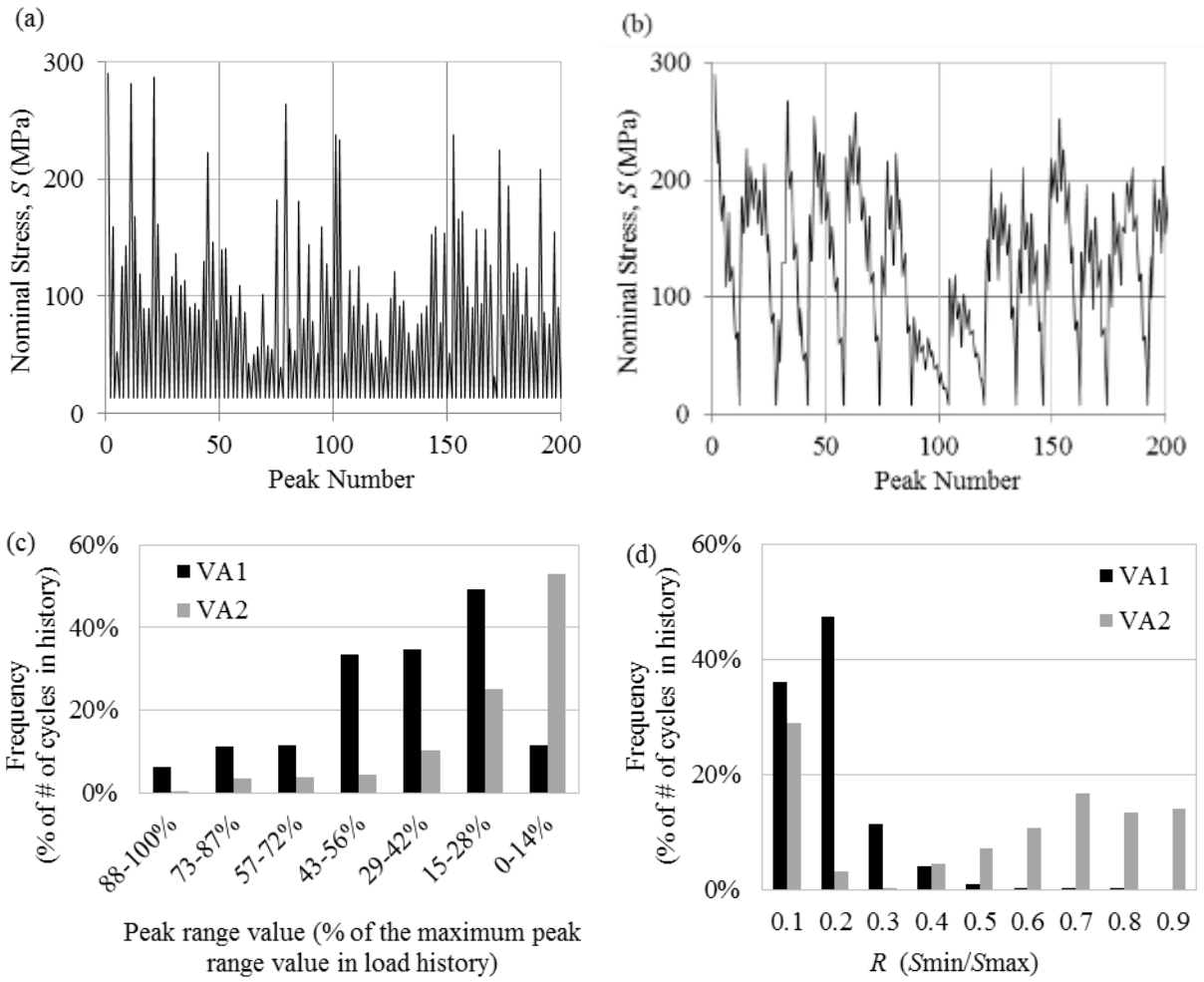

Figure 3.3: VA loading histories: (a) mid-span moment of a 40 m girder (VA1); (b) support reaction of a 15 m girder (VA2); (c) VA loading histograms; (d) *R* histograms

Significant differences can be seen between the two VA loading histories. Since the girder span is much longer than the typical truck length in VA1, only one large load cycle is caused by passing each truck over the bridge. In the second case (VA2), where a shorter girder span is considered, each axle load causes a small cycle as it comes on or off the end of the bridge. Consequently, VA1 consisted of a series of mainly large load cycles (compared to the maximum load level) all with the same minimum stress levels. However, VA2 consisted of mainly small load cycles with different minimum stress levels (and thus with higher mean stress levels compared to the same stress range in VA1).

3.3 Fatigue Test Results

Results of the 67 fatigue tests conducted in this study are summarized in Table 3.1 and Table 3.2.

3.3.1 Modes of Failure

While all of the as-welded specimens failed at the weld toe, various modes of failure were observed for the treated specimens. All of the treated Type-X specimens that failed did so as a result of cracks initiating at the weld toe and had fatigue lives greater than the as-welded specimens. Five of the treated Type-L specimens failed at the weld toe with no fatigue life increase, three exhibited a mixed root / toe failure mode, and all of the other treated specimens failed due to cracks initiating at the weld root. In other words, the impact treatment resulted in shifting the failure mode (Figure 3.4).

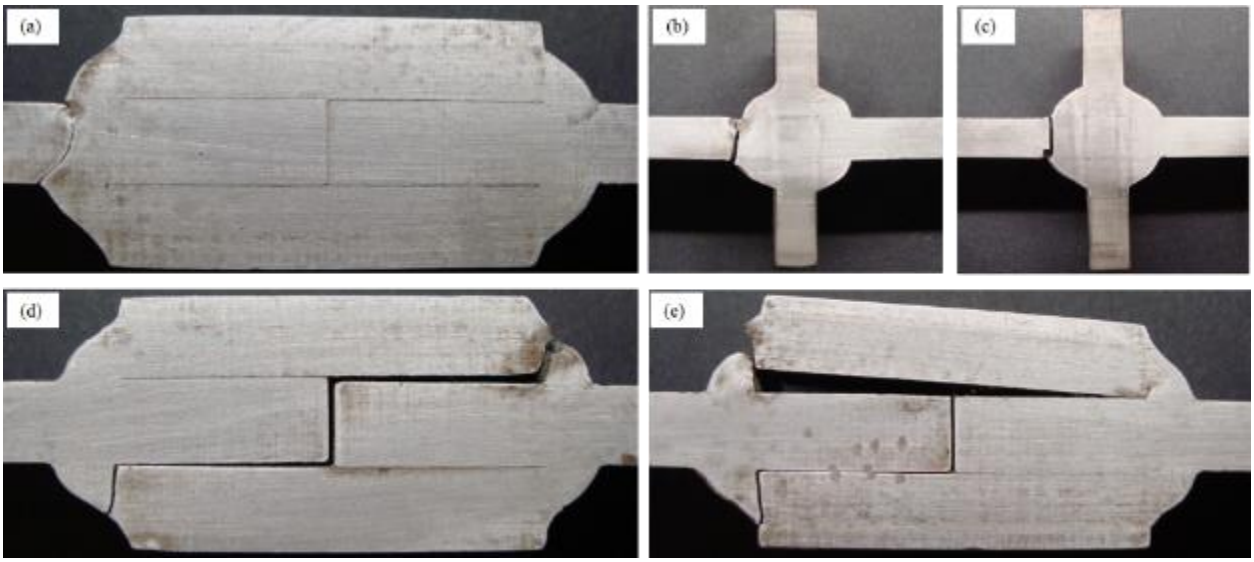

Figure 3.4: Fatigue cracking modes in specimens: toe failures in as-welded lap specimen (a) and as-welded and treated cruciform specimens (b and c); root failure in treated lap specimens (d and e)

Table 3.1: Fatigue test results for transverse stiffener (Type-X) specimens

Test ID	N (10^3 cycles)	ΔS_{eq} [†] (MPa)	S_{max} (MPa)	S_{min} (MPa)	ΔS_{max} (MPa)	ΔS_{min} (MPa)	ΔS_{min} [*] (MPa)
As-welded							
XAC-1	1,995	108	120	12			
XAC-2	920	144	160	16			
XAV-1	3,843	87	180	10	171	3	11
XAV-2	1,131	110	229	12	217	3	14
XAV-3	713	121	252	13	239	4	15
XAV-4	397	186	387	21	367	6	23
XAW-1	8,203	61	167	7	162	3	3
XAW-2	1,921	83	226	9	220	3	3
XAW-3	1,041	117	319	13	310	5	5
XAW-4	627	142	387	16	376	6	6
Treated							
XTC-1	<u>101,080</u>	106	118	12			
XTC-2	25,995	127	141	14			
XTC-3	3,165	155	177	18			
XTC-4	1,255	159	177	18			
XTC-5	2,365	165	177	18			
XTC-6	1,720	170	177	18			
XTC-7	6,450	180	200	20			
XTC-8	4,650	191	212	21			
XTV-1	<u>192,686</u>	66	138	7	131	2	8
XTV-2	<u>100,685</u>	71	148	8	141	2	9
XTV-3	<u>101,545</u>	76	159	8	151	2	10
XTV-4	<u>103,020</u>	82	170	9	161	3	10
XTV-5	22,327	87	180	10	171	3	11
XTV-6	45,826	110	229	12	217	3	14
XTV-7	16,852	121	252	13	239	4	15
XTV-8	14,283	154	320	17	304	5	19
XTV-9	625	186	387	21	367	6	23
XTW-1	21,103	76	207	8	201	3	3
XTW-2	52,989	83	226	9	220	3	3
XTW-3	64,693	96	262	11	254	4	4
XTW-4	13,599	108	295	12	286	4	4
XTW-5	27,646	117	319	13	310	5	5
XTW-6	6,592	125	341	14	331	5	5
XTW-7	1,818	142	387	16	376	6	6

Note 1: the naming convention is specimen type (X or L), toe condition (A = as-welded; T = treated), loading spectrum (C = CA; V = VA1; W = VA2), specimen number

Note 2: underline = runout (testing was discontinued after roughly 100 million cycles)

[†] CA equivalent stress range with $m = 3$

[*] The minimum stress range present in the loading spectrum with at least 1% occurrence in the loading block.

Table 3.2: Fatigue test results for lap joint (Type-L) specimens

Test ID	N (10^3 cycles)	ΔS_{eq}[†] (MPa)	S_{max} (MPa)	S_{min} (MPa)	ΔS_{max} (MPa)	ΔS_{min} (MPa)	ΔS_{min}[*] (MPa)
As-welded							
LAC-1	27	251	279	28			
LAC-2	17	308	342	34			
LAV-1	652	71	148	8	141	2	9
LAV-2	1,080	76	159	8	151	2	10
LAV-3	1,651	78	161	9	153	2	10
LAV-4	468	87	180	10	171	3	11
LAV-5	56	186	387	21	367	6	23
LAW-1	9,840	50	136	6	133	2	2
LAW-2	964	66	179	7	174	3	3
LAW-3	116	142	387	16	376	6	6
Treated							
LTC-1	505	180	200	20			
LTC-2	220	253	282	28			
LTC-3	80	300	333	33			
LTC-4[+]	55	311	346	35			
LTC-5[‡]	25	323	358	36			
LTC-6[+]	40	334	371	37			
LTC-7[‡]	13	346	384	38			
LTC-8[‡]	10	392	435	44			
LTV-1	71,466	66	138	7	131	2	8
LTV-2	8,156	82	170	9	161	3	10
LTV-3	11,479	87	180	10	171	3	11
LTV-4	9,073	92	191	10	181	3	11
LTV-5	4,373	121	252	13	239	4	15
LTV-6	1,223	154	320	17	304	5	19
LTV-7[‡]	66	186	387	21	367	6	23
LTW-1	<u>364,066</u>	43	116	5	113	2	2
LTW-2	<u>102,824</u>	46	125	5	122	2	2
LTW-3	28,733	50	137	6	133	2	2
LTW-4	12,267	58	158	6	154	2	2
LTW-5	11,451	66	179	7	174	3	3
LTW-6[+]	782	112	306	12	297	5	5
LTW-7	1,442	125	341	14	331	5	5
LTW-8[‡]	135	142	387	16	376	6	6

Note 1: the naming convention is specimen type (X or L), toe condition (A = as-welded; T = treated), loading spectrum (C = CA; V = VA1; W = VA2), specimen number

Note 2: underline = runout (testing was discontinued after roughly 100 million cycles)

[†] CA equivalent stress range with $m = 3$

[*] The minimum stress range present in the loading spectrum with at least 1% occurrence in the loading block.

[+] Specimen exhibited mixed mode of failure (fatigue cracking at weld root and toe).

[‡] Specimen failed at weld toe.

3.3.2 Effect of Large Overloads

Currently, no benefit for impact treatments can be claimed if the R ratio is higher than 0.4 according to [29] and it is assumed that the impact treatment methods are not suitable if the maximum applied stress is higher than $0.8 \cdot f_y$ according to [22]. To study the potentially unfavourable effect of large tensile overloads on the fatigue behaviour of the treated welds, 18 of the fatigue tests were conducted at equivalent stress range levels high enough that the tensile stress peaks in the loading history were greater than $0.8 \cdot f_y$ (280 MPa) including 12 treated Type-L (LT) and 6 treated Type-X (XT) specimens. All six of the XT specimens still exhibited fatigue life improvements. For the LT specimens, however, five specimens subjected to overloads larger than f_y (350 MPa) failed at the weld toe with no fatigue life improvement and three specimens exhibited a mixed (root / toe) mode of failure with a minimal fatigue life improvement. The results were not affected by the large overloads for the remaining four specimens with $0.8 \cdot f_y < S_{max} < f_y$ (Table 3.2). The fact that the treated weld toes in different specimens exhibited different types of fatigue behaviour under similar nominal loading highlights the need to define this limit based on a local approach (e.g. a structural or effective notch stress approach).

3.3.3 Effect of High *R* Ratios

More than 50% of the load cycles in the VA2 history had R ratios greater than 0.4, while almost all of the cycles in VA1 had R ratios between 0 and 0.2. For the treated specimens, VA2 was found to be somewhat more damaging than VA1 for both specimen types, indicating the unfavourable effect of the high R cycles. However, significant fatigue life increases were still observed under VA2 loading.

In the following sections, the test results are used to evaluate a number of available recommendations for the fatigue design of impact treated welds. The nominal, structural, and effective notch stress approaches are considered. An FE analysis is performed to determine the local stresses. A statistical analysis of the fatigue test results is also conducted and characteristic *S-N* curves with slope m=5 are proposed for the fatigue design of treated welds under VA loading in the high cycle domain.

3.4 Nominal Stress Approach

Stress-life (*S-N*) results in terms of the nominal stress range for each specimen group are plotted in Figure 3.5 and Figure 3.6. The corresponding as-welded design *S-N* curves from [28, 29, 33] are also shown on these figures, along with *S-N* design curves for impact treated welds from [12, 17, 22, 29].

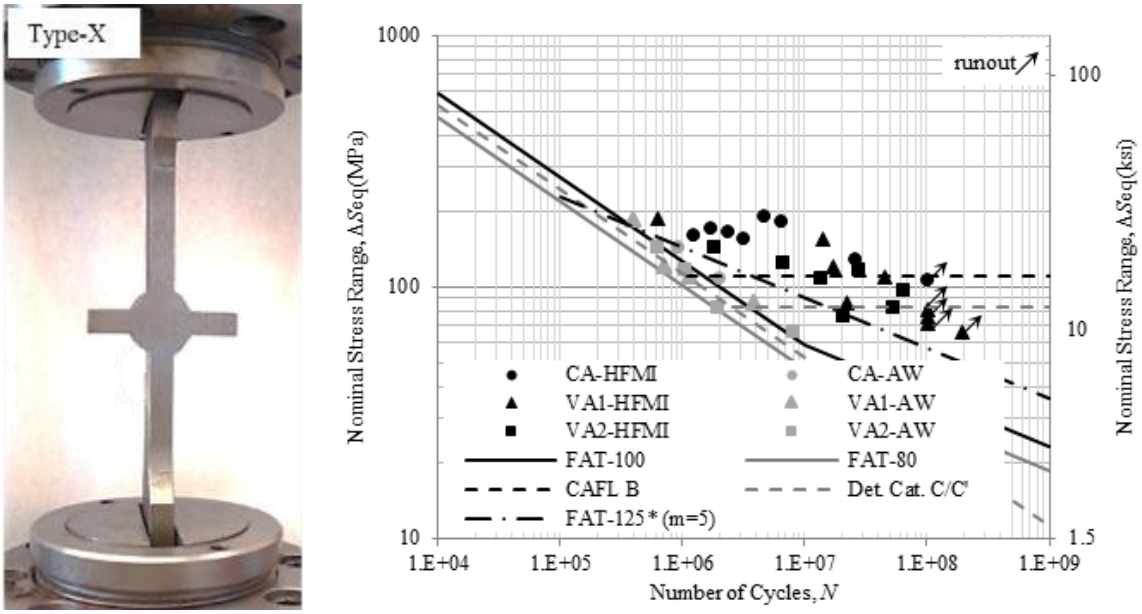

Figure 3.5: *S*-*N* results for transverse stiffener (Type-X) specimen

As can be seen in Figure 3.5, the as-welded (AW) specimens had fatigue lives close to the relevant as-welded design curves, namely: the AASHTO Det. Cat. C [28] and the IIW FAT-80 [29] curves. Note that there is a knee point in IIW FAT-80 curve at 10^7 cycles for VA loading and *m* changes from 3 to 5, whereas a constant amplitude fatigue limit (CAFL) is assumed at 10^7 cycles for the CA loading. No significant difference was observed between the as-welded CA, VA1, and VA2 results.

For the treated specimens, on the other hand, the loading spectrum does appear to affect the results. For the same stress range at different levels, CA and VA2 results generally had the longer and the shorter fatigue lives, respectively, as was seen previously for needle peening [5].

All of the CA failures for treated welds lie above the modified AASHTO design curve for Det. Cat. C/C' with the CAFL for Det. Cat. B (110 MPa). This curve was proposed in [12] for impact treated transverse non-load carrying attachments with fillet welds under CA loading and does not consider any fatigue improvement in the finite fatigue life domain. The increase in the fatigue strength proposed in [12] is limited to CA loading and subject to the condition that either the treatment is applied under permanent loads or the stress due to dead (permanent) loads does not exceed 110 MPa. The CA fatigue test results obtained in the present study appear to support the validity of this design curve for the ultra-high cycle fatigue domain under CA loading.

All of the VA results for treated welds lie above the IIW FAT-100 detail curve, which represents treated (hammer peened) IIW FAT-80 details and considers a 1.3 times increase in the fatigue strength of the treated weld [22, 29]. When plotted in terms of the applied equivalent stress range, this curve was found to conservatively estimate the fatigue life for the treated specimens, especially in the ultra-high cycle domain (more than 10^7 cycles). It should also be noted that the CAFL of 60 MPa at 10^7 cycles according to this recommendation (not shown in the figure) was also found to be highly conservative.

The FAT-125* curve with a slope (m) of 5, instead of the traditional m = 3, proposed in [7] for impact treated transverse welds was found to accurately represent the design fatigue strength for the treated specimens in the mid- to ultra-high cycle (10^5 to 10^8 cycles) domains. Moreover, a more accurate CAFL of 90 MPa at 10^7 cycles (not shown in the figure) can be envisioned when m = 5 is used.

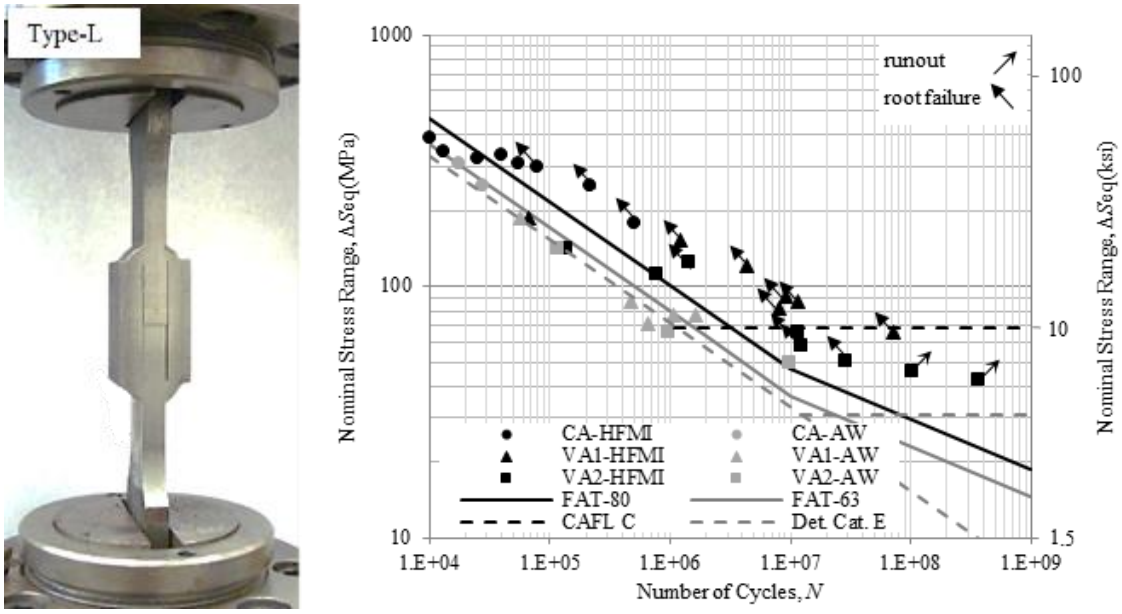

Figure 3.6: S-N results for lap joint (Type-L) specimen

In Figure 3.6 it can be seen that the as-welded (AW) lap joint specimens had fatigue lives close to but generally below the lives predicted by the two relevant design curves, namely: the AASHTO Det. Cat. E curve [28] and the IIW FAT-63 curve [29] representing transverse loaded lap joints with fillet welds. The suspected reason for this result is the particularly severe nature of the tested fatigue detail, wherein the central plate is cut so that the entire load passes through the cover plates via welds with a much smaller throat dimension than the cover plate thickness. Similarly to the Type-X specimens, no

significant difference was observed between the as-welded CA, VA1, and VA2 results; however, the loading type does appear to have a significant effect on the treated weld results.

All of the CA results for the treated lap joint detail lie above the modified AASHTO design curve consisting of a Det. Cat. E curve with the CAFL for Det. Cat. C (69 MPa). This increase in the fatigue strength is again limited to CA loading and subject to the condition that either the treatment is applied after the permanent loads are introduced or the stress due to these loads does not exceed 69 MPa [12]. Again, the CA fatigue test results obtained in the present study appear to support the validity of this design curve for the ultra-high cycle fatigue domain under CA loading.

The IIW FAT-80 design curve, which represents a 1.3 increase in the fatigue strength of the treated welds, is also plotted for comparison. It should be noted that this curve only applies to fatigue failures initiating at the treated weld toe and thus, cannot be used to design against other failure modes such as weld root failures [22, 29]. All except three of the VA tests on the treated welds fell above the IIW FAT-80 curve. The explanation for this result is that these three specimens experienced periodic tensile overloads with magnitudes higher than the nominal material yield strength (350 MPa).

Since the failure mode for the majority of the treated lap joint specimens was root failure, the FAT-125* curve was found inapplicable in this case and was therefore not included in Figure 3.6.

3.5 Structural Stress Approach

There are different methods available to determine the structural (or "hot-spot") stress at welded joints. These methods are generally based on: i) extrapolation of stresses at pre-defined reference points on the surface close to the weld toe or ii) linearization of the through-thickness stresses. Originally developed for and applied in the offshore structures, the structural stress approach aims to obtain the local stress at the weld toe using coarse (shell, planar, or 3D) finite element (FE) models or direct measurements. Detailed recommendations for hot-spot stress determination and analysis of the welded structures are described in [30, 34-36]. Different approaches to determine the structural stress are compared in these references and it is shown that depending on the geometry and loading conditions, the calculated structural stress may vary [37]. Thus, the method to calculate the structural stress should be carefully chosen based on the geometry and loading conditions. The extrapolation method, typically based on linear extrapolation of surface stress values at $0.4 \cdot t$ and $1.0 \cdot t$ from the weld toe where t is the plate thickness, has been successfully applied to weld details with load-transfer dominated behaviour.

However, for joints with localized stress concentration behaviour (i.e. local detail dominated behaviour), e.g. welded joints with two-sided transverse attachments under uniaxial loading, the extrapolated structural stress may not adequately capture the stress concentration effects (see Figure 3.7).

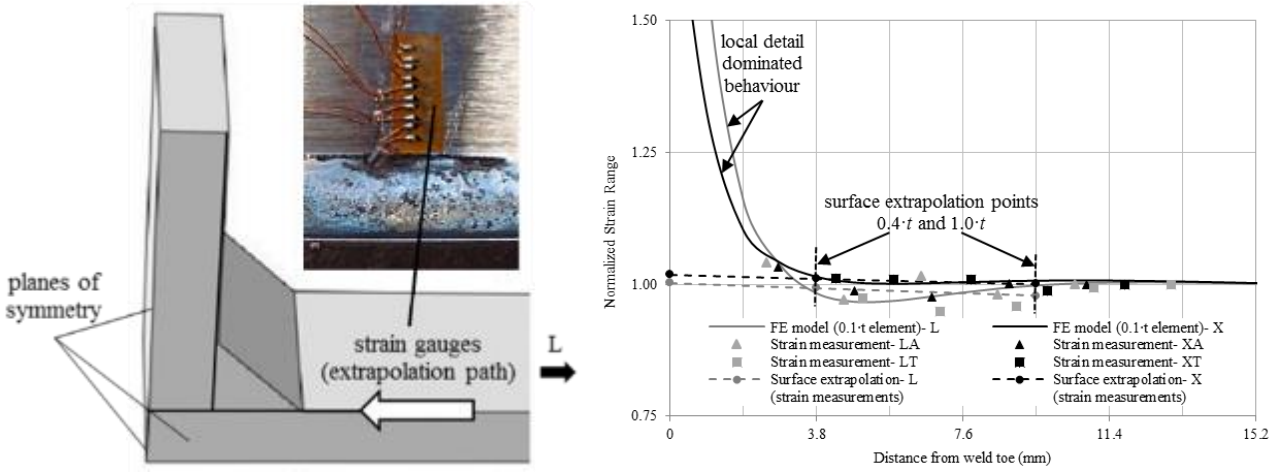

Figure 3.7: Strain profile in front of the weld toe based on measurements and FE analysis

To overcome this problem, other structural stress calculation methods have been proposed, including the ones described in [38-40], in order to develop a mesh-insensitive definition for the structural stress to be used in conjunction with rather coarse FE models. Considering the simple specimen geometries and the uniaxial loading condition used in the current study, Dong's definition of the structural stress [38] was used in conjunction with 2D FE models to evaluate the obtained experimental data. According to this definition, the corresponding statically equivalent structural stress (σ_s) at a weld toe is taken as the sum of the membrane component (σ_m) and bending component (σ_b). Using this definition, the equilibrium conditions within the context of elementary structural mechanics theory are satisfied at both the crack plane at the weld toe and an adjacent reference plane. The local stress distribution at the reference plane can be determined by using a conventional FE model. For solid models with symmetric loading and geometry with respect to the neutral axis of the loaded member and with non-monotonic through-thickness stress distributions (Figure 3.8), the bending and membrane components of the structural stress can be calculated using Equation 3.1 and Equation 3.2 [38].

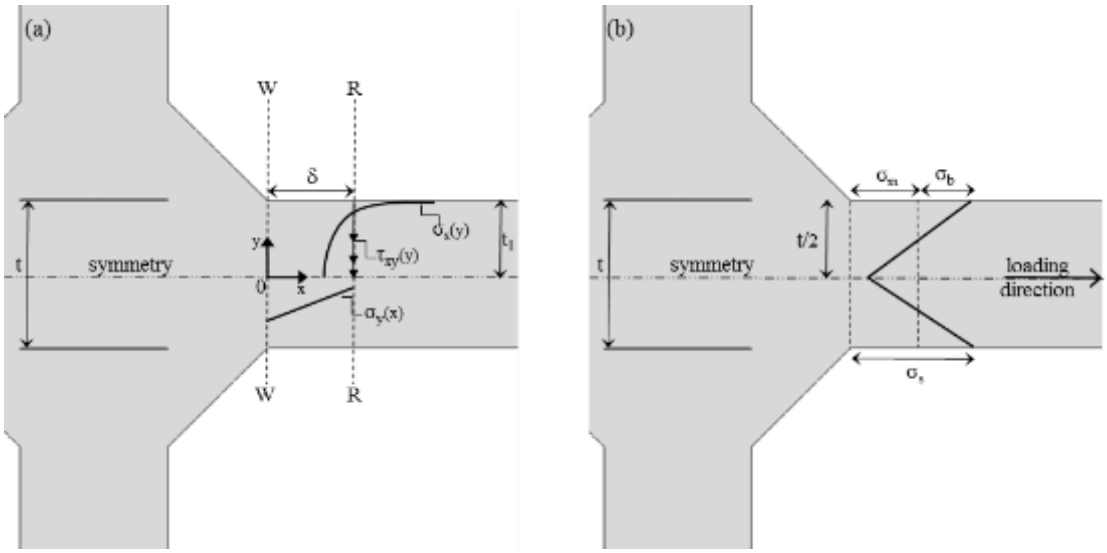

Figure 3.8: Structural stress for through-thickness stress distribution: (a) symmetry with respect to plate mid-thickness; (b) structural stress definition

Equation 3.1**:** $\sigma_m = \frac{1}{t_1} \cdot \int_0^{t_1} \sigma_x(y) \cdot dy$

Equation 3.2: $\sigma_m \cdot \frac{t_1^2}{2} + \sigma_b \cdot \frac{t_1^2}{6} = \int_0^{t_1} \sigma_x(y) \cdot y \cdot dy + \delta \cdot \int_0^{t_1} \tau_{xy}(y) \cdot dy + \int_0^{\delta} \sigma_y(x) \cdot x \cdot dx$

Equation 3.1 represents the force balance in the *x* direction along R-R, and Equation 3.2 represents moment balance with respect to W-W at $y = 0$. With this definition, the structural stress on the W-W plane can be determined using the stress distributions at a reference plane, R-R, as shown in Figure 3.8.

3.5.1 Finite Element Analysis

The FE analysis program *ABAQUS Version 6.12* was used to determine the structural stresses by 2D static analysis of the fatigue test specimens. Linear elastic material behaviour with $E = 200$ GPa was assumed and the specimen geometry was modelled using 8-node biquadratic plane strain quadrilateral elements. Typical model geometry and boundary conditions are presented in Figure 3.9. An element size (a/b) of $0.4 \cdot t / 0.5 \cdot t$ was used, based on [38]. A mesh sensitivity analysis was performed using various element sizes, including $0.2 \cdot t / 0.16 \cdot t$ and $0.1 \cdot t / 0.1 \cdot t$. A summary of the FE analysis results for the Type-X specimen is presented in Figure 3.9.

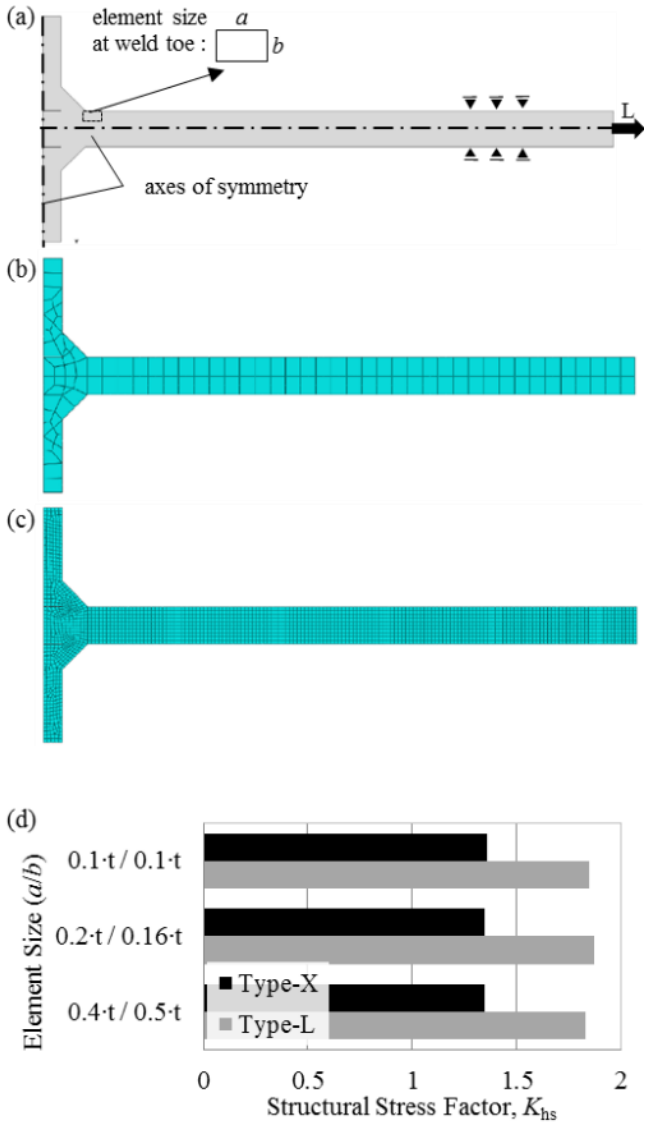

Figure 3.9: FE model for determining the structural stress (Type-X specimen): (a) model geometry; (b) coarse FE mesh (0.4·*t* / 0.5·*t*); (c) fine FE mesh (0.1·*t* / 0.1·*t*); and (d) structural stress factors

Based on the FE results, the structural stress concentration factors (K_{st}) of 1.35 and 1.85 were calculated for Type-X and Type-L specimens, respectively (Table 3.3).

Table 3.3: FE-based structural stress concentration factors

	Type-X	Type-L
σ_m	1.00	1.00
σ_b	0.35	0.85
σ_s	1.35	1.85

Figure 3.10 presents the fatigue test results for both specimen types in terms of their structural stress range (ΔS_{st}) where $\Delta S_{st} = K_{st} \cdot \Delta S_{nominal}$. Corresponding structural stress-based *S-N* design curves, according to [29], are also plotted for comparison. It should be noted that these curves are established for the structural stress estimated using the reference points and extrapolation equation given in [29]. In special cases, this reference also allows the use of alternative methods of estimation of the structural stress, including the procedure used in this study from [38], which are compatible with the fatigue design resistance data recommended in [29]. IIW FAT-100 and 125 represent as-welded and treated non-load carrying welds. FAT-90 represents as-welded load-carrying welds and FAT-112 represent a 1.3 increase in the fatigue strength of the treated load carrying welds that–similar to the nominal approach–cannot be directly applied to failure modes other than weld failure of the treated weld toe.

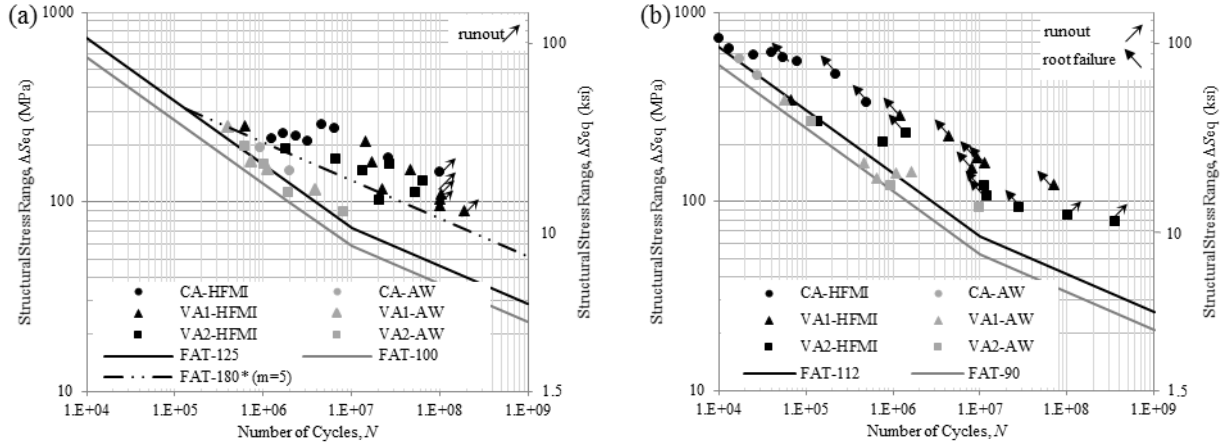

Figure 3.10: Structural stress *S-N* results: (a) Type-X specimen; (b) Type-L specimen

When expressed in terms of structural stress, all of the as-welded results for both specimen types now lie on or above the corresponding design curves. In comparison with the nominal stress approach (Figure 3.5 and Figure 3.6), the structural stress approach results in more accurate fatigue life predictions, in particular for the as-welded lap joint specimens. For the treated specimens, however, the assumed 1.3

times increase in fatigue strength for the treated welds [22, 29] still seems to be too conservative in both cases. Finally, the results for the treated Type-X specimens all lie near or above the modified FAT-180* curve, which is the proposed structural stress curve for treated non-load carrying welds [7].

3.6 Effective Notch Stress Approach

The notch stress approach for fatigue assessment of welded joints is based on the highest elastic stress at the weld toe or root. To account for the variation of the weld geometry parameters or arbitrary stress analysis results, the actual sharp toe and root are replaced by an effective (fictitious) notch with a reference radius. The effective notch stress is then defined as the total elastic stress at the root of the notch. An effective notch root radius of ρ = 1 mm is normally used for structural steels [29]. The effective notch stress can be calculated either numerically or by using the FE method for a welded joint and then compared with a single effective notch stress *S-N* curve for fatigue assessment.

3.6.1 Finite Element Analysis

The FE analysis program *ABAQUS Version 6.12* was again used to determine the effective notch stresses by 2D static analysis of the fatigue test specimens. Linear elastic material behaviour with E = 200 GPa was assumed and 8-node biquadratic plane strain quadrilateral elements were used to model the specimens. The effective notch radii were introduced in a way that the tip of the radius coincided with the root of the real notches at the weld toes and the end of the unwelded root gap. Model geometries and boundary conditions are presented in Figure 3.11. A locally fine mesh with an initial element size of 0.25 mm (ρ/4) was used in the vicinity of the round notches based on [29]. A mesh sensitivity analysis was performed using finer element sizes to accurately model the stress state at the notch roots.

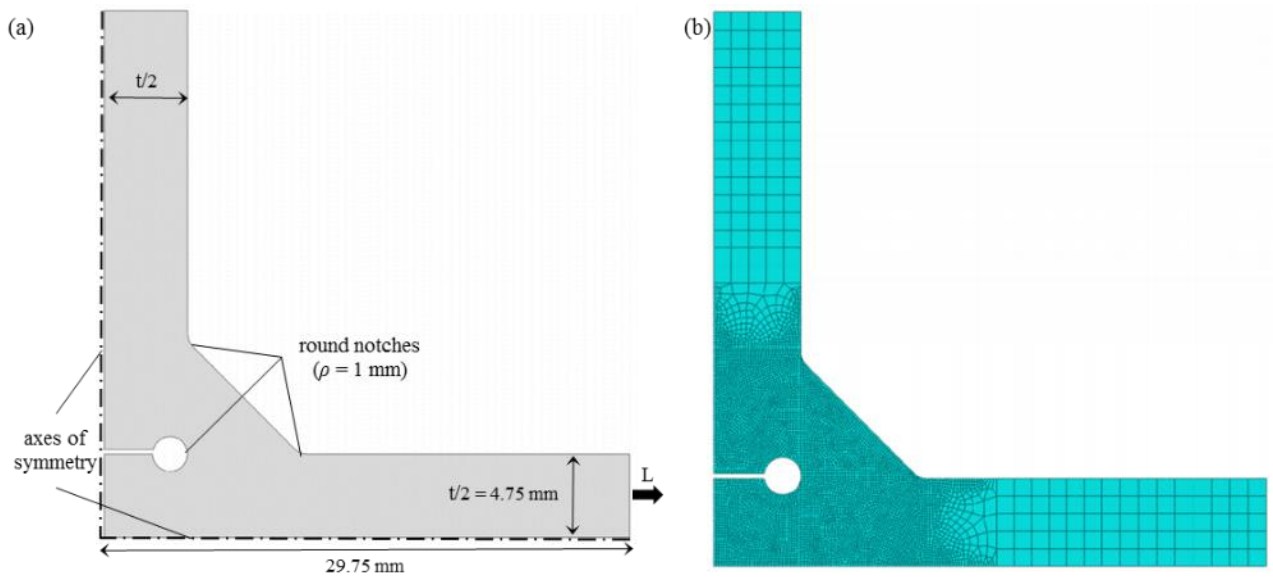

Figure 3.11: Determining the effective notch stress: (a) FE model geometry; (b) typical FE mesh

The notch factor (K_{ns}) was then defined as the ratio of the maximum principal stress at the notch (σ_{ns}) to the remote applied stress (unity here). A summary of the FE analysis results is presented in Table 3.4. Both of the specimen types had higher K_{ns} factors at their weld toe than that at the root.

Table 3.4: FE-based effective notch stress factors (K_{ns})

	Type-X	Type-L
$K_{ns\text{-}toe}$	2.37	4.38
$K_{ns\text{-}root}$	1.78	3.59

Figure 3.12 presents the fatigue test results for both the X-joint and L-joint specimens in terms of the effective notch stress range (ΔS_{ns}) where $\Delta S_{ns} = K_{ns} \cdot \Delta S_{nominal}$. The data points are categorized based on their failure modes (failure at the untreated toe, untreated root, or treated toe) and a corresponding K_{ns} factor is applied for determining the effective notch stress in each case. The IIW FAT-225 curve is also plotted representing the fatigue resistance of the as-welded steel joints [29].

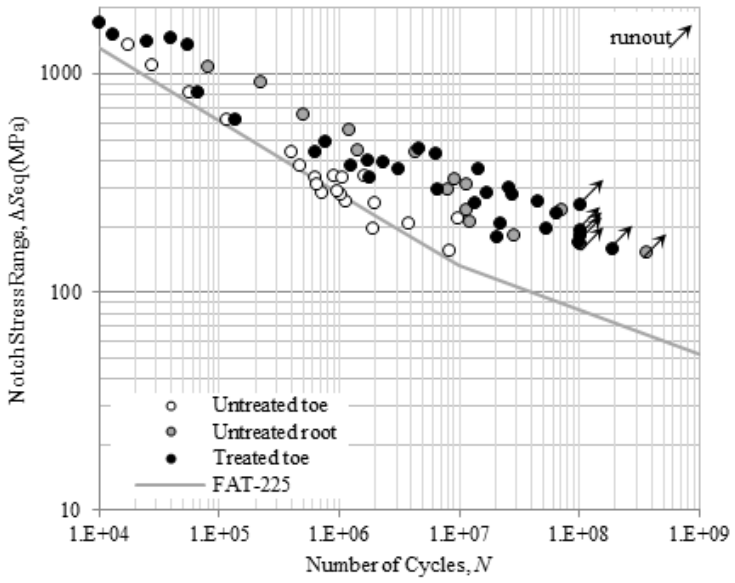

Figure 3.12: Effective notch stress *S*-*N* results

As can be seen in Figure 3.12, all of the as-welded toe failure results for the two specimen types lie close to the design curve and all of the treated weld toes experience fatigue lives longer than the lives estimated by the design curve. Additionally, the effective notch stress method was found to be overly conservative for predicting the fatigue life of the weld root for the L-joint specimens.

3.7 Statistical Analysis and Recommendations for Design

Following the IIW Recommendation [29], S-N curves associated with 50% and 95% survival probabilities were fitted to the fatigue test results by regression analysis. First, the constants of Equation 3.3 were established by linear regression of the fatigue test results for the data set of interest:

Equation 3.3: $\mathrm{LOG}(N) = \mathrm{LOG}(C) - m \cdot \mathrm{LOG}(\Delta S)$

Next, the mean (x_m) and standard deviation (*Stdv*) of the LOG(*C*) constant were calculated:

Equation 3.4: $x_m = \dfrac{\sum x_i}{n}$

Equation 3.5: $Stdv = \sqrt{\dfrac{\sum (x_m - x_i)^2}{n-1}}$

where n is the number of data points. Finally, the characteristic value of the LOG(C) constant (x_k) was calculated, following the procedure described in the IIW Recommendation [29] for a 95% survival probability with a two-sided 75% confidence level in the mean:

Equation 3.6: $x_k = x_m - k \cdot Stdv$

where k is the number of standard deviations that the characteristic value lies below the mean.

Characteristic nominal and structural stress S-N curves for as-welded and treated Type-X and Type-L joints were determined and are presented in Figure 3.13 and Table 3.5. Two curves for each specimen / treatment combination were produced; one representing the mean results (p_f = 50%) and one representing a 95% survival probability (p_f = 95%). Both the CA and VA test results were considered in generating these curves. Only the root failures were considered for the analysis of the treated Type-L specimens. The toe failures were not included on the basis that the peak tensile stresses for these tests were excessive (this point will be revisited in the following discussion). An iterative process was used to calculate the equivalent stress range, ΔS_{eq}, for the VA results. Initially, Miner's sum with m = 3 was used, the first round of statistical analysis was performed, and then a new value for m was calculated. ΔS_{eq} for the VA tests were then re-calculated using the Miner's sum and the new m, followed by another round of statistical analysis. This process was repeated for each case until the assumed and calculated values for m converged. The calculated m value and mean fatigue strength at 2 million cycles (ΔS_{2m}) for each case are summarized in Table 3.5. As expected, all of the S-N curves corresponding to the as-welded toe and root failures had m values close to 3. The S-N curve representing the failure at the treated weld toe, however, was significantly shallower than the as-welded curve.

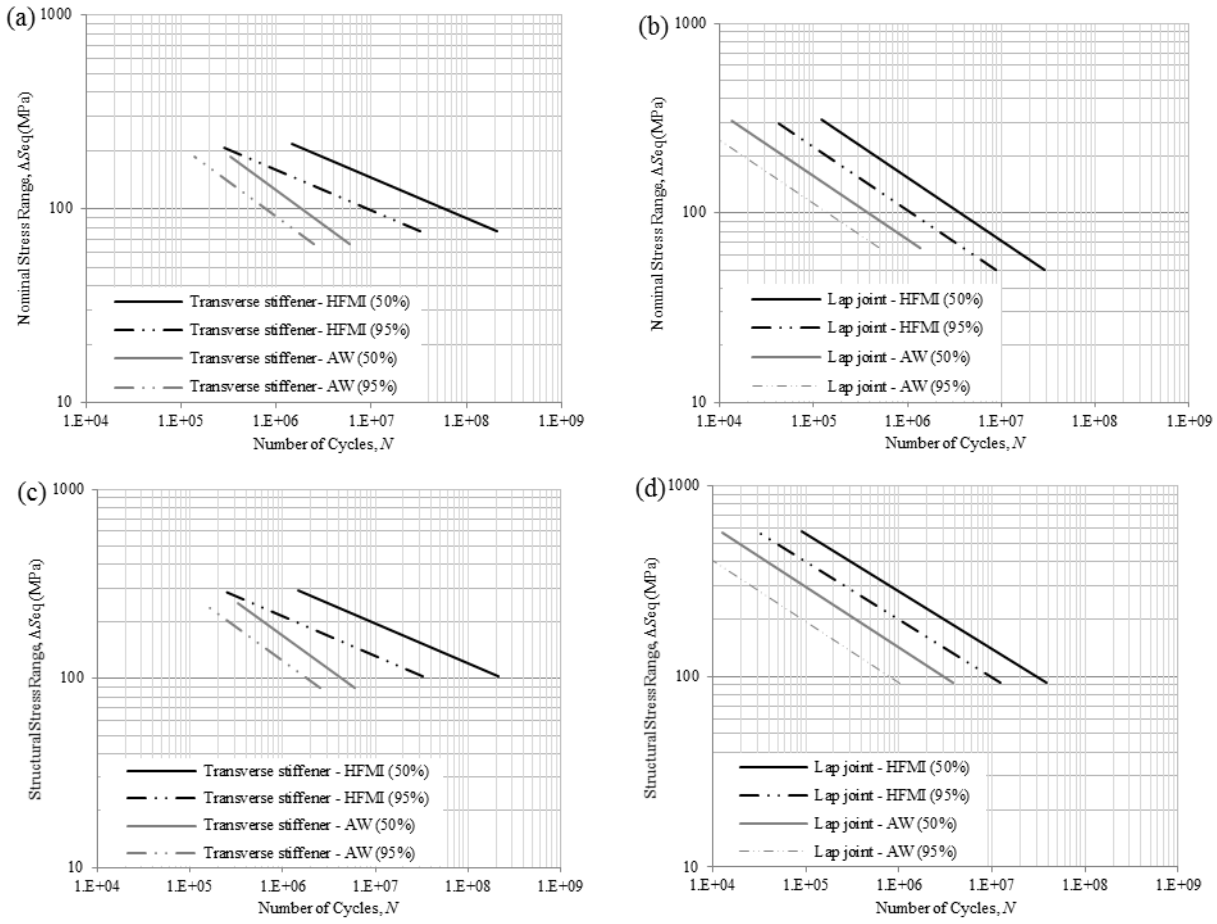

Figure 3.13: VA fatigue resistance curves (nominal and structural stress)

VA design *S-N* curves were then established based on the statistical analysis results. To be compatibile with the current design *S-N* curves, $m = 3$ was assigned for all four specimen / treatment combinations and the resultant FAT class (fatigue strength at 2 million cycles) was then determined. Another set of *S-N* curves with $m = 5$ was also derived for the treated Type-X specimens (see Table 3.5).

Table 3.5: Characteristic S-N curve data (nominal and structural stress)

Specimen/ Weld toe condition	Failure location	Calculated m	Calculated ΔS_{2m} (p_f = 50%)	Assigned m	FAT class (MPa)	Structural Stress FAT class (MPa)
Lap joint (L)/ As-welded	toe	3.13	61	3	41	76
Lap joint (L)/ Treated	root	3.31	122	3	82	151
Transverse stiffener (X)/ As-welded	toe	2.79	98	3	76	103
Transverse stiffener (X)/ Treated	toe	4.79	202	3	113	152
				5	135	182

As Table 3.5 suggests, the increase in the fatigue strength due to HFMI treatment was higher than 1.3 times for both joint types. This increase was 2 times for the lap joint specimens and 1.5 times for the transverse stiffener specimens when $m = 3$ was used. Moreover, using $m = 5$ resulted in a greater and more accurate prediction of the fatigue improvement due to HFMI treatment. The proposed VA design *S-N* curves are plotted against the experimental data in Figure 3.14.

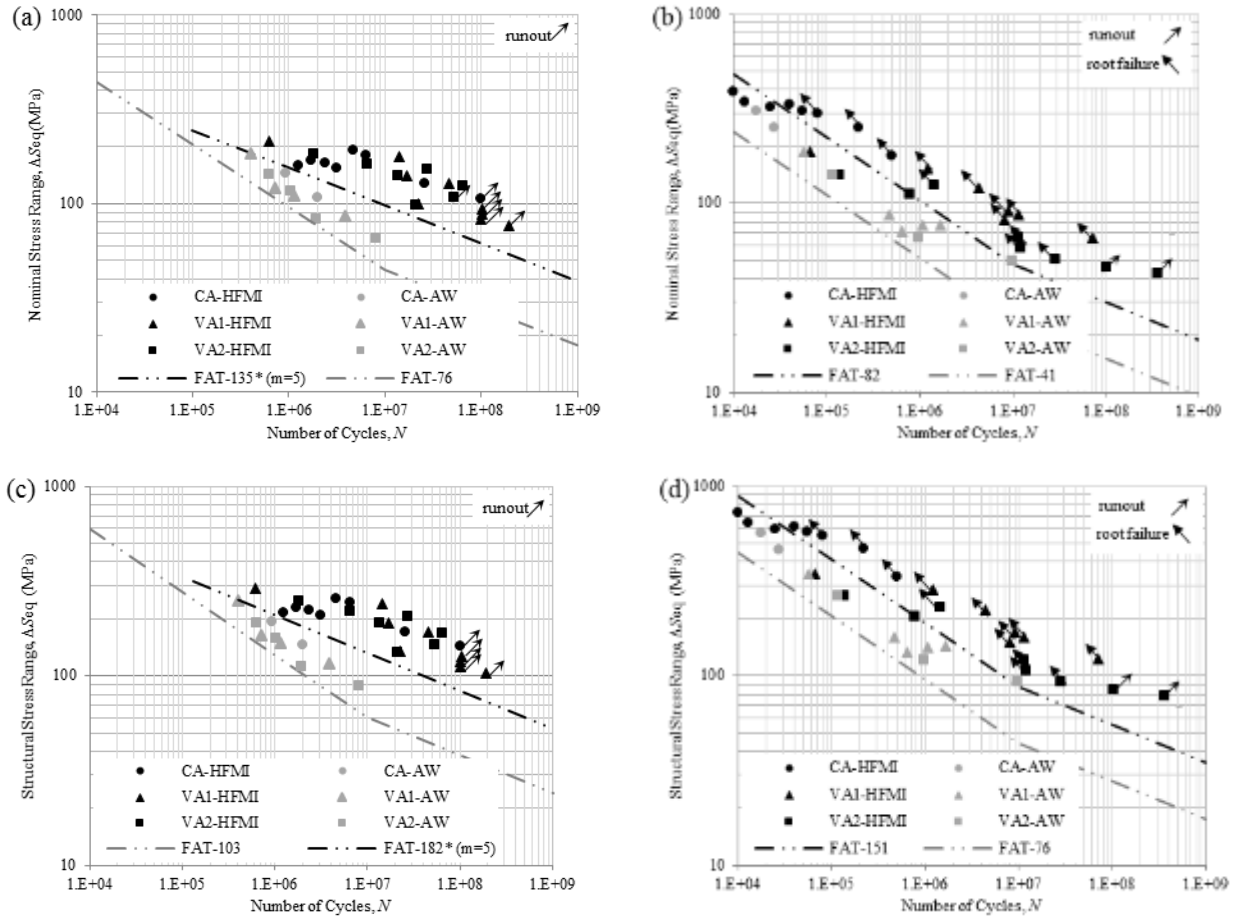

Figure 3.14: Proposed VA fatigue design curves: (a) and (c) Type-X; (b) and (d) Type-L

A similar statistical analysis was performed on the effective notch stress results and the VA fatigue resistance and design curves were similarly established (Table 3.6).

Table 3.6: Characteristic S-N curve data (effective notch stress)

Failure location/ Condition	Calculated m	Calculated ΔS_{2m} (p_f = 50%)	Assigned m	FAT class (MPa)
Toe/ As-welded	2.84	239	3	175
Root/ As-welded	3.57	479	3	279
Toe/ Treated	4.27	487	3	216
			5	339

A set of *S-N* curves with m = 3 for untreated and m = 5 for treated welds is presented in Figure 3.15. Similar to the nominal and structural stress approaches, an *S-N* curve with m = 5 was found to be an appropriate effective notch stress design curve for the treated weld toes in the long life domain.

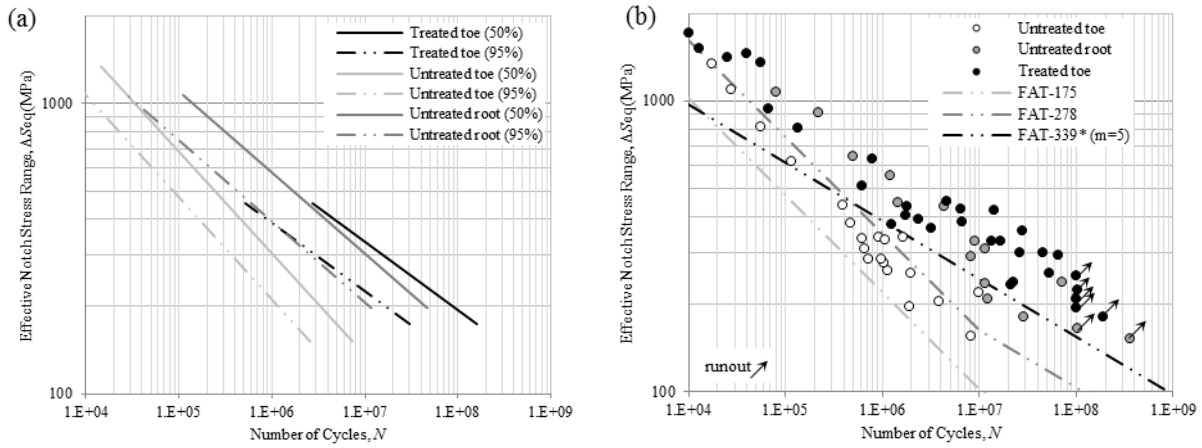

Figure 3.15: Effective notch stress analysis results: (a) VA fatigue resistance curves; (b) proposed VA fatigue design curves

To the further evaluation of the proposed treated weld toe design curves, the curves were plotted against the CA (R = 0.1) and CA-UL (CA loading with periodical compressive underload) test results for "properly" HFMI treated specimens reported in [9], in addition to the results from the current study. The specimens used [9] were fabricated using a similar material and welding process to those used in the current study. The specimen geometry had similar dimenssion to the Type-X specimen.

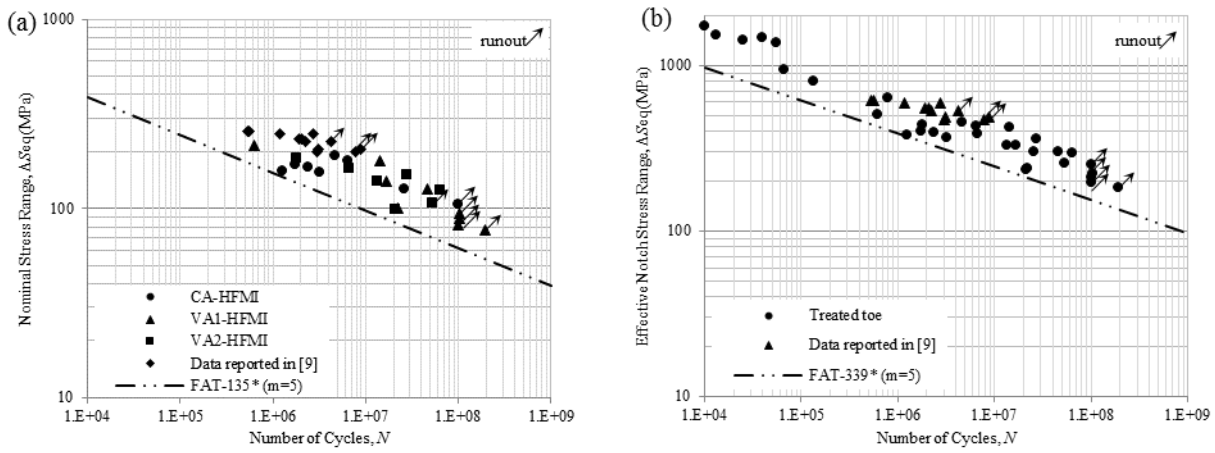

Figure 3.16: Proposed fatigue resistance curves for treated weld toes: (a) nominal stress; (b) effective notch stress

As can be seen in Figure 3.16, all of fatigue test results reported for the treated weld toes in [9] also lie well above the proposed design curves in both cases, further validating these curves.

3.8 Discussion and Concluding Remarks

A comprehensive variable amplitude (VA) fatigue testing program and analysis was conducted, aimed at addressing some of the concerns raised regarding the use of high frequency mechanical impact (HFMI) treatments for bridge welds in the high and ultra-high cycle regime. Two distinct welded joint types representing load-carrying and non-load carrying welds in steel structures such as bridges were studied under two simulated in-service VA loading histories typical for highway bridges. Multiple constant amplitude (CA) fatigue tests were also conducted for comparison purposes. Various approaches to predict the fatigue performance of the treated joints, especially in the long life regime, were evaluated using the generated pool of data. Both the nominal and structural stress approaches and the effective notch stress approach were considered and finite element (FE) analyses were performed to calculate the structural stress and effective notch stress concentration factors.

For the transverse stiffener (Type-X) specimens, the HFMI treatment resulted in a significant fatigue strength improvement in all cases. The failure mode did not change after applying the treatment and all of the specimens that failed did so as a result of cracks initiating at the weld toe. The proposed design provisions to account for the benefit of the treatment were found to be rather conservative. Based on a statistical analysis of the test results, $m = 5$ was recommended instead of the traditional $m = 3$ to determine the equivalent stress range for treated weld toes under VA loading. Consequently, FAT-180*

with $m = 5$ was proposed for the structural stress design of treated Type-X details. Similarly, FAT-339* with $m = 5$ was proposed for the effective notch stress design of the treated weld toes.

Treating the weld toe in the lap joint (Type-L) specimens resulted in shifting the failure mode from the weld toe to the weld root in cases where the peak tensile stress was not excessive. Significant fatigue life improvements were still achieved, despite this shift in the failure mode. FAT-135* with $m = 5$ was proposed for the nominal stress design of treated Type-L details.

While little or no fatigue improvement is currently considered in [29] for treated weld toes under loading histories with high mean stresses, specifically with $R > 0.4$, significant fatigue life improvements were still achieved under a VA loading history (specifically, VA2) where more than 50% of the cycles in the loading spectrum had R ratios higher than 0.4. Within the scope of this study, which considered realistic loading histories for steel bridges, this parameter did not seem to be a crucial factor.

The IIW Recommendations [22] currently limit the maximum applied nominal stress to $0.8 \cdot f_y$ for impact treated welds. Several fatigue tests were conducted under VA loading histories with nominal overloads of 0.9, 1.0, and $1.1 \cdot f_y$. While the treated transverse stiffener (Type-X) specimens still exhibited some degree of fatigue improvement under these loading conditions, all of the treated lap joint (Type-L) specimens that experienced overloads with a magnitude of $1.0 \cdot f_y$ or higher failed at their primary failure location (i.e. the weld toe), without any fatigue life improvement. In other words, the beneficial effect of the treatment at the weld toe was completely undone by the severe overloads. This highlights the need to use a local, e.g. structural stress, approach to determine the magnitude of the maximum allowable overload (or underload) stress for treated weld details. Within the scope of this paper, it is recommended to limit the nominal maximum stress to $1.15 \cdot f_y / K_{st}$.

The constant amplitude fatigue limit (CAFL) of 110 MPa (nominal stress) for the treated transverse stiffener (Type-X) detail proposed in [12] was found to be a reasonable limit. No CA fatigue test failure was observed below this limit and several runout VA tests had a maximum stress range even larger than 110 MPa. For the treated lap joint specimens, a CAFL of 48 MPa (nominal fatigue strength at 10^7 cycles) corresponding to weld root cracking is recommended.

Chapter 4

Testing and Measurements to Determine Model Parameters for Fatigue Analysis

4.1 Introduction

A strain-based fracture mechanics (SBFM) model is used in Chapter 5 to predict the effectiveness of a high frequency mechanical impact (HFMI) treatment applied to welded details. The model is evaluated using the experimental results and found to be an effective means for predicting the fatigue lives for both the as-welded and impact treated specimens for all of the studied loading conditions reported in Chapter 3. Using this analytical model, which is discussed in detail in Chapter 5, requires a number of input parameters that can only be determined from laboratory testing and measurement. Towards this end, a series of materials tests were conducted to determine accurate material properties and to get a better understanding of the material cyclic behaviour.

Crack growth under variable amplitude (VA) loading can be largely explained through changes in fatigue crack closure and crack opening stress. A recently developed methodology [1, 2] was used for modelling changes in the crack opening stress level and fatigue damage using data derived from periodic underload fatigue tests of smooth specimens. The effective strain-life data, crack closure parameters, and effective crack growth data were obtained for the HAZ-simulated 350W steel. Microhardness measurements were also made to study the effect of impact treatment on the microstructure of the material in the vicinity of the treated weld toe. Weld toe geometry measurements were made to characterize the weld shape and weld defects. Finally, residual stress measurements were obtained to determine the actual residual stress distribution on and below the weld toe surface.

4.2 Materials Testing Procedures and Measurements

A comprehensive materials testing program was carried out to determine several parameters that are required to use the analytical modelling approach investigated in this study. Uniaxial and cyclic testing were conducted on smooth specimens to derive the effective strain-life curve. Crack closure parameters (including the steady state crack opening stress and the crack opening stress parameter μ) were then determined. Crack growth experiments were also conducted to determine the fatigue crack growth parameters and to validate the employed methodology.

4.2.1 Material

The material used in this study was CSA 350W steel, which is a steel grade commonly used in Canadian bridges. The chemical composition for this type of steel should meet the requirements of CSA G40.20/ G40.21 [3]. The typical chemical composition is presented in Table 4.1.

Table 4.1: Chemical composition of 350W steel (percentage by weight)

C	Mn	P	S	Si
0.23	0.50-1.50	0.04	0.05	0.35

Fatigue cracks in the welded joints initiate and grow in the heat affected zone (HAZ). The material in the HAZ is harder than the original base metal due to the heating cycle that it experiences during the welding process [4]. Figure 4.1 shows an etched, cut Type-X specimen. The base metal, weld metal, HAZ, and crack initiating at the weld toe are clearly visible. Hardness measurements have shown that the HAZ was 8-10% harder, in Rockwell B (HRB) scale, than the base metal.

A HAZ simulating procedure was explored in this study to mimic the actual properties at the fatigue crack initiation site in the materials test samples. In this procedure, the cut but un-machined 9.5 mm thick samples were first heated to 990 °C in an oven for 30 minutes. After being removed from the oven, the samples were immediately placed between two large circular disks for "mass-quenching" to room temperature. In this procedure, the temperature (990 °C) was chosen to simulate the maximum temperature that is generated during the welding process, the timing (30 minutes) was chosen for the 9.5 mm pieces according to the relevant curves to achieve an isothermal condition across the thickness, and the two large disks simulated the as-received base metal (non-heated mass) which surrounds the HAZ in the welded location. Following this procedure, the hardness in the samples was increased from 89 to 94 HRB which was close to the increase in the hardness of the actual weldments.

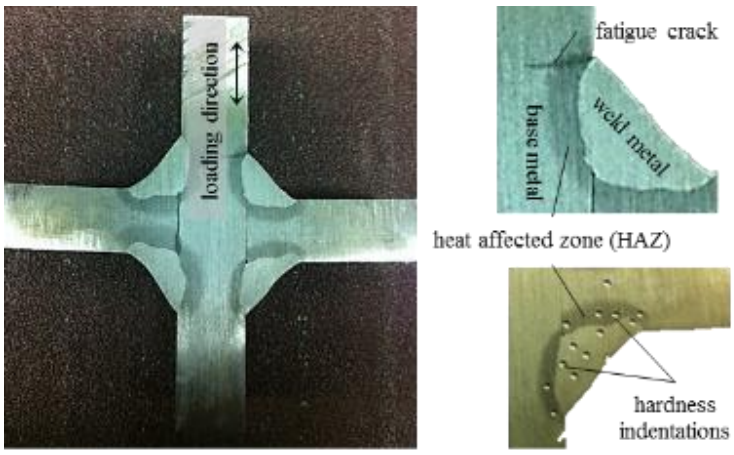

Figure 4.1: Typical fatigue cracking and HAZ in test specimens

4.2.2 Specimen Geometries

Three pre-cracked compact tension (CT) specimens, fabricated in accordance with the ASTM E647 [5], and 40 smooth specimens were fabricated of the same 350W steel used in the fabrication of the small-scale fatigue specimens. Polished smooth cylindrical, variable width specimens were used for cyclic materials testing and the CT specimens were used for fatigue crack growth testing. The specimen geometries are presented in Figure 4.2.

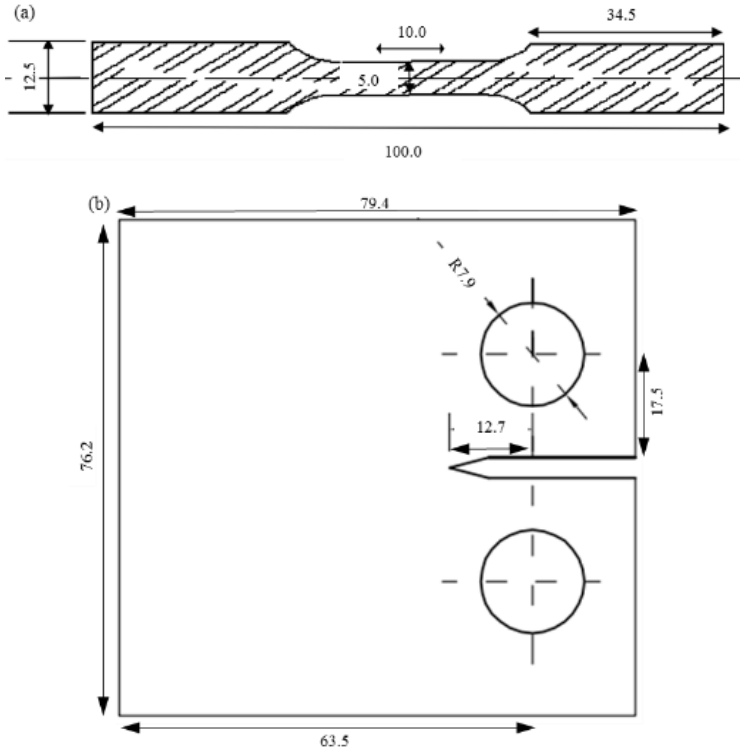

Figure 4.2: Specimen geometries: (a) 9.5 mm thick smooth specimen; (b) 9.5 mm CT specimen

4.2.3 Specimen Gripping and Alignment

All fatigue tests were conducted using an MTS servo-controlled closed-loop electro-hydraulic testing machine. A process control computer controlled by FLEX software [6] was used to output the strain and stress amplitudes for strain and stress-controlled tests, respectively. Figure 4.3 shows the typical gripping assembly for a smooth cylindrical specimen. The load train alignment including the load cells, the grips, the specimen, and the actuator was checked prior to starting the materials testing program. The smooth specimens were inserted and secured into the lower grip and the hydraulic actuator was then raised until the other end of the specimen was inserted and secured into the upper grip. For strain-controlled tests, an axial extensometer was mounted and held in place by two wire springs.

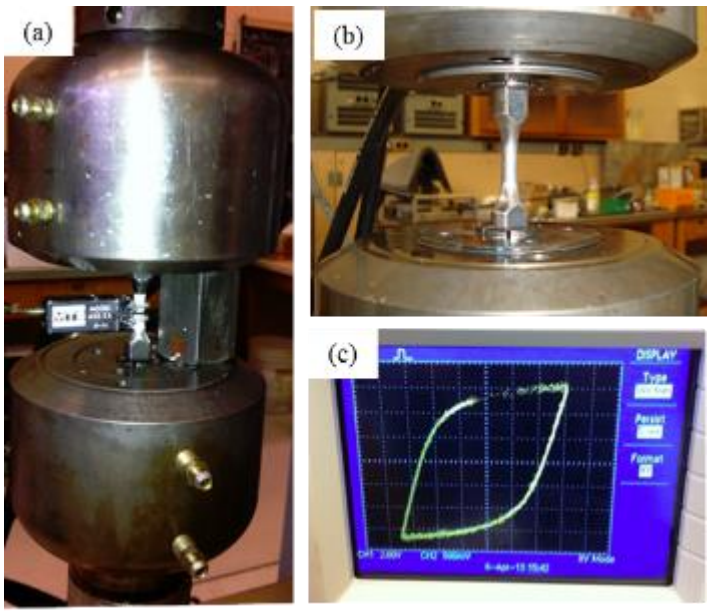

Figure 4.3: Test setup for smooth specimens: (a) and (b): grips and extensometer; (c) typical hysteresis loop

Figure 4.4 shows the gripping assembly for the CT specimens. The testing was conducted using the same loading frame used for the smooth specimens. The CT specimens were inserted and secured into the lower grip and the hydraulic actuator was then raised until the other end of the specimen was inserted and secured into the upper grip. The specimens were held by using two custom made bolts, which were tightened in the absence of any applied load. A travelling optical microscope (360x magnification) was mounted on the machine facing the specimen. A Vernier (with 0.001 mm accuracy) was attached to the microscope and used to measure changes in the crack length.

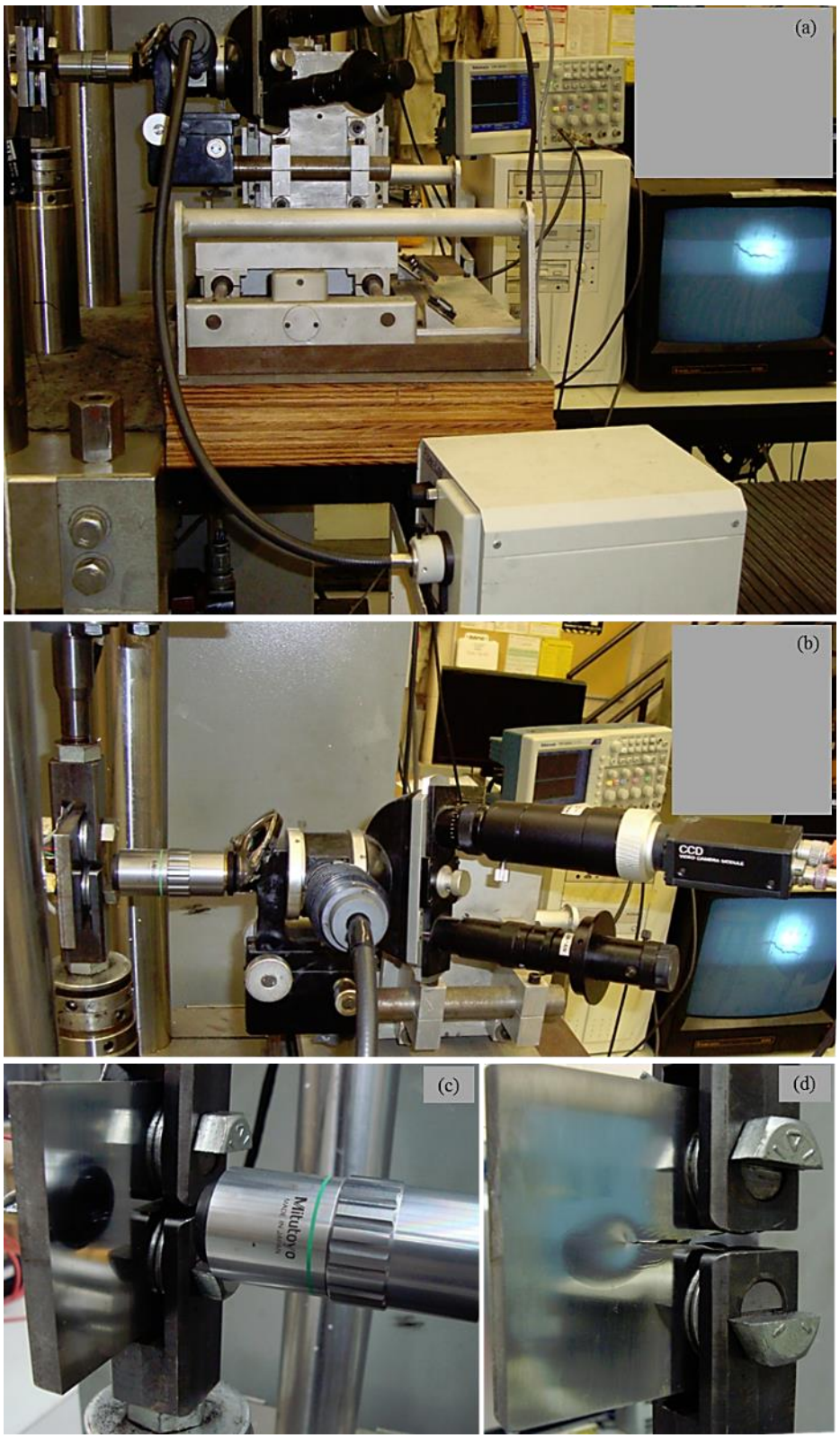

Figure 4.4: Test setup for CT specimens: (a), (b), and (c): different parts of the setup including the 360x short focal length optical microscope; (d) final opened crack in (not included in the results)

4.2.4 Static and Cyclic Materials Tests

The static tension and cyclic materials tests were conducted in accordance with ASTM E8 [7] to determine the static and cyclic material properties. All specimens were carefully inspected and their dimensions were measured at three different points along the reduced cross section prior to testing.

Equation 4.1 presents the monotonic Ramberg-Osgood stress-strain relationship where ε is the total (the elastic and plastic) true strain, σ is the true stress, E is the elastic modulus, K is the strength coefficient, and n is the strain hardening exponent:

Equation 4.1: $$\varepsilon = \frac{\sigma}{E} + \left(\frac{\sigma}{K}\right)^{1/n}$$

Equation 4.2 presents and the cyclic Ramberg-Osgood model where K' and n' are the cyclic strength coefficient and the cyclic strain hardening exponent, respectively:

Equation 4.2: $$\varepsilon = \frac{\sigma}{E} + \left(\frac{\sigma}{K'}\right)^{1/n'}$$

A cyclic Ramberg-Osgood material model is used in Chapter 5 to determine the stresses and strains for each load cycle. Equation 4.3 presents the equation for the hysteresis loop where $\Delta\varepsilon$ and $\Delta\sigma$ are the changes in the strain and stress, respectively:

Equation 4.3: $$\Delta\varepsilon = \frac{\Delta\sigma}{E} + 2\left(\frac{\Delta\sigma}{2K'}\right)^{1/n'}$$

Mechanical (monotonic and cyclic) properties of the HAZ-simulated 350W steel were determined as discussed in the following two sections.

4.2.5 Monotonic Tension Tests

Figure 4.5 shows a typical stress (σ) – strain (ε) curve obtained for the HAZ-simulated 350W steel tested in the study. Ramberg-Osgood stress-strain curve constants were determined by graphical curve fitting and minimizing the least squares parameters (Equation 4.4 and Table 4.2).

Equation 4.4**:** $$\varepsilon = \frac{\sigma}{208083} + \left(\frac{\sigma}{494}\right)^{1/0.036}$$

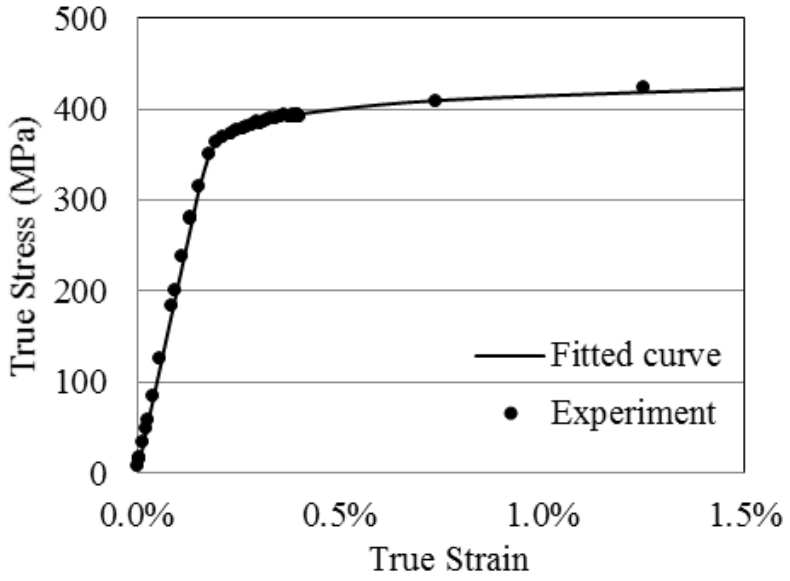

Figure 4.5: Monotonic tension test results

Table 4.2: Mechanical (monotonic) properties of HAZ simulated 350W steel

Parameter		Units	Magnitude
Elastic Modulus	E	MPa	208,083
Yield strength	S_y	MPa	356
Ultimate tensile strength	S_u	MPa	616
Elongation		%	32
Monotonic tensile strength coefficient	K	MPa	494
Monotonic tensile strain hardening exponent	n	-	0.036
Reduction in area		%	49
True fracture strain	ε_f	%	70

4.2.6 Cyclic Tests

Fully reversed cyclic loading tests were conducted at ten different prescribed strains (0.1 to 1.0%) on two specimens. Figure 4.6 shows the stabilized cyclic stress-strain curve obtained for the 350W steel. Additional stabilized σ-ε data obtained during the fully reversed constant amplitude tests (discussed in the following section) are included in this figure for comparison. However, they were not used in the curve fitting procedure. The Ramberg- Osgood cyclic stress-strain curve constants were determined by graphical curve fitting and minimizing the least squares parameters (Equation 4.5 and Table 4.3).

Equation 4.5: $\varepsilon_a = \frac{\sigma_a}{208083} + \left(\frac{\sigma_a}{812}\right)^{1/0.108}$

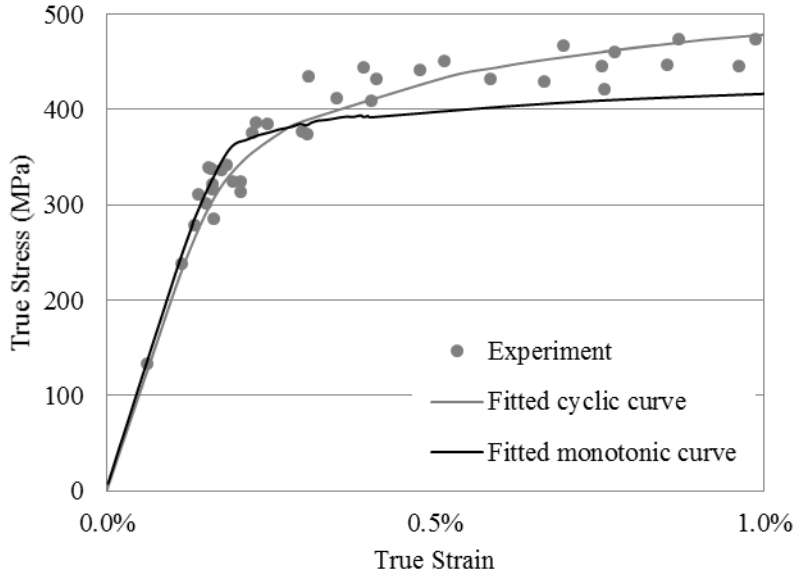

Figure 4.6: Hysteresis test results

Table 4.3: Mechanical (cyclic) properties of HAZ simulated 350W steel

Parameter		Units	Magnitude
Cyclic yield strength (0.2% offset)	σ_y	MPa	410
Cyclic tensile strength coefficient	K'	MPa	812
Cyclic tensile strain hardening exponent	n'	-	0.108

1.1. Determination of the fatigue strain-life and the effective strain-life curves

The total strain range can be expressed as the sum of the elastic ($\Delta\varepsilon_e$) and plastic ($\Delta\varepsilon_p$) strain ranges:

Equation 4.6: $$\frac{\Delta\varepsilon}{2} = \frac{\Delta\varepsilon_e}{2} + \frac{\Delta\varepsilon_p}{2}$$

Equation 4.7: $$\frac{\Delta\varepsilon_e}{2} = \frac{\sigma'_f}{E}(2N_f)^b$$

Equation 4.8: $$\frac{\Delta\varepsilon_p}{2} = \varepsilon'_f(2N_f)^c$$

where σ'_f, ε'_f, b, and c are material constants (see Table 4.5) and $2 \cdot N_f$ is the reversals to failure. Thus, the strain-life curve can be expressed as Equation 4.9 and constructed by conducting fully reversed constant amplitude tests.

Equation 4.9: $\frac{\Delta\varepsilon}{2} = \frac{\sigma'_f}{E}(2N_f)^b + \varepsilon'_f(2N_f)^c$ or $\varepsilon_a = \frac{\sigma'_f}{E}(2N_f)^b + \varepsilon'_f(2N_f)^c$

4.2.7 Strain-life Curve: Fully Reversed Constant Amplitude Tests

Twenty-one constant amplitude (CA) tests were conducted and the results were used to determine the fatigue properties of the HAZ-simulated 350W steel and to generate the total strain-life curve. Axial, fully reversed (R = -1) strain-controlled CA fatigue tests were carried out. Throughout each test, the stress-strain peaks were read and recorded at logarithmic intervals using a voltmeter. The specimens were considered failed when a 50% drop in the tensile peak load (from the peak tensile load at the estimated specimen half-life) was observed. The loading frequency of the tests varied from 0.5 to 5 Hz. To increase the testing speed for the specimens with the estimated fatigue lives greater than 10^5 cycles, the testing mode was switched to load control after the stress-strain loops (in strain-controlled mode) were stabilized. For the load-controlled tests, the loading frequencies were increased to 50 to 100 Hz and the failure was defined as the separation of the specimen into two pieces. Figure 4.7 presents the CA test results.

Table 4.4: CA test results (* runout tests)

Test #	Reversals	Total strain (%)	Elastic strain (%)	Plastic strain (%)
1	1,806	0.815	0.225	0.587
2	1,834	0.799	0.216	0.579
3	6,194	0.577	0.217	0.358
4	7,368	0.412	0.215	0.196
5	10,812	0.405	0.179	0.225
6	15,182	0.309	0.202	0.106
7	20,028	0.307	0.186	0.120
8	38,672	0.306	0.192	0.114
9	68,852	0.207	0.175	0.032
10	81,052	0.204	0.166	0.038
11	134,038	0.206	0.157	0.049
12	194,434	0.194	0.160	0.034
13	229,640	0.184	0.162	0.022
14	460,164	0.175	0.161	0.013
15	723,246	0.162	0.154	0.008
16	1,633,832	0.163	0.155	0.008
17	3,259,448	0.155	0.151	0.003
18	4,828,832	0.164	0.154	0.009
19*	10,000,000	0.134	0.134	0.000
20*	10,000,000	0.145	0.145	0.000
21*	10,000,000	0.153	0.153	0.000

The strain amplitude (50% of strain range) vs. life curve constants were determined by graphical curve fitting and minimizing the least squares parameters (Equation 4.10 and Table 4.5).

Equation 4.10: $\varepsilon_a = \frac{853}{208083}\left(2N_f\right)^{-0.072} + 0.56\left(2N_f\right)^{-0.611}$

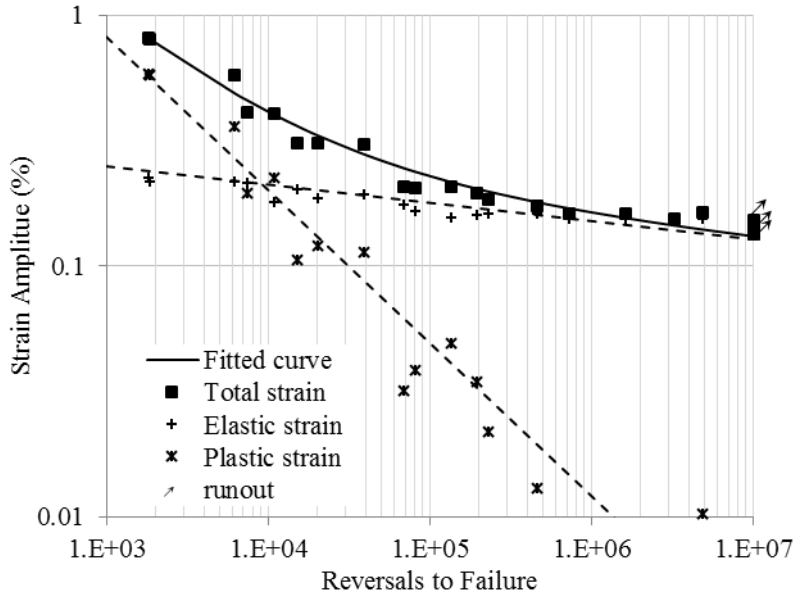

Figure 4.7: CA test results

Table 4.5: Strain-life curve constants for HAZ simulated 350W steel

Parameter		Units	Magnitude
Fatigue strength coefficient	σ'_f	MPa	853
Fatigue strength exponent	b	-	-0.072
Fatigue ductility coefficient	ε'_f	-	0.56
Fatigue ductility exponent	c	-	-0.611

4.2.8 Effective Strain-life Curve: Underload Fatigue Tests

The effective strain range, given as the difference between the maximum strain and the greater of the crack opening strain or the minimum strain in the cycle, is the range of a strain for which a fatigue crack is open during a cycle. The effective strain-life curve can be used to predict fatigue lives under a VA loading [2, 8]. In this study, it is also used to calculate the steady state crack opening stresses.

Previous work at the University of Waterloo [9, 10] introduced the following damage parameter:

Equation 4.11: $E\Delta\varepsilon^* = E\Delta\varepsilon_{eff} - E\Delta\varepsilon_i$

where $\Delta\varepsilon_{eff}$ is the effective strain range, $\Delta\varepsilon_i$ is the material's intrinsic fatigue limit strain range below which a fully open crack will not grow, and $\Delta\varepsilon^*$ is the part of the strain range that causes fatigue crack growth. It was shown later in [11] that $\Delta\varepsilon^*$ is related to the fatigue life, i.e.:

Equation 4.12: $E\Delta\varepsilon^{*} = A(N_f)^{b}$

where *A* and *b* are material constants. Following the methodology described in [1], a series of underload (UL) fatigue tests were conducted to determine the constants *A* and *b* and then to construct the effective strain-life curve for the HAZ simulated 350W steel. When using the UL tests to construct the effective strain-life curve, N_f in Equation 4.12 is the equivalent fatigue life for the small CA cycles.

Nine underload fatigue tests were conducted to construct the effective strain-life curve. These load-controlled tests were carried out under a loading history consisting of a periodic single underload (UL) cycle followed by a number of smaller CA load cycles. The CA load cycles had the same maximum stress as the UL cycle. However, the number and the minimum stress of the small cycles were varied for each test. This loading history was aimed at creating a closure free crack growth by keeping the opening stress below the minimum stress of the smaller load cycles. This was attempted by ensuring that the UL cycle occurred frequently enough in the loading spectrum. The UL cycle was set equal to the fully reversed CA stress level that corresponded to a fatigue life of 10,000 cycles based on the strain-life curve (Equation 4.10), as proposed in [12]. An underload of this magnitude causes a large reduction in the crack opening stress without expending an undue fraction of the total damage in the large cycles. The number of small cycles was chosen in a way that first, they caused 80 to 90% of the total damage to the specimen, and secondly, they were free from crack closure (i.e. the opening stress was lower than the minimum stress for all the cycles). After failure, the equivalent fatigue life for the small cycles in the UL tests was determined by calculating the damage fraction caused by the UL cycles (1/10,000 per occurrence) and subtracting it from unity. The total number of small cycles was then divided by the fraction of the damage that they had caused to calculate the equivalent fatigue life for the CA load cycles. The CA strain ranges and their corresponding equivalent fatigue lives were used to construct the effective strain-life curve (Equation 4.14). Figure 4.8 presents the UL test results.

Table 4.6: UL test data (* runout)

Test #	CA cycles strain range (%)	# of CA cycles	Reversals to failure	Damage % by UL cycles	Damage % by CA cycles	Equivalent CA reversals
1	0.159	100	540,000	26.73%	73.27%	737,027
2	0.147	200	646,210	16.07%	83.93%	769,984
3	0.144	250	1,004,000	20.00%	80.00%	1,255,000
4	0.131	400	1,053,848	13.14%	86.86%	1,213,275
5	0.120	700	2,381,436	16.99%	83.01%	2,868,716
6	0.116	1,000	3,900,000	19.48%	80.52%	4,843,548
7	0.110	2,000	7,454,440	18.63%	81.37%	9,160,803
8	0.092	4,000	9,607,176	12.01%	87.99%	10,917,986
9*	0.075	10,000	20,000,000	10.00%	90.00%	22,222,222

To obtain the *A* and *b* constants and construct the effective strain-life curve, first a value was chosen for $\Delta\varepsilon_i$ in such a way that the curve of $\Delta\varepsilon^*$ versus N_f was linear on a logarithmic scale (Equation 4.12). For curve fitting purposes, an additional data point was added to the UL curve. This extra point was added by calculating the effective strain range at 2% total strain range assuming that the crack in the 2% strain range CA test opens at one half the minimum stress [13]. When the values of *A, b,* and $\Delta\varepsilon_i$ were determined, the effective strain-life curve was constructed using Equation 4.13:

Equation 4.13: $$\Delta\varepsilon_{eff} = \frac{\mathrm{A}}{E}\left(2N_f\right)^{\mathrm{b}} + \Delta\varepsilon_i$$

The effective strain-life curve constants were determined by graphical curve fitting and minimizing the least squares parameters. The curve and the corresponding parameters are presented in Equation 4.14 and Table 4.7:

Equation 4.14: $$\Delta\varepsilon_{eff} = 56.11\left(2N_f\right)^{-0.498} + 0.085$$

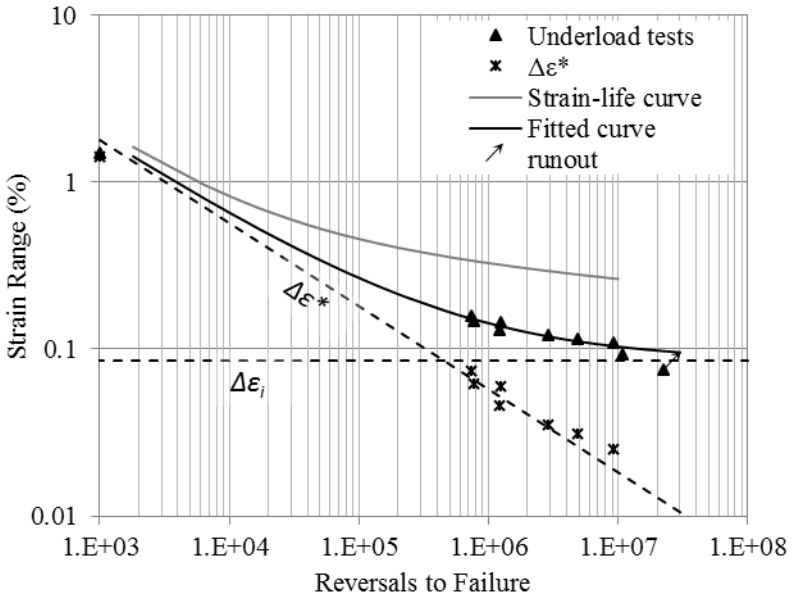

Figure 4.8: Fitted effective strain-life curve

Table 4.7: Effective strain-life curve parameters for HAZ-simulated 350W steel

Parameter	Units	Magnitude
Underload cycle	MPa	±349
A/E	-	56.11
b	-	-0.498
Δεi	%	0.085

4.2.9 Estimating Steady-state Crack Opening Stress

A formula proposed in [14] was used to model the steady state crack opening stress:

Equation 4.15: $$S_{opss} = \theta S_{max}\left(1-\left(\frac{S_{max}}{\sigma_y}\right)^2\right)+\varphi S_{min}$$

where S_{opss} is the steady state crack opening under CA loading, S_{max} and S_{min} are the nominal maximum and minimum stresses in a smooth specimen (or the local maximum and minimum stresses at the notch root in a notched specimen, respectively), σ_y is the cyclic yield stress, and θ and φ are two experimentally determined material constants.

Along with the described crack closure model, a model proposed in [15] was used to relate the change in the crack opening stress in a given cycle (ΔS_{op}) to the difference between the current opening stress (S_{cu}) and the steady state crack opening stress (S_{opss}):

Equation 4.16: $$\Delta S_{op} = \mu\left(S_{opss} - S_{cu}\right)$$

where μ is a material constant.

4.2.10 Using the Effective Strain-life Curve to Calculate the Steady-state Crack Opening Stress

Following the procedure described in [1], values for θ, φ, and μ can be experimentally determined. In this study, the CA and effective strain-life curves were used to estimate the steady state crack opening stress. As derived in Equation 4.17, the difference between the strain range at a given fatigue life in a fully reversed CA strain-life curve, $\Delta\varepsilon_{CA}$, and that in the effective strain-life curve at the same fatigue life, $\Delta\varepsilon_{eff}$, is equal to the difference between the CA test minimum strain, ε_{min}, and the estimated crack opening strain, S_{op}, in the CA cycle:

Equation 4.17: $$\Delta\varepsilon_{CA} - \Delta\varepsilon_{eff} = \left(\varepsilon_{max} - \varepsilon_{min}\right) - \left(\varepsilon_{max} - \varepsilon_{op}\right) = \varepsilon_{op} - \varepsilon_{min} = \frac{S_{op} - S_{min}}{E}$$

Thus, the CA crack opening stress, S_{op}, can be estimated by using the CA and effective strain-life data in conjunction with Equation 4.18:

Equation 4.18: $$S_{op} = S_{min} + E\left(\Delta\varepsilon_{CA} - \Delta\varepsilon_{eff}\right)$$

The values for S_{op} can then be used to determine the constants in Equation 4.15 by fitting this equation to the data obtained from Equation 4.18.

Using the constants previously calculated for the strain-life and the effective strain-life data, the estimated crack opening stress was calculated (Equation 4.19) and is presented in Figure 4.9 and Table 4.8.

Equation 4.19: $$S_{opss} = 0.448\sigma_{max}\left(1 - \left(\frac{\sigma_{max}}{410}\right)^2\right) + 0.024\sigma_{min}$$

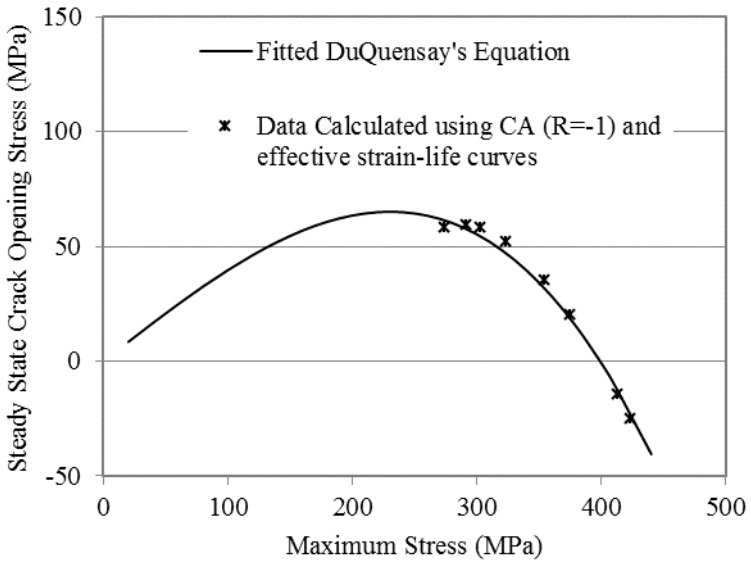

Figure 4.9: Steady-state crack opening stress for the HAZ-simulated 350W steel

Table 4.8: Steady-state crack opening stress equation parameters

Parameter	Units	Magnitude
Constant - θ	-	0.448
Constant - φ	-	0.024

4.2.11 Estimating the Crack Opening Stress Parameter μ: Damage Tests

Following the procedure described in [1], another test series was used to estimate the crack opening stress buildup parameter μ in Equation 4.16. This parameter describes the recovery of the crack opening stress to its steady state level. Fatigue tests were conducted on smooth specimens under load histories consisting an underload cycle which was followed by a number of smaller CA cycles. The frequency of occurrence of the underloads was varied for each test by changing the number of small CA cycles. The changes in the fatigue lives were tracked during the testing program. These changes in damage per loading block (consisting of one UL cycle and the following CA cycles) were then used to determine the value of *m*.

Eight underload fatigue tests were carried out for this purpose. The underload cycle was set equal to the fully reversed constant amplitude stress level corresponding to the fatigue life of 10,000 cycles [12]. The small cycles had the same maximum stress as the UL cycle. The stress range of the CA cycles was

constant in all of the eight tests and only the number of small cycles per block was varied from test to test. These tests were conducted in load control and specimens were considered to have failed when they separated into two pieces. After failure, the equivalent damage done by the small CA cycles was calculated and the damage per cycle was plotted against the number of cycles per block. Next, this data was fitted by iteratively assuming values for μ and using Equation 4.16 to calculate the crack opening stress for each small cycle in the loading block. Then, the effective strain range was calculated for each cycle using Equation 4.18 and the damage per cycle was calculated using the effective strain-life curve. Finally, the average damage per cycle was estimated by summing the damage per cycle (calculated in the previous step) and dividing it by the number of small cycles in each block.

Table 4.9: Damage fatigue test results

Test #	#of CA cycles	Cycles to failure	Damage % by UL cycles	Damage % by CA cycles	Equivalent CA cycles	Damage per cycle
1	10	85,767	77.97%	22.03%	389,319	2.57E-06
2	30	152,577	55.67%	44.33%	344,185	2.91E-06
3	50	38,301	7.51%	92.49%	41,411	2.41E-05
4	60	55,432	9.09%	90.91%	60,973	1.64E-05
5	80	146,043	18.03%	81.97%	178,166	5.61E-06
6	100	460,459	45.59%	54.41%	846,276	1.18E-06
7	200	650,083	34.83%	65.17%	997,519	1.00E-06
8	500	522,543	10.43%	89.57%	583,391	1.71E-06

In this study, each loading block consisted of a UL cycles of ±349 MPa followed by a number of CA cycles of ±180 MPa. Considering the data reported in [2] for parameter μ for three different steel grades and the experimental results in this section (Figure 4.10), a value of 0.018 for μ seems to be a reasonable estimate. However, it is worth noting the high degree of scatter observed for this parameter.

Equation 4.20: $\Delta S_{op} = 0.018\left(S_{opss} - S_{cu}\right)$

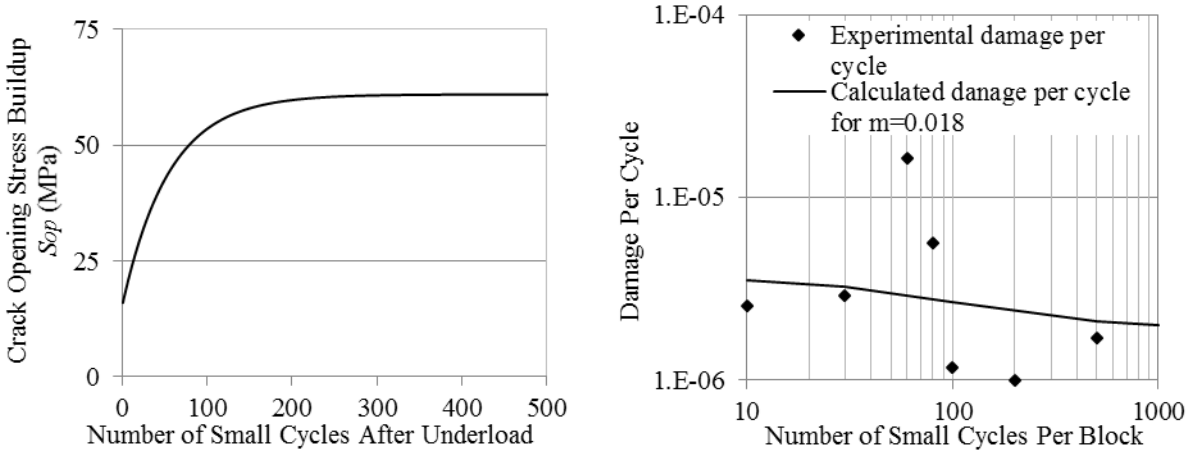

Figure 4.10: Derived crack opening stress buildup data

4.2.12 Derivation of the Closure Free Crack Growth Curve and Closure Free Crack Growth Measurements: Crack growth tests

Three pre-cracked compact tension (CT) specimens, one HAZ-simulated and two as-received, were fatigue tested under the stress ratios between 0.8 and 0.9. These stress ratios were high enough that no crack closure was observed. The specimen geometry, fabrication process, and fatigue testing procedure and parameters all were in accordance with ASTM E647. These tests were conducted to derive crack growth parameters (*C* and *m* constants) for both the HAZ-simulated and as-received 350W steel used in this study.

Equation 4.21 shows the Paris-Erdogan (1963) crack growth law for a growing crack:

Equation 4.21: $$\frac{da}{dN} = C(\Delta K)^m$$

where ΔK is the stress intensity factor (SIF) range. Each SIF is determined using Equation 4.22:

Equation 4.22: $K = Y\Delta\sigma\sqrt{\pi a}$ or $K = YE\,\Delta\varepsilon\sqrt{\pi a}$

In this equation, *Y* is a correction factor which accounts for the geometry and crack shape, *E* is the modulus of elasticity of the material, *a* represents the (crack) depth below the surface, and σ and ε are the local stress and strain, respectively, at this depth.

The work by Elber in 1970 [16] showed that there exists a threshold SIF range (ΔK_{th}) below which fatigue cracks do not propagate. Equation 4.23 is the modified Paris law that accounts for crack closure.

Equation 4.23: $\frac{da}{dN} = C'(\Delta K - \Delta K_{th})^{m'}$

When expressed in terms of the effective strain range, the effective strain intensity is defined [17] as:

Equation 4.24: $\Delta K_{eff} = FE\,\Delta\varepsilon_{eff}\sqrt{\pi\left(a + a_0\right)}$

Equation 4.25: $a_0 = \frac{1}{\pi}\left(\frac{\Delta K_i}{FE\Delta\varepsilon_i}\right)^2$

where F is a shape factor, $\Delta\varepsilon_{eff}$ is the effective strain range, ΔK_i is the intrinsic threshold strain intensity, and a_0 is a constant as defined in Equation 4.25. The effective crack growth curve can then be expressed in the following from [18]:

Equation 4.26: $\frac{da}{dN} = B(\Delta K_{eff} - \Delta K_i)^n = B(\Delta K^*)^n$

where B and n are material constants.

No significant difference in crack growth behaviour was observed between the HAZ-simulated and as-received specimens. All the test results were therefore used to determine the crack growth parameters. Figure 4.11 presents the crack growth results along with the fitted crack growth curves (Equation 4.21 and Equation 4.23). The derived equations for the fitted curves are presented in Equation 4.27 and Equation 4.28. The constants were determined by graphical curve fitting and minimizing the least squares parameters. A summary of the derived parameters is presented in Table 4.10.

Equation 4.27: $\frac{da}{dN} = 4.7\cdot10^{-12}(\Delta K)^{3.06}$ for $\Delta K > 2.54$ MPa$\sqrt{\text{m}}$

Equation 4.28: $\frac{da}{dN} = 1.3\cdot10^{-10}(\Delta K - 2.54)^{2.01}$

Equation 4.29 and Figure 4.11 present the closure free crack growth curve derived using the effective strain-life curve.

Equation 4.29: $\frac{da}{dN} = 1.2\cdot10^{-10}(\Delta K_{eff} - 2.5)^{2.10}$

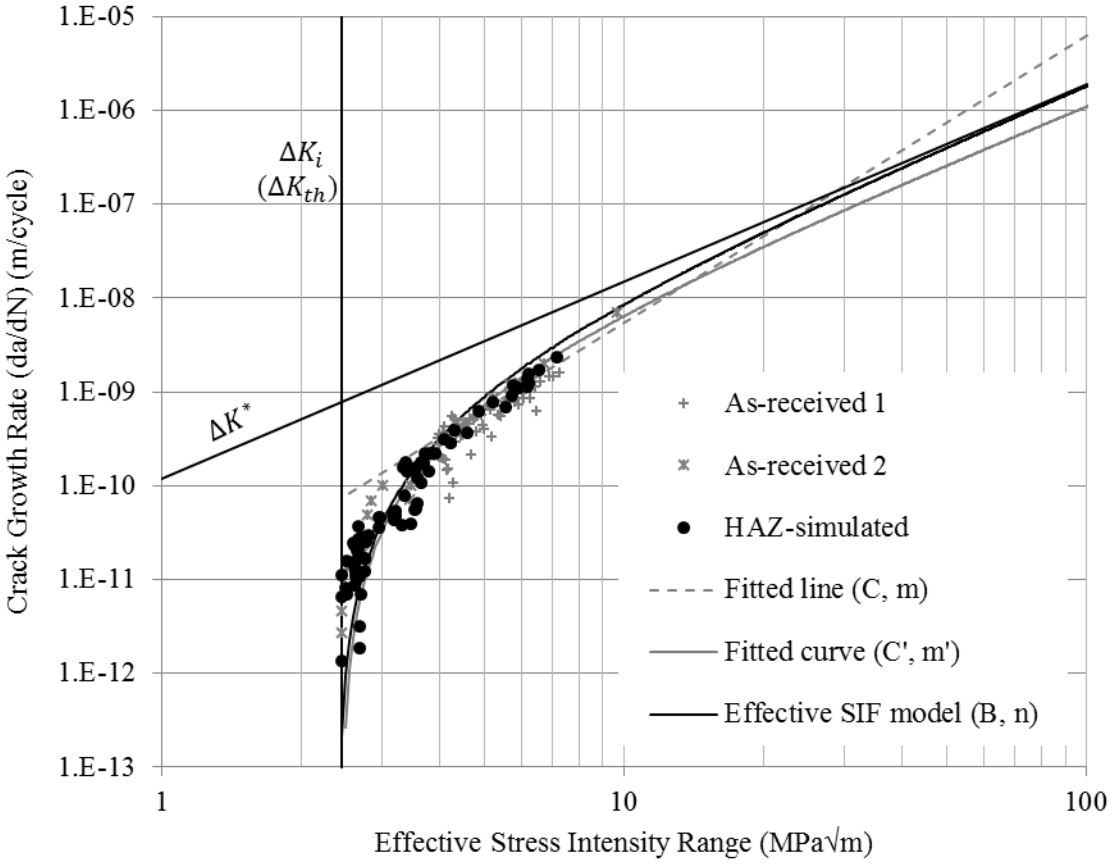

Figure 4.11: Experimental crack growth rate versus effective SIF range for 350W steel

Table 4.10: Crack growth curve parameters

Parameter	Units	Magnitude
C (Equation 4.21)	N, m	$4.7 \cdot 10^{-12}$
m (Equation 4.21)	-	3.06
C' (Equation 4.23)	N, m	$1.1 \cdot 10^{-10}$
m' (Equation 4.23)	-	2.01
ΔK_{th} (Equation 4.23)	MPa√m	2.54
B (Equation 4.26)	N, m	$1.2 \cdot 10^{-10}$
n (Equation 4.26)	-	2.10
ΔKi (Equation 4.26)	MPa√m	2.50

A procedure based on the methodology described in [1] was followed to derive the closure free crack growth curve (Equation 4.29) from the effective strain-life curve (Equation 4.14). In this procedure, a crack growth curve that predicted the observed fatigue lives (of the smooth specimens in the materials testing program) was chosen. The following steps were used to derive Equation 4.29:

1- The log-log linear portion of the crack growth curve (Equation 4.26) was derived from the log-log linear portion of the effective strain-life curve (Equation 4.12). To start, ΔK_i and n were set equal to 2.50 MPa$\sqrt{m}$ and 2 as suggested by [18], and an initial value of $2 \cdot 10^{-12}$ was chosen for B.
2- ΔK_1^* corresponding to a low strain level $\Delta\varepsilon_1^*$ (e.g. 0.05%) was calculated using Equation 4.24 and Equation 4.25. Here, the subscript (1) refers to the step number.
3- $(da/dN)_1$ was estimated for ΔK_1^* based on the curve set up in Step 1.
4- N_{f1} was calculated using the following equation, where the final crack (a_f) was taken as the half of the specimen width (2.5mm):

Equation 4.30: $$N_f = \int_{a_0}^{a_f} \frac{1}{C}\left(\Delta K^*\right)^n da$$

5- N_{f1} was compared with the observed fatigue life for $\Delta\varepsilon_1^*$ (Equation 4.12).
6- If the calculated life was different than the actual life, the constant B was changed accordingly and Step 5 was repeated until the calculated life matched the observed life. The Constant B was found at the end of this step.
7- To find the slope n, ΔK_2^* corresponding to a high strain level $\Delta\varepsilon_2^*$ (e.g. 0.5%) was calculated using Equation 4.24 and Equation 4.25 and $(da/dN)_2$ was determined.
8- N_{f2} was calculated using Equation 4.30 and compared with the observed life. If different, n was changed accordingly until the calculated life matched the observed life.

The curve given by these constants in Equation 4.29 was found to be in good agreement with the fitted curve (Equation 4.28) for the effective crack growth curve.

4.3 Microhardness Measurements and Microstructure

It has been shown that impact treatments improve the fatigue performance of welds primarily by introducing beneficial compressive residual stresses, which cause cracks to grow at a slower rate during the early stages of crack propagation. Depending on the treatment method, secondary treatment effects such as the modification of the weld toe geometry and near-surface hardness may also affect the fatigue behaviour. The effect of impact treatment on the near-surface hardness of the fatigue specimens was investigated by conducting microhardness tests on the heat affected zone (HAZ) of the as-welded and

treated specimens. Microstructure pictures were also taken to obtain a better understanding of the microstructure of a treated weld.

4.3.1 Microstructure of the Treated Weld

Two untested fatigue specimens, one as-welded and one treated, were sectioned and cast in epoxy. The samples were then prepared in accordance with ASTM E3 [19] by polishing to produce a smooth, pit-free surface. Prior to microhardness measurements, the specimen surface was etched with a 2% Nital solution to reveal the microstructure (grains and grain boundaries). Photos were then taken through a microscope at X10-50 magnification to observe grain boundaries in the microstructure of the steel.

Figure 4.12and Figure 4.13 show the microstructures of the treated specimens. The compressed region near the surface is apparent in both figures. A number of defects that can act as the initial crack under fatigue testing can also be seen in these figures. Defect depths were defined as the longest dimension perpendicular to the surface.

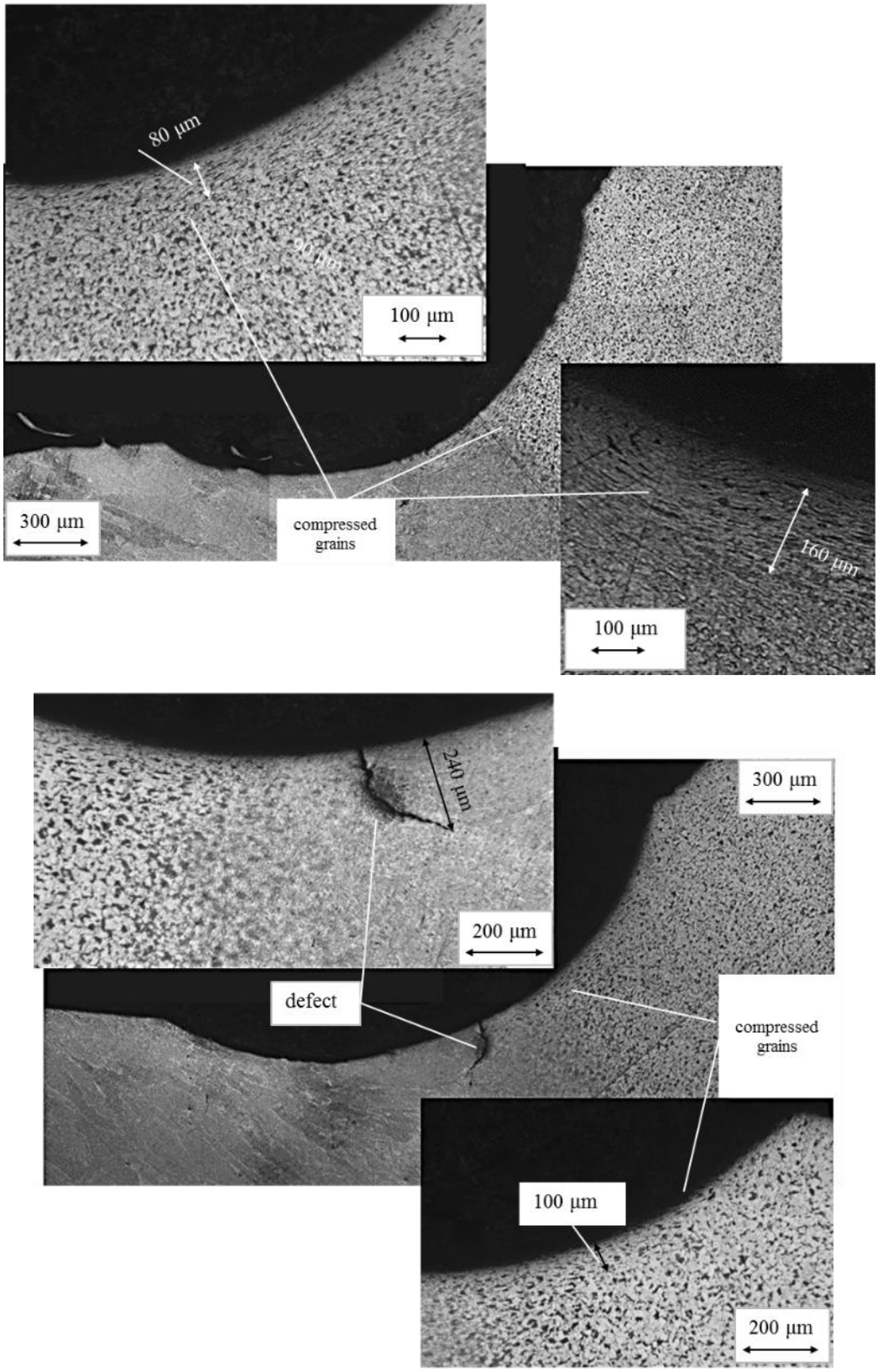

Figure 4.12: Microstructure of treated Type-X specimen

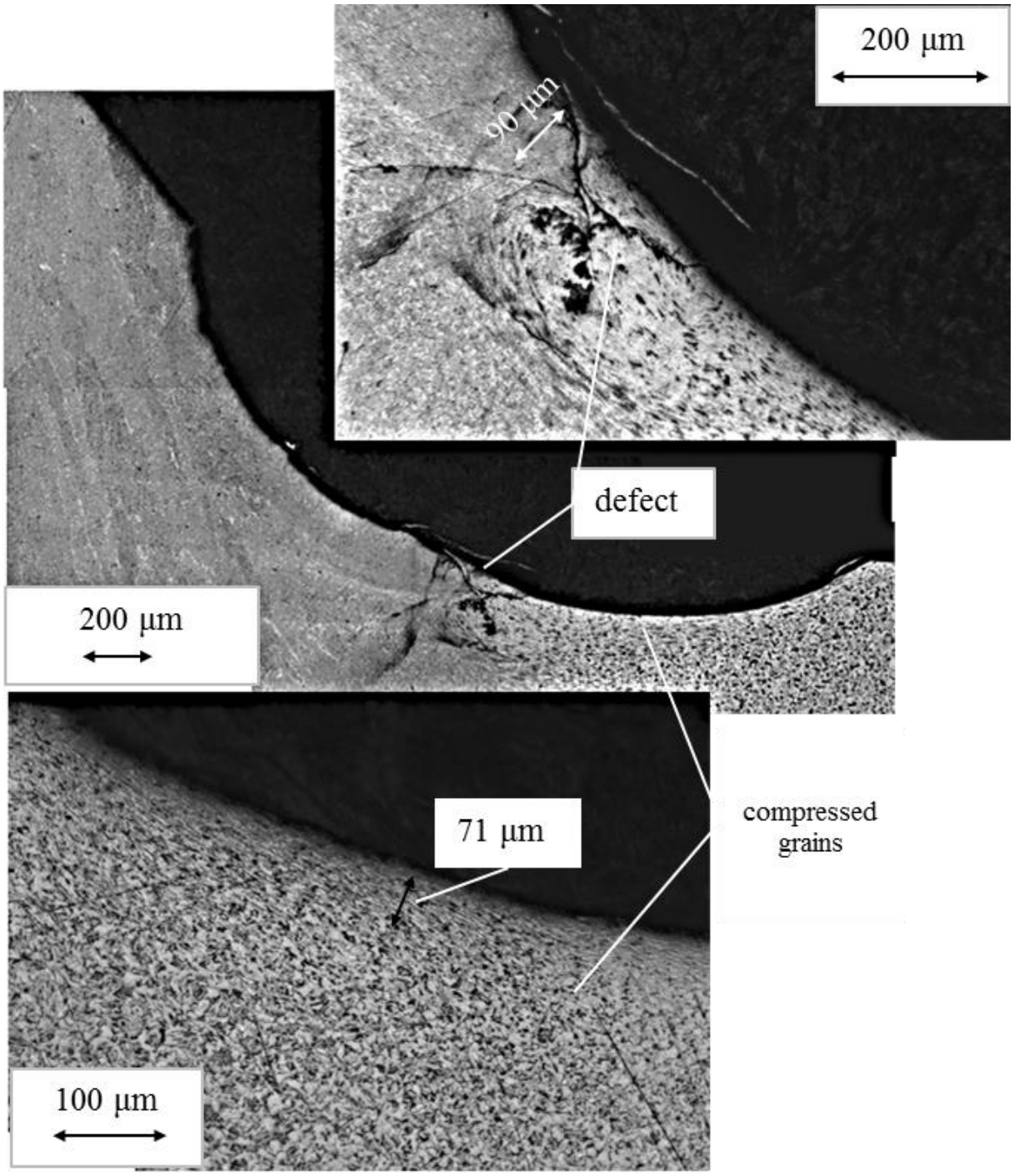

Figure 4.13**:** Microstructure of treated Type-L specimen

4.3.2 Microhardness Measurements

Hardness tests were then performed using a Vickers microhardness tester. Following the procedure in ASTM E384 [20], indentations were made to a depth of about 0.1 mm below the surface and then every 0.2 mm up to 2 mm in depth. The indent dimensions were measured using a microscope at X50 magnification. The Vickers hardness (HV) was then calculated for each depth using Equation 4.31:

Equation 4.31: $HV = 1854.4\frac{P}{d^2}$

where HV is the Vickers hardness number, P is the applied force in grams-force (here P = 200 gf), and d is the average diagonal length of the indentation in μm.

The microhardness measurements are summarized in Table 4.11 and Figure 4.14.

Table 4.11: Microhardness measurements (HV)

	As-welded			HFMI			Base metal
Depth (mm)	Loc.1	Loc.2	Average	Loc.1	Loc.2	Average	Loc.1
0.1	218	227	222.5	253	308	280.5	191
0.3	222	222	222.0	240	276	258.0	
0.5	219	212	215.5	239	269	254.0	195
0.7	219	195	207.0	230	256	243.0	
0.9	213	197	205.0	205	238	221.5	197
1.1	203	202	202.5	208	215	211.5	
1.3	202	200	201.0	207	207	207.0	193
1.5	209	205	207.0	206	211	208.5	
1.7	202	206	204.0	197	205	201.0	193
1.9	198	195	196.5	204	208	206.0	
2.1	198	199	198.5	208	198	203.0	191

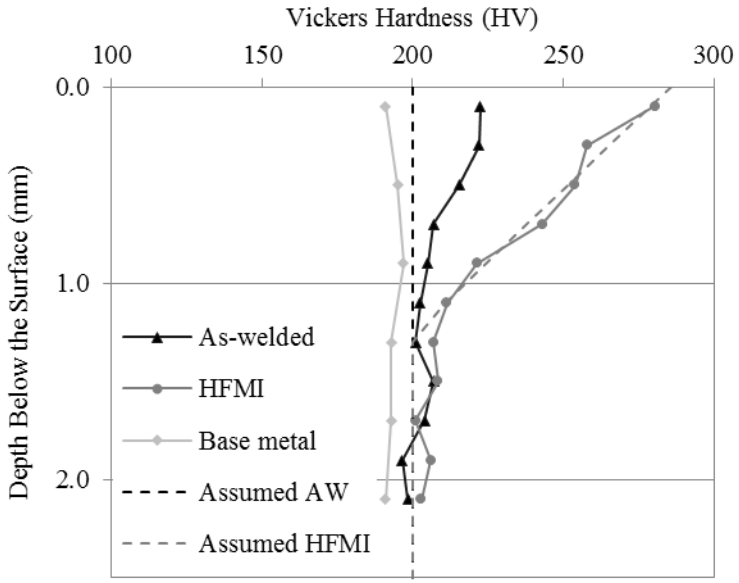

Figure 4.14: Microhardness measurements

As Figure 4.14 shows, using the HFMI treatment resulted in a considerable increase in the near-surface hardness. However, the hardness decreases rapidly below the surface, to that of the as-welded HAZ at a depth of ~1.0 mm. Similar general trends were reported in [4, 21].

4.4 Treated Weld Toe Geometry

A number of geometrical parameters describing the local conditions at the weld toe were measured using two different methods. These results were used as an input for the fracture mechanics analysis to calculate the stress concentration factors at the as-welded and impact treated weld toes.

The measured parameters are shown in Figure 4.15. The radius corresponding with the greatest indent depth on the base metal side was considered as the critical weld toe radius (R). Two indent depth measurements were taken for each weld toe. Indent depth was defined as the maximum perpendicular distance from a straight line to the bottom of the indent. One depth measurement (D_b) was taken with respect to a best fit line along the base metal surface, which is similar to the depth typically measured manually by weld inspectors for checking for undercuts when assessing weld quality. Another depth measurement (D_w) was taken with respect to a best fit line drawn along the surface of the weld. The average of the base metal and weld side indent depths (D_{avg}) was also calculated for each case. These parameters were measured using two non-destructive methods: silicon impression measurement and measurements obtained using a handheld 3D laser scanner.

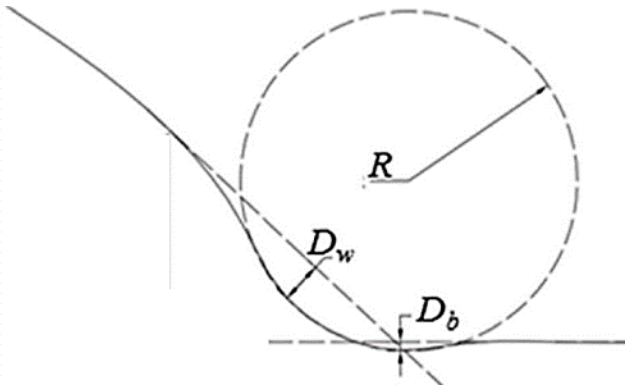

Figure 4.15: Weld toe geometry parameters

4.4.1 Silicon Impression Measurements

Weld toe parameters were measured by taking silicon impressions of the weld toe and then slicing them (Figure 4.16) in a similar way to the one described in [22]. A total of 12 measurements were conducted on four (two Type-X and two Type-L) weld toe impressions each at three locations (impression cuts). Measurements were also conducted on as-welded toe impressions to set a basis for conducting the treated weld toe impression measurements. The results are summarized in Table 4.12.

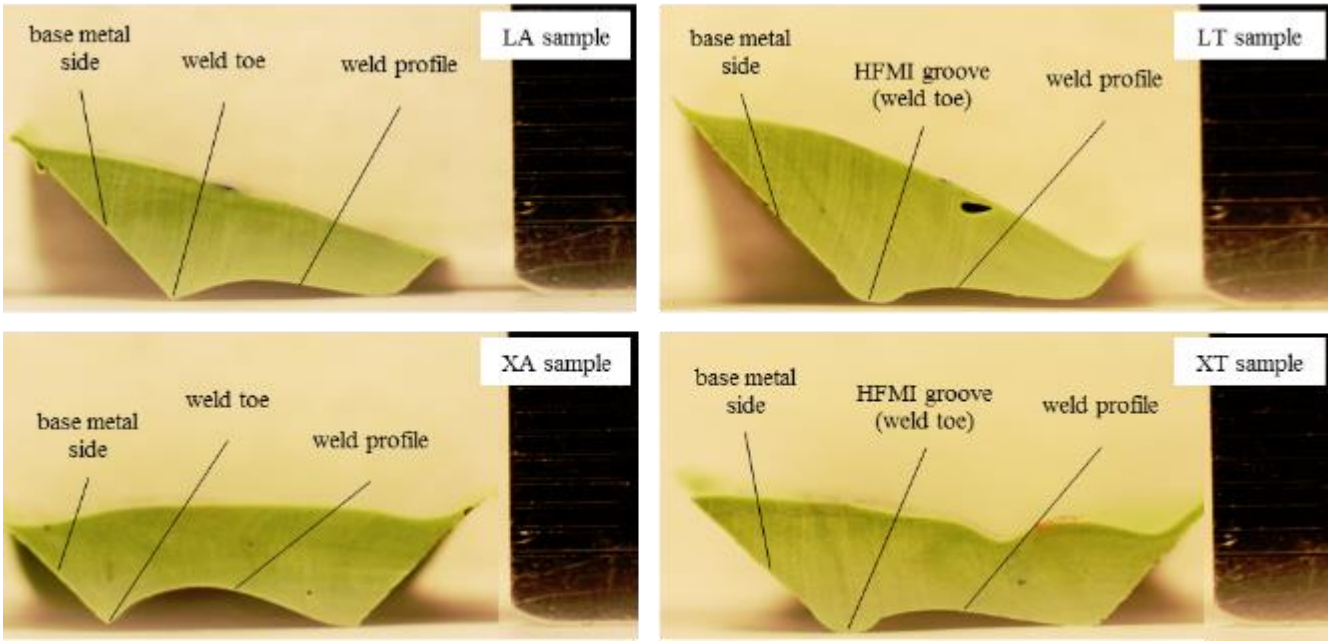

Figure 4.16: Silicon impression of weld toes

Table 4.12: Silicon impression-based measurements

Specimen	Cut	D_b (mm)	D_w (mm)	D_{avg} (mm)	R (mm)
LT1	1	0.066	0.336	0.201	1.68
	2	0.112	0.247	0.180	1.76
	3	0.032	0.329	0.181	1.81
LT2	1	0.082	0.206	0.144	1.74
	2	0.171	0.198	0.185	1.92
	3	0.270	0.273	0.272	1.87
XT1	1	0.143	0.353	0.248	1.76
	2	0.110	0.283	0.197	1.62
	3	0.203	0.361	0.282	1.68
XT2	1	0.184	0.272	0.228	1.94
	2	0.213	0.299	0.256	1.82
	3	0.258	0.275	0.267	1.94
Average:		0.154	0.286	0.220	1.80
Sample Standard Deviation:		0.076	0.053	0.045	0.11

4.4.2 Measurements Using 3D Handheld Laser Scanner

A recently developed methodology [23] to identify various impact treatment levels applied to a steel weld toe was also used to measure the weld toe geometrical parameters. This methodology has a number of advantages over the current quality assurance (QA) practices, which are mainly based on visual inspection. These advantages include providing quantitative measures for the treatment level, increasing ease of use, and providing the capability to document the weld toe profile before and after impact treatment for future referencing.

The geometrical properties of the weld toe were captured using an EXAscan™ handheld laser scanner. This scanner is designed for the rapid acquisition of a large number of points on the surface of an object. The device does not require an external positioning system as it uses two lines of laser light, three cameras, and small, circular, self-adhesive targets to record and register the specimen's geometry (Figure 4.17). One of the benefits of this external positioning system is that it does not require a high-skilled operator to achieve high accuracy results. The dynamic referencing mode (coordinate system) locks onto the object being scanned, thereby maintaining specimen alignment throughout the entire scanning process. Prior to the scanning process, an aerosol powder spray was applied to the specimens. This is a common method for reducing the reflectivity of scanning targets in order to increase the accuracy of the scan points. During the scanning process, a 3D surface geometry is acquired by

sweeping the laser scanner, and therefore the field of view of its three cameras, over the weld toe in a manner similar to spray painting (Figure 4.17). As the laser moves, it captures the surface geometry of the weld toe. The captured geometry is in the form of millions of individual data points consisting of x, y, and z coordinates in 3D space. This process is fast and provides a relatively high level of accuracy (0.04 to 0.05 mm) [24].

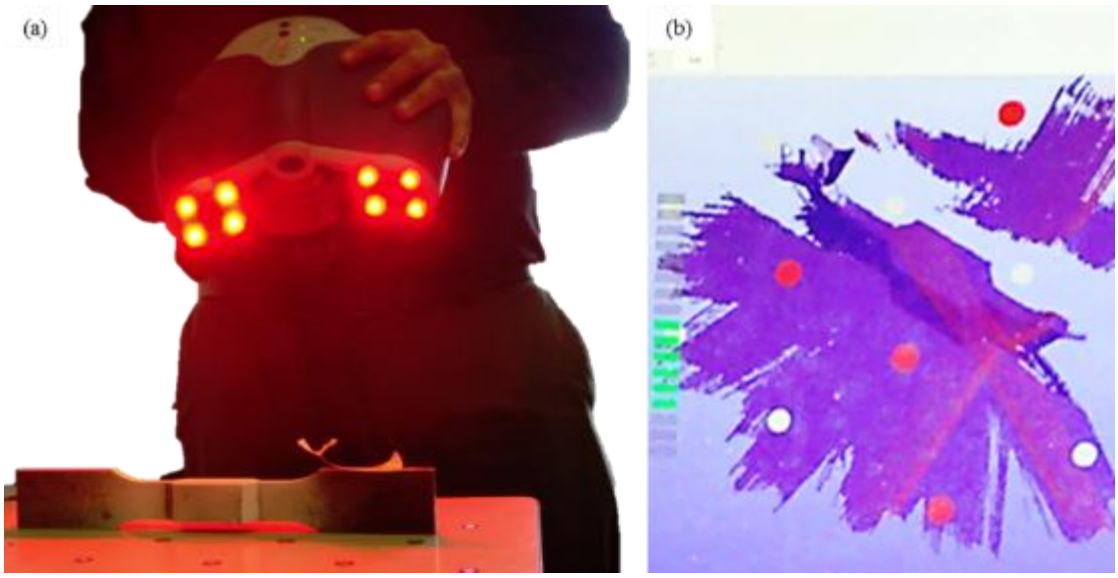

Figure 4.17: Scanning a weld specimen: (a) 3D laser scanner; (b) point cloud data

A suitable software package is then used to merge the point cloud data points collected into one 3D representation of the scanned object. Once the weld toe is scanned, the measured data can be easily extracted. Following the acquisition of the point cloud, a number of post-processing steps (described in [23]) were executed in order to obtain the desired weld toe profile information. The weld toe profile in the middle of the specimen was acquired by intersecting the 3D point cloud and the perpendicular middle plane. The geometric parameters were then measured using a computer-aided design (CAD) software (here AutoCAD) for the curves obtained in the previous step. The results are summarized in Figure 4.18 and Table 4.13.

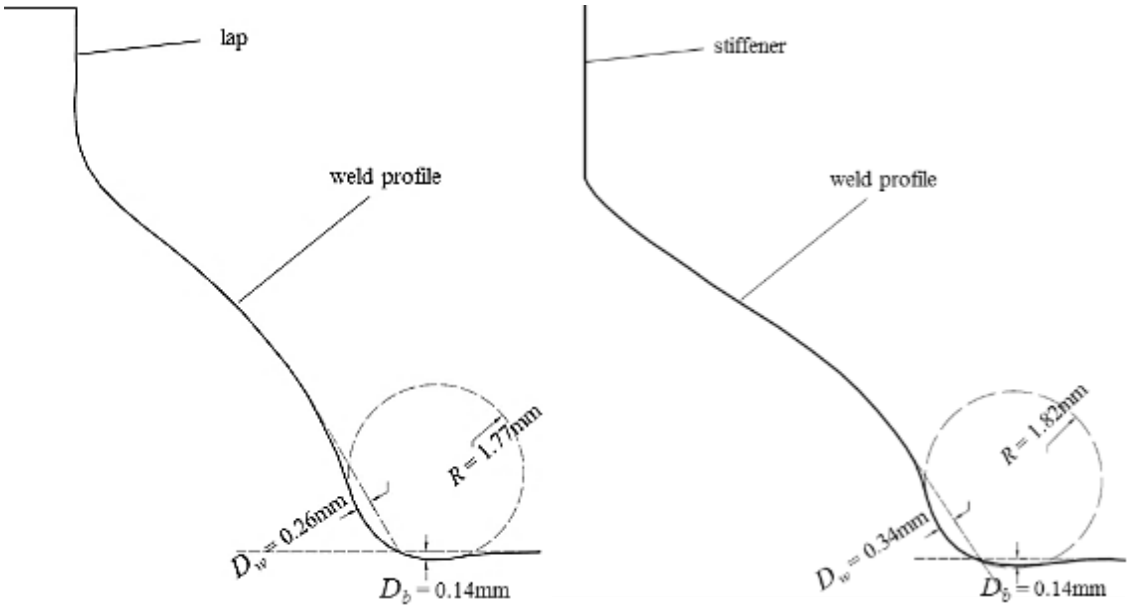

Figure 4.18: HFMI groove measurements for treated specimens

Table 4.13: Laser scanner-based measurements

Specimen	D_b (mm)	D_w (mm)	D_{avg} (mm)	R (mm)
LT3	0.14	0.26	0.20	1.77
XT3	0.14	0.34	0.24	1.82

4.5 Through-thickness Stress Distributions at the Weld Toe

The through thickness stress profiles for the as welded and treated specimens were determined by finite element (FE) analysis. The laser scanned weld toe profiles acquired in the previous section were inputted into an FE software package (*ABAQUS*) to generate the models (Figure 4.19). Linear elastic material behaviour with E = 208 GPa was assumed and the specimen geometry was modelled using 8-node biquadratic plane strain quadrilateral elements. The stress profile at the weld toe (defined as the deepest point of the groove for the treated specimens) caused by applying a remote unit stress was then determined. The results are summarized in Figure 4.20. As can be seen in this figure, the stress concentration reduction at the weld toe after applying the treatment was minimal.

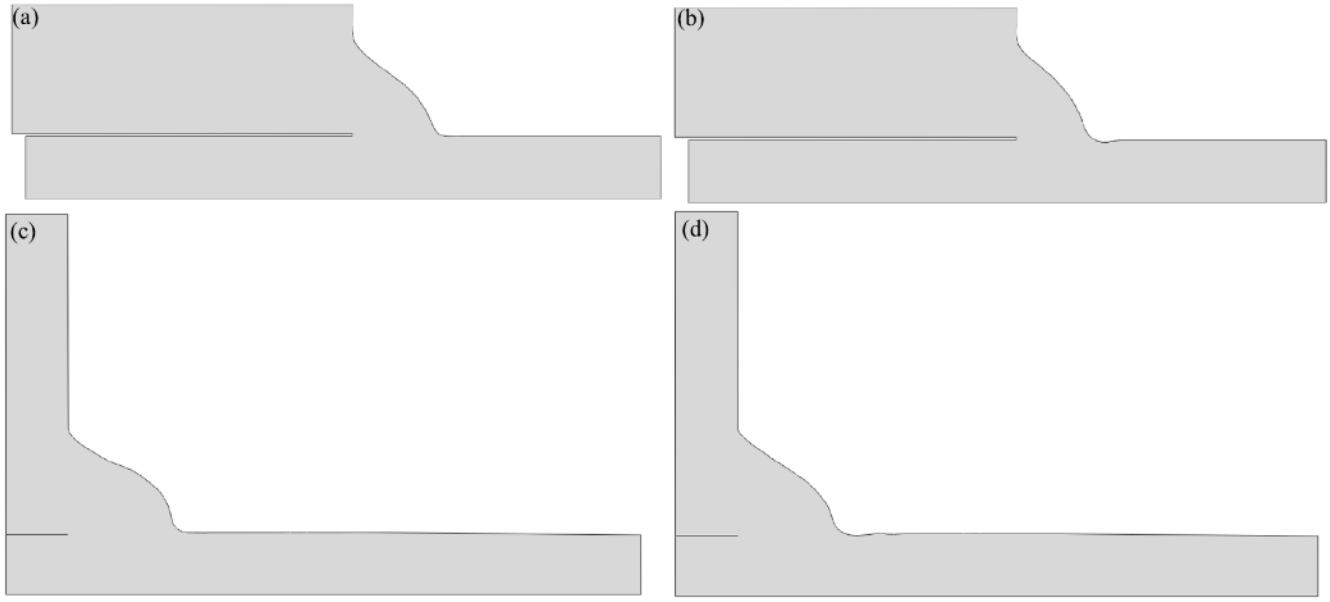

Figure 4.19: FE geometry models for specimens: (a): LA; (b): LT; (c): XA; (d) XT

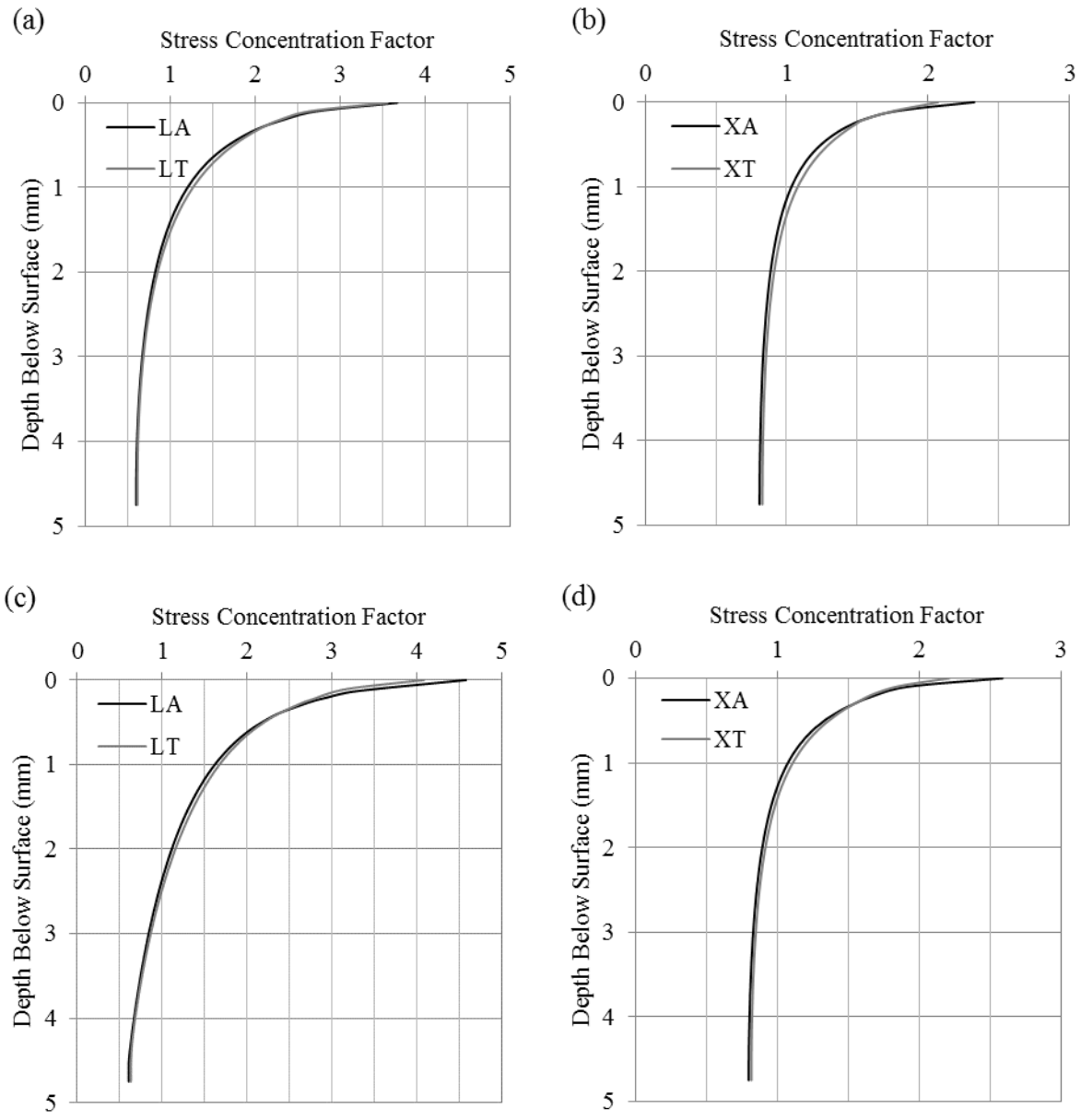

Figure 4.20: Through thickness axial stress profiles at weld toe: (a) and (c) axial stress; (b) and (d) maximum principal stress

4.6 Residual Stresses

The residual stress state at the weld toe plays a key role in the fatigue performance of the as-welded and HFMI treated welded joints. In order to precisely evaluate the residual stress profile induced by the peening treatments, a finite element (FE) analysis was undertaken and the effects of different parameters on the resultant stress state due to peening at the toe were studied. Direct residual stress measurements were also conducted and the final residual stress profile at the treated weld toe, to input into the fracture mechanics model, was determined by considering both the FE and measured distributions.

4.6.1 Finite Element Analysis of Bridge Welds Retrofitted by Peening

Two-dimensional finite element (FE) models that simulate the treatment process were used to model the treatment of the Type-X fatigue specimens. Effects of the plate thickness, indentation depth, and preload level on the residual stress distribution induced by peening under load were then studied. A more complete version of this analysis is presented in [25].

For this study, needle peening was modelled by a 2D static analysis of a single indentation using the FEA program ABAQUS. The FE model consisted of a 2D solid indenter impacting the weld toe of a 2D plane strain model of a transverse stiffener. In this model, a 2.5 mm diameter elastic steel (E = 200 GPa) hemispherical indenter impacted the elastic-plastic base material at the weld toe, imposing a predefined indentation depth. In modelling the base material, yield and ultimate stress levels were chosen based on the measured values obtained from the materials tests reported in [4].

Each analysis is done in three steps: the preloading step, the indenting step, and the unloading step. In the preloading step, the predefined preload (if applicable) is applied. Preloading was modelled by prestressing the base material and maintaining the same load level throughout indentation and unloading steps. In the indenting step, the static indenter impacts the weld toe region and penetrates into the base material up to a predetermined indentation depth. Finally, the static indenter returns to its original position during the unloading steps. These steps are shown in Figure 4.21.

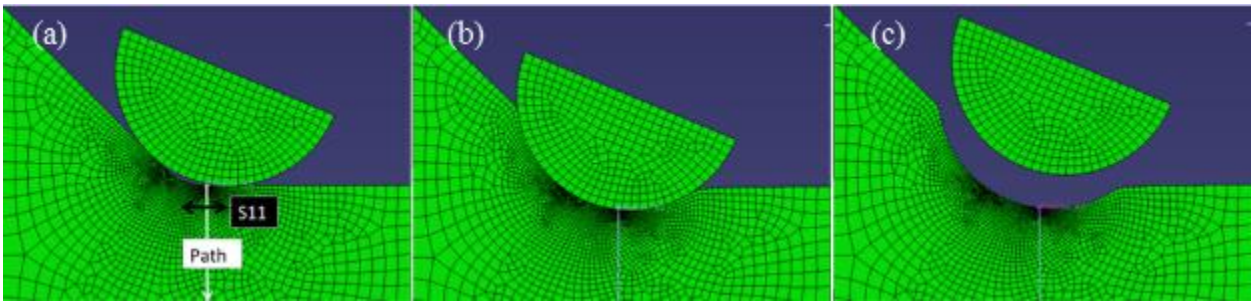

Figure 4.21: Analysis steps: (a) preloading; (b) indenting; (c) unloading

After unloading (i.e. removing the indenter), the residual stress distribution in the direction of the applied load (S11) through the thickness of the plate at the weld toe ("path" in Figure 4.21) is graphed against the depth below the surface.

The model geometry and boundary conditions are presented in Figure 4.22. The weld toe geometry was modelled based on the 35 angle and radius measurements reported in [26]. A typical weld toe with weld toe angle and radius of 45° and 0.6 mm, respectively, is used in all models. In the current study, the effects of preload level and plate thickness are also investigated

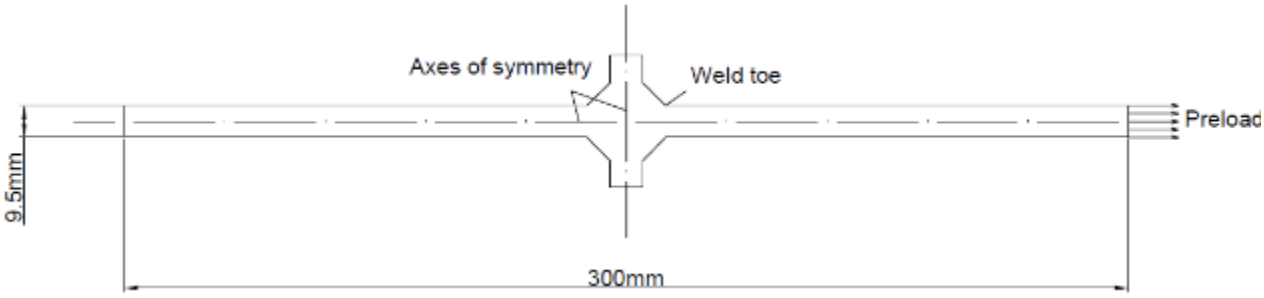

Figure 4.22: Model geometry and boundary conditions

Figure 4.23 represents a typical stress pattern through the thickness of the plate at weld toe region. In this figure, red represents the tension and blue means compression.

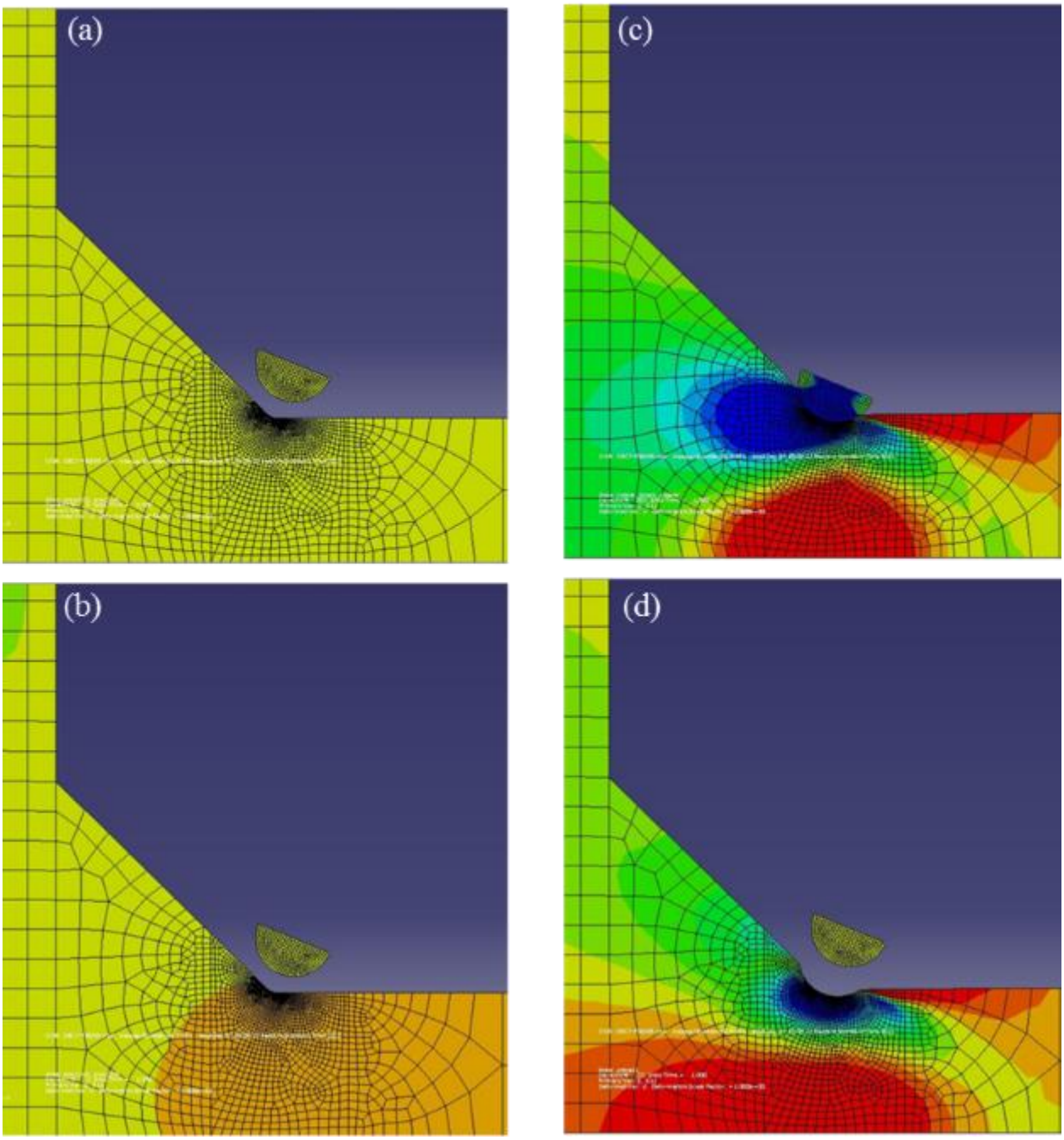

Figure 4.23: Stress pattern through the thickness of the plate at weld toe region: (a) at rest; (b) after preloading step; (c) after loading step and before unloading step; (d) after unloading step

The magnitude and subsurface distribution of the residual stresses induced by peening at the weld toe of the tested fatigue specimens was measured using X-ray diffraction techniques for two normally peened (not preloaded) fatigue specimens, as discussed in [26]. The results of these measurements were used to validate the static indenter model use in this FE study. An envelope of the residual stress measurements

is presented in Figure 4.24, along with analysis results for the FE model with various indentation depths assumed from 0.05 to 0.3 mm. The specimen naming scheme format in Figure 4.24 and Figure 4.25 is FS-P#-I#, where FS stands for "Fatigue Specimen", P# represents the prestress level in MPa (e.g. P45 represent a 45MPa prestress level), and I# represents the indentation depth in 10-2 mm (e.g. I05 means an indentation depth of 0.05 mm).

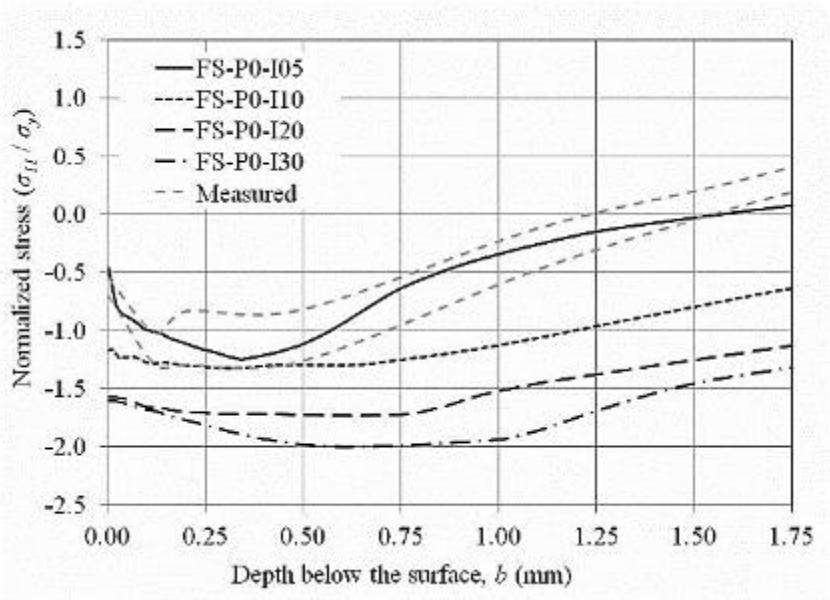

Figure 4.24: Residual stress profiles for fatigue specimen.

As Figure 4.24 indicates, the analysis results for a static indentation depth (d) of 0.05 mm fell between upper and lower bounds of the residual stress measurements. Moreover, d = 0.05 mm also predicts the compressive residual stress zone depth (~1.5 mm) reasonably well. On the other hand, results for d = 0.1 mm accurately estimate the value and location for the largest (in magnitude) compressive residual stress. Thus it can be concluded that a suitable value for an effective static indentation depth that results in good predictions of the measured residual stress distribution will lie somewhere between 0.05 mm and 0.1 mm.

Figure 4.25 presents results for the analysis of the fatigue specimen under the various investigated prestressing levels for two static indentation depths. Looking at this figure, it can be seen that the peak compressive residual stress level is not significantly affected by the 45 MPa prestress. In the case of the 165 MPa prestress, a reduction in this peak compressive residual stress level is seen. However, in both cases, this stress level still exceeds the yield strength of the material. In general, the peak compressive

residual stress level was seen to be less sensitive to the prestressing level when the indentation depth is increased to 0.3 mm.

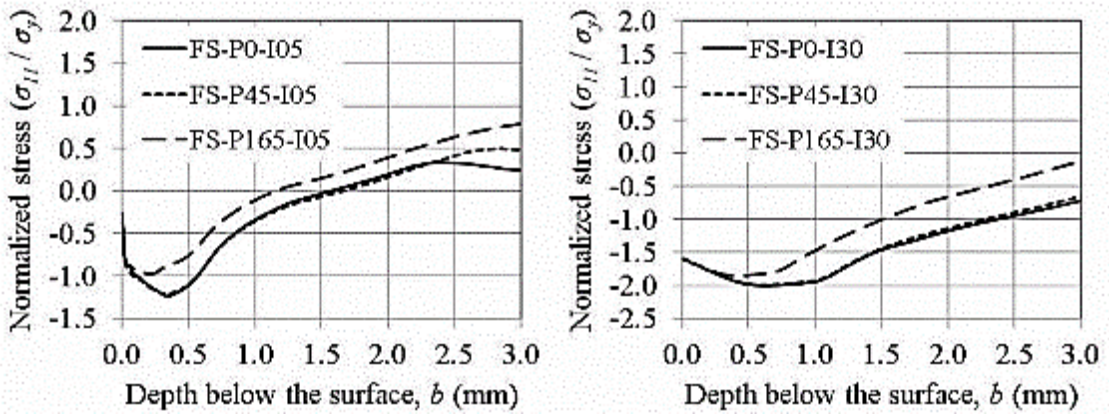

Figure 4.25: Effect of prestress on residual stress profile for FS model.

Based on the results presented in this sections, the following conclusions were drawn:

- Mainly depending on the indentation depth, the impact treatments can result in a compressive residual stress field near the surface at the weld toe with a peak magnitude of as high as two times of the material's yield strength.
- Subsurface self-equilibrating tensile residual stresses were also generated by applying the impact treatment.
- The treatment-induced residual stress profiles were similar to each other at different preload levels when the indentation depth is ~0.3 mm.
- The peak compressive residual stress level and compressive residual stress zone depth increased with an increase in the indentation depth.

4.6.2 Residual Stress Measurements

Residual stress measurements were conducted using the X-ray diffraction method. This method was chosen because it had an appropriate spatial and volumetric resolution to adequately characterize the residual stress distributions.

The residual stress measurements were performed on two randomly-chosen untested specimens, one as-welded and one impact (HFMI) treated, at different locations. Thirteen measurements were taken at four locations on the treated specimen at the surface and depths of approximately 0.1, 0.3, 0.6 and 1.0 mm

below the surface. For the as-welded specimens, five measurements were taken at two locations at the surface and depths of approximately 0.1, and 0.3 mm below the surface. Measurements were made using the Laboratory X-Ray Diffraction (LXRD) system at Proto Manufacturing Ltd., following the procedure recommended in ASTM- E915 [27]. Each measurement location was first electro-polished to the desired depth, the measurement was made, and the location was then polished further to reach to the next desired depth. Figure 4.26 shows a specimen in the LXRD system.

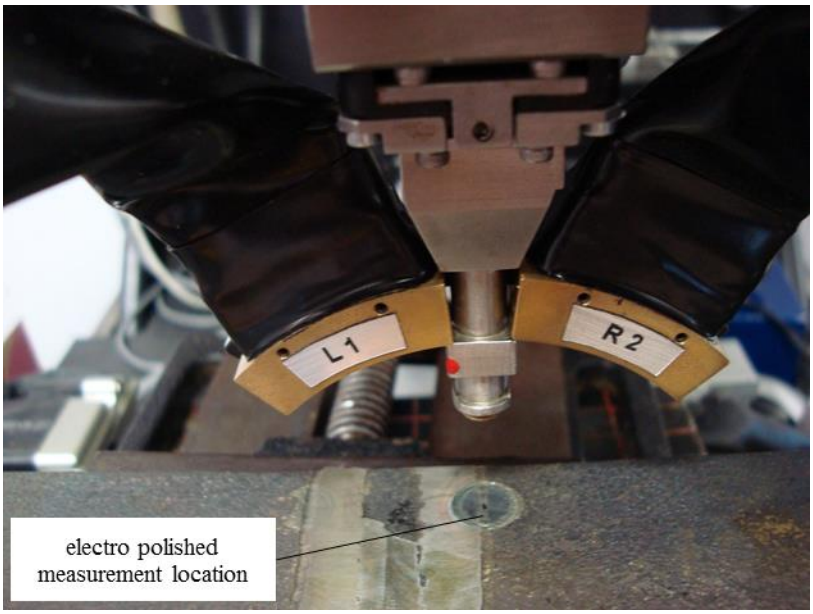

Figure 4.26: LXRD system for residual stress measurements

Measured residual stresses for all the samples are summarized in Table 4.14 and Figure 4.27.

Table 4.14: Residual stress measurements (MPa)

	Depth (mm)	Location 1	Location 2	Location 3	Location 4
HFMI treated Specimen	0.00	-44 ± 10	-238 ± 15	-509 ± 26	-112 ± 16
	0.10	-124 ± 12	-92 ± 7	-203 ± 7	
	0.12				-176 ± 8
	0.31	-4 ± 6		-145 ± 10	-360 ± 8
	0.64				-132 ± 8
	1.02				-40 ± 13
As-welded Specimen	0.00	-9 ± 42	-82 ± 21		
	0.13	86 ± 17	-57 ± 9		
	0.33		-12 ± 46		

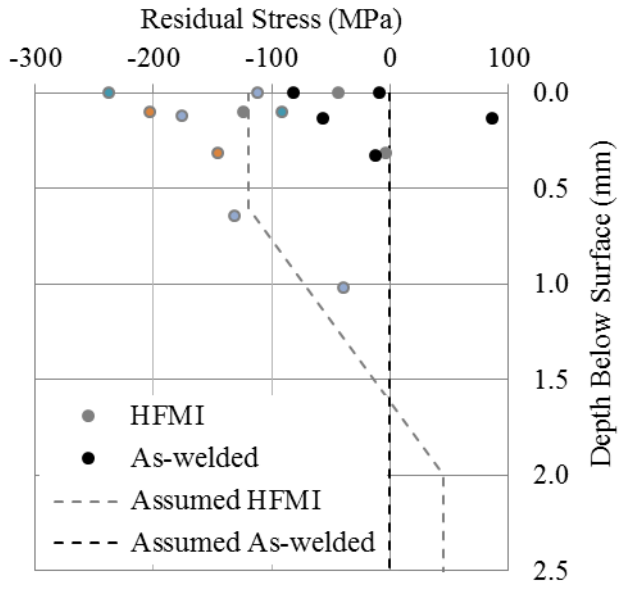

Figure 4.27: Residual stress measurements

A very large scatter was observed in the residual stress measurements. The measurements previously reported in [22, 26] showed that there was an approximately uniformly distributed tensile residual stress in the top few millimetres below the surfaces with a magnitude of 15~20 % of yield stress for the untreated specimen. The current measurements, however, showed considerable scatter and no clear trend with a range of -82 to 86 MPa, with results scattered around an mean of ~zero MPa.

Impact treatment of the specimen resulted in a significant change in the residual stress distribution through the specimen thickness with a high magnitude compressive stress near the weld toe surface. It then gradually decreases for about a millimeter below the surface. A self-equilibrating distribution for the compressive residual stress in the treated specimens was assumed in the SBFM analysis based on the general trends observed in the previous measurements reported in [22, 26]. This distribution (with a peak compressive stress of $0.33 \cdot f_y$ near the surface) is also plotted in Figure 4.27.

4.7 Conclusions

Several input parameters for the fracture mechanics model (discussed in the next chapter) were determined using a comprehensive materials testing plan, FE analysis, 3D laser scanning, and direct measurements. A recently developed experimental technique to derive the crack closure parameters and the effective crack growth curve by using smooth specimens was used. The results were then validated by conducting a series of fatigue crack growth tests on compact-tension (CT) specimens. The effect of

impact treatment on the near-surface hardness of the fatigue specimens was investigated by conducting microhardness tests on the heat affected zone (HAZ) of the as-welded and treated specimens. Microstructure pictures were also taken to obtain a better understanding of the microstructure of a treated weld. The as-welded and treated weld toe geometries were determined using silicon impressions and also a 3D laser scanner. The FE method was then used to determine the stress concentration factors at the weld toes. The FE method was also used to evaluate the residual stress profile induced by the peening treatments and the results were compared with the X-ray diffraction -based residual stress measurements conducted on the as-welded and treated specimens.

Chapter 5

Strain-Based Fracture Mechanics Analysis

5.1 Introduction

Various analytical approaches are used to predict the fatigue performance of welded structures and also the beneficial effects of residual stress-based post-weld treatments. In most codes and recommendations, a variations of the "detail category" or an "*S*-*N* curve" approach are employed. Neither the Classification method nor the structural stress approach give precise information about crack size and crack growth in different stages of the structure's service life. Fatigue test results have shown that there are other parameters, e.g. loading scheme, influencing the fatigue behaviour of structures other than the design stress range and the detail geometry. Moreover, there are a number of fatigue rehabilitation methods that enhance the fatigue behaviour of the structures and the effect of these methods can only be fully understood by using analytical models that can account for all of these variables. Linear elastic fracture mechanics (LEFM) is such an analytical tool, with the ability to predict the behaviour of propagating cracks in structures. Conventional fracture mechanics deals only with the crack growth in materials by calculating a crack driving force and characterizing the material's resistance to fracture. Basic assumptions in linear elastic fracture mechanics are that the material is isotropic and linear elastic. The stress field near the crack tip is then calculated using the theory of elasticity. In LEFM, most formulas are derived for either plane stress or plane strain conditions, associated with the three basic modes of loading on a cracked body: opening, sliding, and tearing. LEFM is valid only when the inelastic deformation is small compared to the size of the crack, or under a condition commonly referred to as small-scale yielding. If large zones of plastic deformation develop in the vicinity of the crack, other methods such as elastic plastic fracture mechanics (EPFM) or strain-based fracture mechanics (SBFM) must be used.

A strain-based fracture mechanics (SBFM) approach, which is similar to LEFM in many ways, can be used to account for non-linear material behaviour, which may be significant at the weld toe under high applied stress ranges. Thus, SBFM is suitable for considering the effects of the large overloads and underloads that may occur under in-service loading histories typical of bridge structures. The development and use of a SBFM model is described in this chapter. This SBFM model [1] is able to predict two crack growth accelerating mechanisms, which can be particularly severe for impact treated

welds. These mechanisms include 1) relaxation of the compressive treatment stresses due to compressive under-loads that are large enough to cause a nonlinear material response, and 2) reducing the crack opening stress level due to large compressive under-loads or tensile over-loads that results in increasing the effective (damaging) portion of the applied stress cycle, for a number of cycles following the extreme loading event. Additionally, the SBFM model does not require two stages to model the total fatigue life of the weld. The model is developed to model small crack behaviour in notches, where material behaviour is nonlinear, and it does not run into the problems of LEFM in this domain. For larger crack sizes, the results converge on those predicted by LEFM. Based on previous studies and metallurgical analysis, it is thought to be a reasonable assumption that very small defects are present at welds prior to loading [1].

The strain-based fracture mechanics (SBFM) model is validated using the fatigue test results presented and discussed in the previous chapters. This model is chosen because of its ability to model both high-cycle and low-cycle fatigue problems. Rare and severe overload events can occur in the long life regime and the SBFM model is particularly well suited for modelling treated welds as it keeps track of the residual stresses following these severe overload events.

5.2 Strain-based Fracture Mechanics (SBFM) Model

A strain-based fracture mechanics (SBFM) model is used to analyze the fatigue specimens. An earlier version of this model was successfully used in [1] to analyze treated welds under variable amplitude (VA) loading conditions. The model's ability to predict the fatigue performance under different loading and treatment conditions typical for highway bridge applications was evaluated by comparing the predicted results with the test results on small-scale weld specimens in [1-3]. In this study, several changes were made to make the SBFM model compatible with the effective strain-life model described in Chapter 4.

5.2.1 Model Description

The model used in this research is basically a linear elastic fracture mechanics (LEFM) model that is modified to consider non-linear material effects. By applying the effective crack growth relationship derived in the previous chapter, the number of cycles to failure, N, is calculated by numerically integrating the following expression over a crack depth range, a_i to a_c (initial to critical crack depth).

Equation 5.1: $\frac{da}{dN} = C(\Delta K_{eff} - \Delta K_i)^m$

where a is crack depth, C and m are material constants, and ΔK_{eff} and ΔK_i are the effective and intrinsic stress intensity factor ranges, respectively.

Crack closure effects are considered in the calculation of ΔK_{eff} by using the following expression

Equation 5.2: $\Delta K_{eff} = K_{max} - MAX\left(K_{op} - K_{min}\right)$

where K_{max} and K_{min} represent the stress intensity factors (SIF) at the maximum and minimum load levels in each load cycle, respectively, and K_{op} is the SIF corresponding to the crack opening stress level in that load cycle.

Each SIF is determined using the following expression:

Equation 5.3: $K = YE\varepsilon\sqrt{\pi a}$

where Y is a correction factor that accounts for the crack shape, the finite thickness of the plate, and the free surface on one side of the crack, E is the modulus of elasticity of the material, a is the (crack) depth below the surface, and ε is the local strain at that depth.

A cyclic Ramberg-Osgood material model is used to determine the stresses and strains for each load cycle:

Equation 5.4: $\Delta\varepsilon = \frac{\Delta\sigma}{E} + 2\left(\frac{\Delta\sigma}{2K'}\right)^{1/n'}$

where $\Delta\varepsilon$ and $\Delta\sigma$ are the changes in the strain and stress, respectively, and K' and n' are material constants.

Neuber's rule is used to calculate strain histories at various depths below the surface of the weld toe.

Equation 5.5: $\Delta\varepsilon \cdot \Delta\sigma = \frac{(k\Delta S)^2}{E}$

where k is the (theoretical) stress concentration factor and ΔS is the nominal applied stress range

A formula proposed in [4] is used to model the steady state crack opening stresses:

Equation 5.6: $$S_{opss} = \theta S_{max}\left(1-\left(\frac{S_{max}}{\sigma_y}\right)^2\right)+\varphi S_{min}$$

where S_{opss} is the steady state crack opening under constant amplitude (CA) loading, S_{max} and S_{min} are the nominal maximum and minimum stresses in a smooth specimen (or the local maximum and minimum stresses at the notch root in a notched specimen, respectively), σ_y is the cyclic yield stress, and θ and φ are two experimentally determined material constants.

Along with this crack closure model, a model proposed in [5] is used which relates the change in the crack opening stress in a given cycle (ΔS_{op}) to the difference between the current opening stress (S_{cu}) and the steady state crack opening stress (S_{opss}):

Equation 5.7: $$\Delta S_{op} = \mu\left(S_{opss} - S_{cu}\right)$$

where μ is a material constant.

During the analysis, the material is cyclically loaded at various depths below the surface of the weld toe and the strain parameters are determined for each load cycle. As shown in Figure 5.1, the local elastic stress (σ_{el}) is calculated by adding up the local elastic residual stress ($\sigma_{el,res}$) due to welding (and HFMI treatment in the case of the treated specimens) and the local elastic stress due to the applied load ($\sigma_{el,app}$).

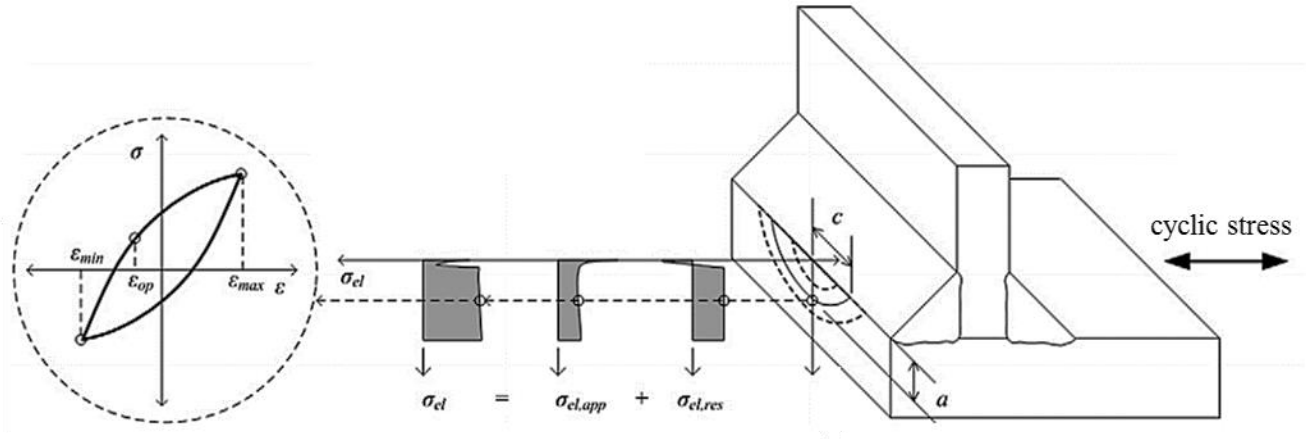

Figure 5.1: Stress-strain analysis according to SBFM model [1]

Using the approach described in [6], a stress concentration factor, k_p, that considers the presence of the crack in the weld toe, is used to determine the local elastic stresses. The following expression is used to calculate k_p

Equation 5.8: $k_p = \frac{K_{el}}{Y\sqrt{\pi a}}$

where k_p is the modified stress concentration factor (SCF), k_{el} is the SCF for the uncracked weld toe, and K_{el} is the elastic stress intensity factor that considers the non-uniform stress distribution along the crack path.

To calculate K_{el}, elastic weight functions, $m(x, a)$, from [7] for edge cracks in a semi-infinite plate are used in Equation 5.. The effects of crack shape and finite plate thickness are considered by using the proper correction factors in the calculation of the SIF (Y factor in Equation 5.3).

Equation 5.9: $K_{el} = \int_0^a k(x)\, m(x,a)\, dx$

In this equation, x is the depth below the surface of the plate.

The local elastic stress (σ_{el}) corresponding with S can then be calculated using Equation 5.10:

Equation 5.10: $\sigma_{el} = k_p \cdot S$

The stress-strain hysteresis loops are generated by calculating the local nonlinear stress-strain history for the given nominal stress history. Each time a hysteresis loop is closed, σ_{max}, ε_{max}, σ_{min}, ε_{min}, σ_{op}, and ε_{op} are calculated. Using these parameters, ΔK_{eff} and da/dN are then determined. Finally, the fatigue life is calculated by a numerical integration of Equation 5.1.

The model requires the residual stress distributions for the fatigue detail due to both welding and the applied post-weld treatment method (if applicable). As a simplification, the residual stresses are introduced by shifting the initial stress monotonically from zero to the specified residual stress level. The effect of any strain hardening due to the treatment is conservatively ignored in this method.

5.2.2 Input Parameters

The described SBFM model requires a number of input parameters, which can be determined by materials testing, finite element analysis, and experimental observations. The required material constants were determined in the previous chapter and are summarized in Table 5.1. Finite element (FE) analysis was used to determine the stress concentration factors. A number of geometrical parameters concerning the crack size and shape were determined based on the experimental observations and the literature in this field. The residual stress measurements conducted by using the X-ray diffraction method in conjunction with the FE analysis described in the previous chapter were used to determine the residual stress distributions due to the HFMI treatment and the welding process.

Table 5.1: Input parameters for the SBFM model

Parameter	Value	Unit	Source
E	208,083	MPa	monotonic and cyclic material testing
S_y	356	MPa	
σ_y	410	MPa	
K'	812	MPa	cyclic material testing and hardness measurements
n'	0.108	-	
local K'	$1.45 \cdot 3.45 \cdot HV^*$	MPa	[8]
local n'	0.15	-	
C	$1.1 \cdot 10^{-10}$	MPa, mm	effective crack growth measurements
m	2.01	-	
ΔK_i	80	MPa·√mm	
θ	0.448	-	effective strain-life model
φ	0.024	-	
μ	0.018	-	
a_i	0.15	mm	[1, 9], microstructure imaging

*HV: Vicker's hardness number

Stress concentration factor (k_{el}) and k_p: finite element (FE)-based stress concentration factors (SCF) for the as-welded weld toe profiles, presented in the previous chapter, were used to calculate k_p.

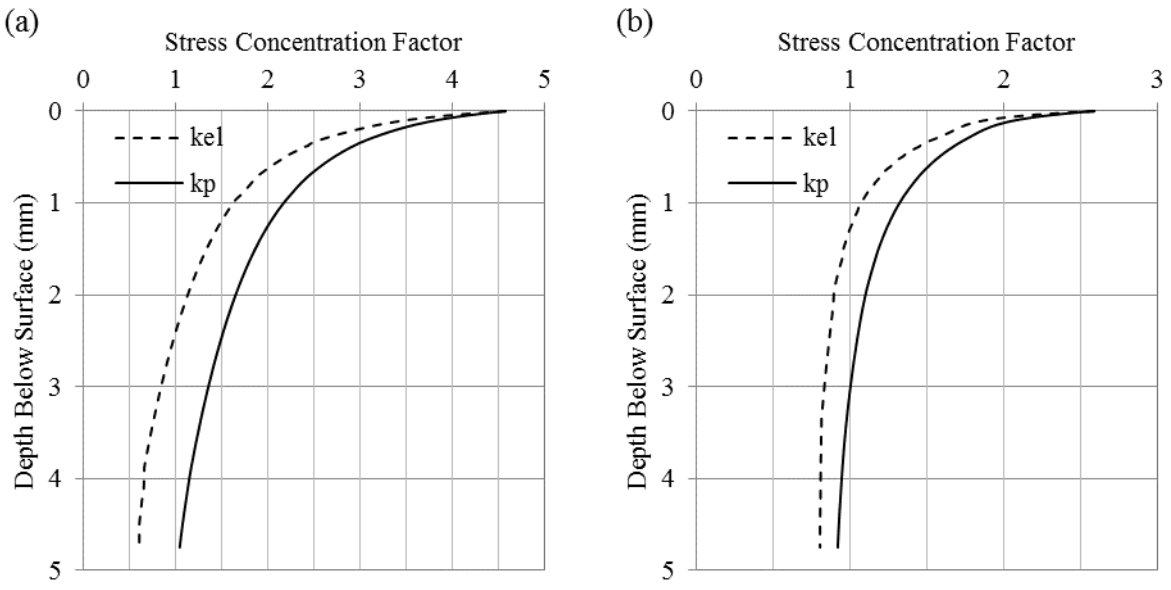

Figure 5.2: SCF distributions: (a) Type-L specimen; (b) Type-X specimen

Initial crack size: an initial crack size of 0.15 mm is assumed according to the previous studies at the University of Waterloo [1, 3] and the microstructure imaging reported in the previous chapter.

Critical crack size: the critical crack size was calculated based on the average stress over the remaining (net) cross section exceeding the tensile strength, and not larger than one half of the thickness (4.75 mm).

Crack shape: based on the observed cracks and similar to [1, 3], a through crack is assumed. An initial crack aspect ratio (a/c where c is half of the width of the semi-elliptical surface crack) of 0.6 was assumed. This ratio was assumed to linearly vary to zero at a crack depth of 1.0 mm.

Compressive residual stresses due to HFMI treatment: as described in the previous chapter, a self-equilibrating residual stress distribution was assumed. Elastic weight functions, $m(x, a)$, from [7] were also used to calculate the SIF for the treated specimens.

Tensile residual stresses due to welding: a uniform zero residual stress was assumed for the as-welded specimens.

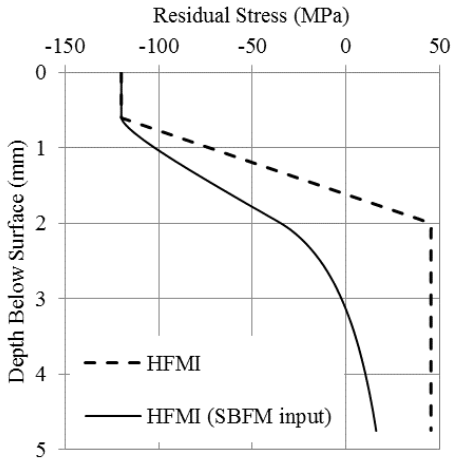

Figure 5.3: Residual stress distribution for treated specimens

5.3 Comparison of Model Predictions and Test Results

The model predictions for the fatigue experiments are presented in this section and are compared with test results that were presented in Chapter 3.

5.3.1 Constant Amplitude (CA) Loading

The SBFM predictions and test results for the as-welded and treated specimens tested under CA loading are presented in Figure 5.4. Distinctly different *S-N* slopes were predicted by the model for the as-welded and the treated weld toes in both cases. For comparison, a number of additional CA (with R = 0.1) test results for Type-X specimens are also included in this figure. These additional test results were reported in [1, 3] using a similar specimen geometry to the Type-X specimen.

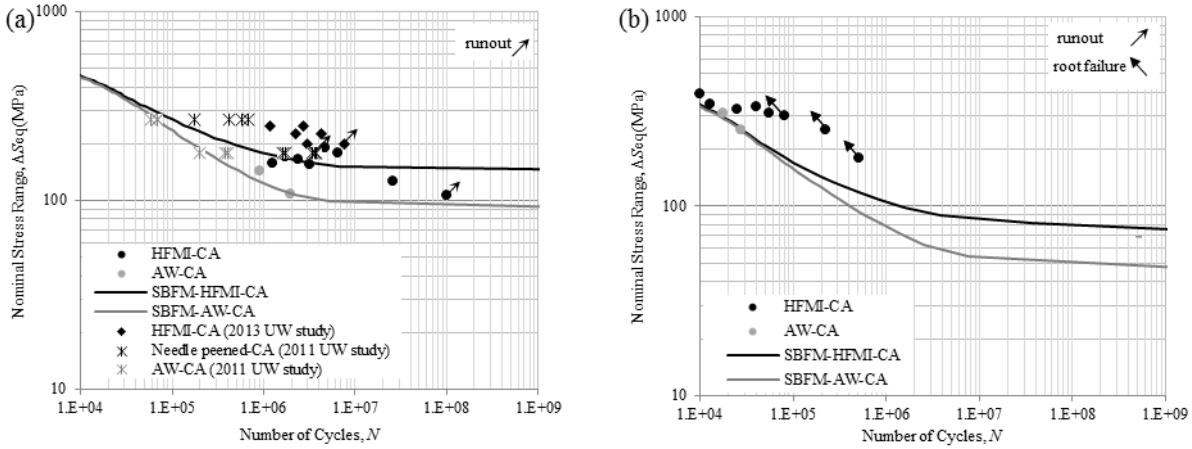

Figure 5.4: SBFM predictions for CA test results

As Figure 5.4 suggests, the SBFM model closely predicted the fatigue behaviour of the as-welded and the treated Type-X specimens. Close fatigue life predictions were also obtained for the as-welded Type-L specimens. The fact that no fatigue improvement due to the HFMI treatment was obtained at high stress levels (300 MPa and higher) was also correctly predicted by the model. At lower stress ranges for the Type-L specimen, however, the test results showed some degrees of fatigue life improvement in the form of changing the mode of failure from the toe to the root. These observations were conservatively underpredicted by the SBFM model. Finally, in both of the cases, the SBFM results predict an almost 80% increase in the constant amplitude fatigue limit (CAFL) due to the application of HFMI treatment.

5.3.2 Effect of Variable Amplitude Loading History

Figure 5.5 and Figure 5.6 present the SBFM model predictions for the variable amplitude (VA) fatigue tests. The equivalent stresses for the VA tests are calculated based on $m = 3$ in these figures. As the figures imply, the VA loading effects on the fatigue lives of the specimens are closely predicted for the as-welded specimens in both cases. For the treated specimens, the fatigue lives for both test types are underpredicted to some extent in the long life regime. However, several important trends are predicted by the model including the early toe failures for the severely overloaded specimens and the lower fatigue limit under VA loading histories compared to the CA loading history.

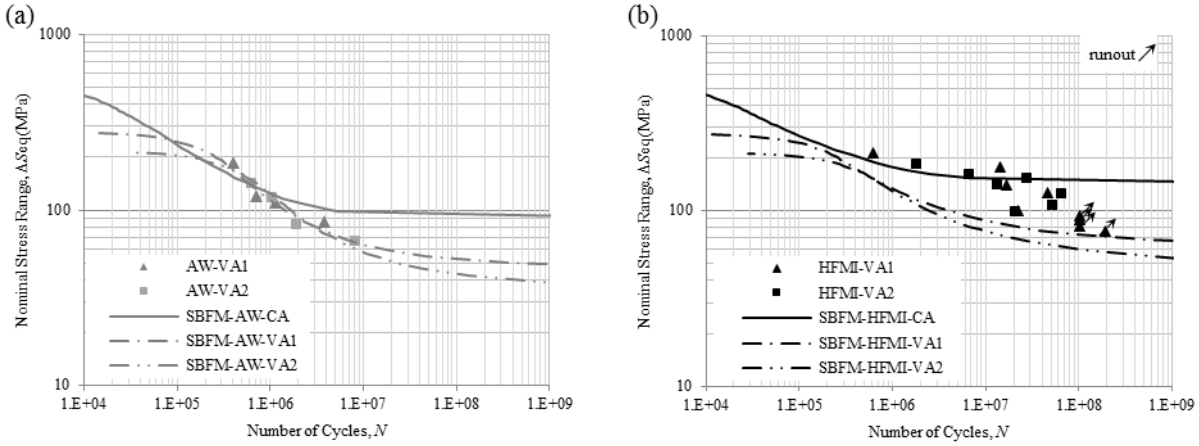

Figure 5.5: SBFM predictions for Type-X specimens: (a) as-welded; (b) treated

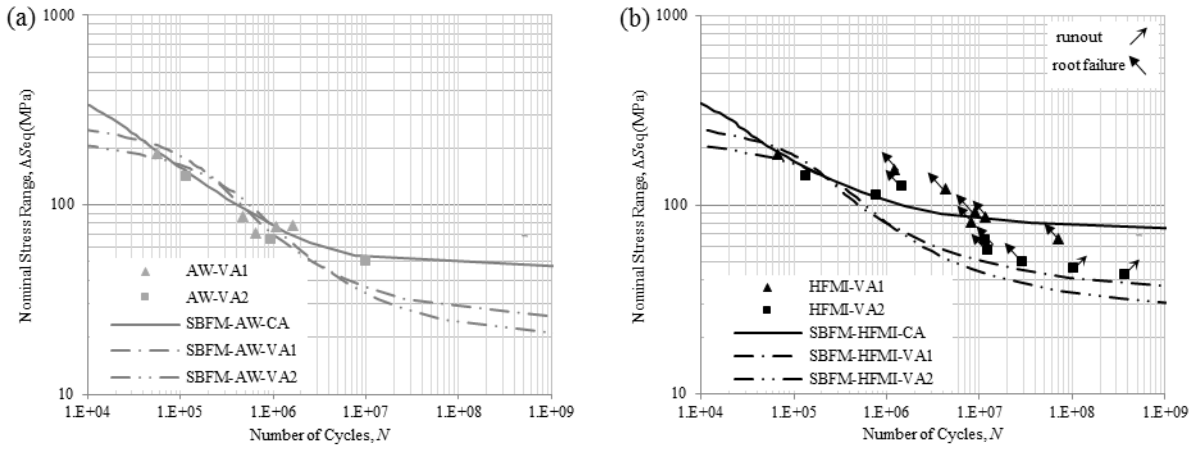

Figure 5.6: SBFM predictions for Type-L specimens: (a) as-welded; (b) treated

5.3.3 Re-visiting the Web Stiffener Specimens (Distortion-induced Fatigue)

Fillet welded joints can be divided into two main groups: details with load carrying fillet welds and details with non-load carrying fillet welds. According to the structural (hot-spot) stress method, a single design curve can be used for the fatigue design of all the welded details in the same group. Thus, theoretically, it is possible to analyse a simpler joint in one group to generate the structural *S-N* curve for the group. This curve can then be used to predict the fatigue strength of a rather complex welded details in the same load-carrying weld group.

As an example, the web stiffener detail which was described in detail in Chapter 2 of this thesis, is a welded joint with non-load carrying fillet welds. However, an analytical analysis (e.g. SBFM analysis) of the critical weld toes for this detail is very difficult and computationally demanding due to the complex loading and geometry conditions and also the complicated fatigue crack shape and growth parameters. On the other hand, Type-X small scale specimens in this study represent another welded joint with non-load carrying fillet welds with a much simpler loading and geometry conditions and with well-known fatigue crack parameters. This simplicity made it possible to employ an analytical method (SBFM) to predict the fatigue behaviour of the small scale specimens under different treatment and loading conditions. The model predictions for the fatigue strength of as-welded and treated weld toes in Type-X specimens were presented in Figure 5.5 in terms of the nominal stress. The model predictions can be expressed in terms of the structural stress by multiplying the results (shifting the curve upward) by the structural stress coefficient for Type-X specimens (1.35) to derive the structural stress *S-N* curves.

Now, by using the structural stress concept, the obtained structural stress *S-N* curve can be used to estimate the fatigue strength of the web stiffener detail and, virtually, any welded detail with non-load carrying fillet welds. This idea is explored in this section.

Figure 5.7 presents the SBFM-based structural stress curve and the distortion-induced fatigue test results. In Figure 5.7a, the test results are expressed in terms of their extrapolated structural (hot-spot) stress ranges (reported in Chapter 2). As described in Chapter 3, the web stiffener detail is considered as a weld detail with load-transfer dominated behaviour and, thus, the extrapolation method is applicable. Figure 5.7b presents the test results in terms of the structural stress definition that was used in Chapter 3 to calculate the structural stress coefficient for a Type-X specimen based on the definition in [10]. In order to calculate the structural stress range based on the definition in [10] for the web stiffener details, the same finite element (FE) models that were described and discussed in Chapter 2 were used. The sectional forces and moments were then used to calculate the structural stress at the critical weld toe (also called the hot-spot). Structural stresses of 107.7 and 72.1 MPa were calculated for the unretrofitted and retrofitted specimens, respectively, for a 0.1 mm out of plane displacement (*d*) of the stiffener at a distance of 127 mm from the inside face of the near flange. The structural stresses for all of the distortion-induced fatigue test results were then re-calculated based on the FE results and the measured out of plane displacement (*d*) for each test. In all of the cases, the FE-based structural stress ranges were 20-30% larger than the extrapolated structural stresses. The updated web stiffener test results together with the analytical structural stress *S-N* curve for Type-X specimens are presented in Figure 5.7.

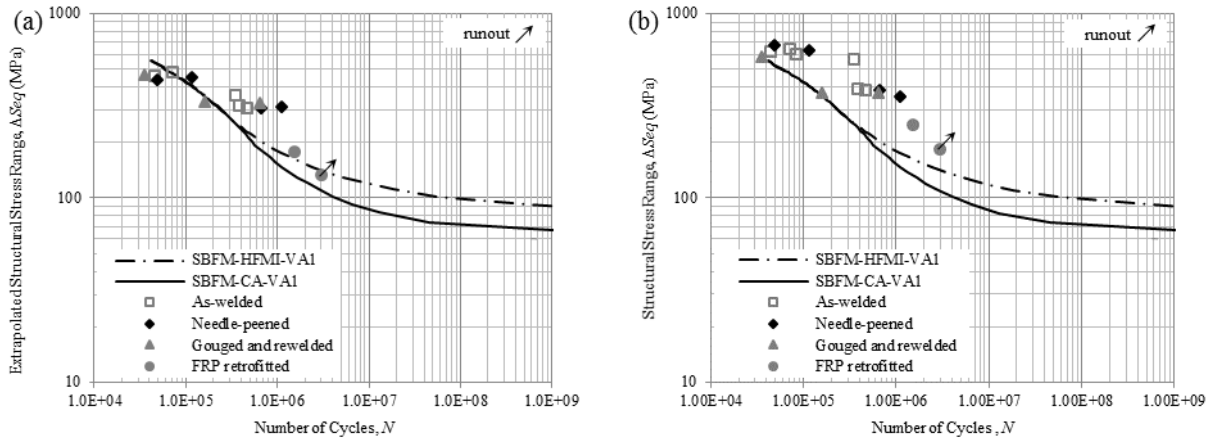

Figure 5.7: SBFM-based predictions for the web stiffener detail: (a) Extrapolated structural stress range; (b) FE-based structural stress range

As can be seen in this figure, using the SBFM predictions resulted in a close prediction of the fatigue strength of the web stiffener detail. Moreover, this approach correctly predicts the ineffectiveness of the used impact treatment method (needle peening in this case) at the tested stress ranges which were higher than 300 MPa. However, according to the model predictions, significant fatigue life increases can be expected at stress ranges lower than 100 MPa.

5.4 Comparison of Model Predictions and the Experimental Statistical Analysis

Figure 5.8 compares the SBFM model predictions and the experimental statistical data obtained in Chapter 3. According to this figure, the analytical predictions for the treated specimens were close to the *S-N* curves associated with a 95% survival probability, derived based on the experimental results. The SBFM predictions for the as-welded samples, however, were found to be closer to the mean test data, i.e. close to the S-N curves associated with 50% survival probability, for both specimen types.

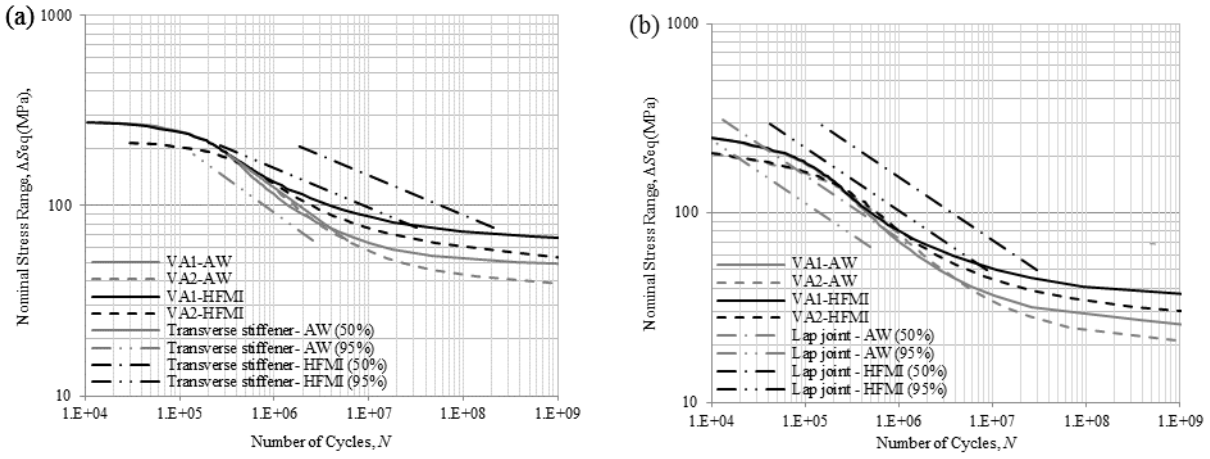

Figure 5.8: SBFM predictions and characteristic *S-N* curves: (a) Type-X; (b) Type-L

The analytical *S-N* curve slope (*m*) for the treated non-load carrying fillet welds was found to be in a good agreement with the statistical *m*. Therefore, *m*=5 was used to calculate the equivalent stress for the VA tests in the succeeding calculations. It should be noted that this assumption was only applied to those failures that occurred at treated toes. Root failures were excluded from the subsequent analysis since the SBFM analysis and parameters were only applicable to those fatigue cracks that initiate from and grow at the weld toe.

Figure 5.9 compares the SBFM model predictions and the suggested design *S-N* curves (in Chapter 3) for the VA fatigue behaviour of the treated weld toes for Type-X specimens based on $m = 5$. As can be seen in Figure 5.9, the analytical *S-N* curves for VA1 and VA2 histories become close to each other and lay on the FAT-182* curve for $N < 10^7$ when $m = 5$ is used. Both of the analytical *S-N* curves deviate from FAT-182* curve with a gradually increasing slope at around 20 million load cycles, which may indicate reaching to a fatigue threshold.

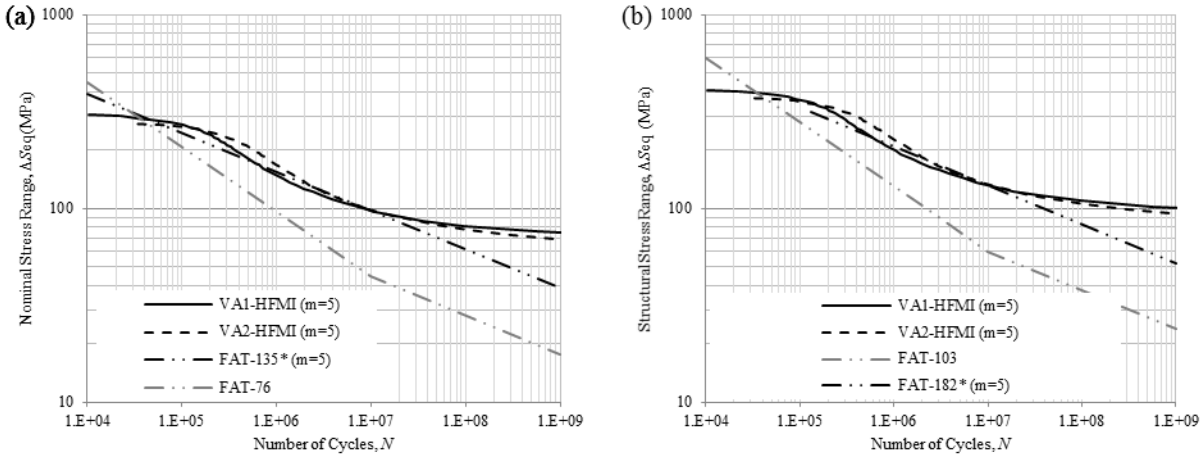

Figure 5.9: SBFM predictions and experimental *S-N* curves for non-load carrying treated weld toes: (a) nominal stress; (b) structural stress

5.5 Analytical Studies Performed with the SBFM Model

After evaluating the SBFM model *S-N* curves, the model was used to predict the fatigue performance of the treated weld toes under other realistic VA loading histories. This analysis was used to make design recommendations and provisions regarding the fatigue thresholds, the occasional tensile overloads, and the *S-N* fatigue design curves.

5.5.1 Simulations for Other Spans and Influence Lines

The analytical *S-N* curves for loading histories applicable to other influence lines and bridge spans were generated by conducting a number of simulations. A similar methodology was successfully used in [11] to study the adequacy of the current design provisions for the fatigue design of aluminum structures. Twenty (20) VA load histories were considered consisting of influence lines for five locations of four bridge spans of 15, 25, 40, and 60 m. These locations included midspan moment for 1- and 2-span girders, intermediate support moment for 2-span girders, and support reactions for 1- and 2-span girders.

The selected influence lines and spans were intended to cover a broad range of VA load history characteristics that are possible in bridge structures. Each in-service VA load history was generated by taking random samples of 1,000 trucks from the larger Ontario database [11]. As described in Chapter 2 and 3, the Ontario survey data included the axle weight and spacing data for 10,198 trucks measured in Ontario in 1995 [12]. Figure 5.10 shows the gross truck weight histogram based on this survey data. A similar histogram was used to generate realistic in-service loading histories in a number of previous studies, e.g. in [1, 11]. It should be noted that the static weights are used for the truck weights in this figure. Thus, to approximate the corresponding dynamic load effects, each axle load should be multiplied by an impact factor of 1.25, in accordance with CAN/CSA-S6 [13].

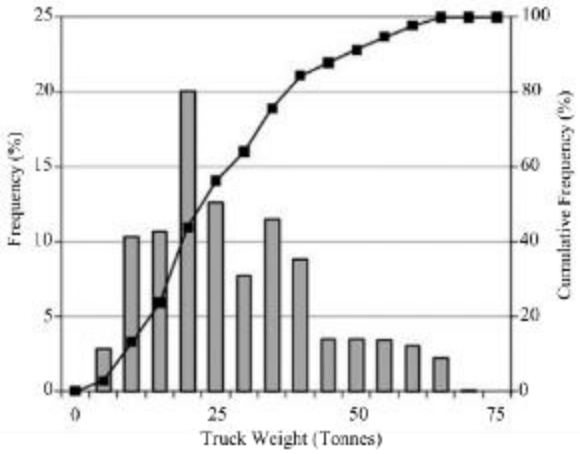

Figure 5.10: Truck weight histogram based on 1995 Ontario survey [1, 12]

The analysis results are presented in Figure 5.11 to Figure 5.13. In these figures, the results are plotted as envelopes in terms of the equivalent stress range, ΔS_{eq}, assuming m=5. The proposed design S-N curves for the as-welded and treated specimens, derived in Chapter 3, are also plotted in these figures for comparison purposes.

In Figure 5.11, the analysis results for the treated Type-X specimens are presented. The results show that both of the FAT-135* and FAT-182* design curves, for the nominal and structural stresses, respectively, lie below the VA loading envelopes for the most part. Based on the results, a significant fatigue life improvement cannot be claimed due to the HFMI treatment for $N < 10^6$ cycles. The VA loading envelopes exhibit a change of slope at around 200 million load cycles which may suggest approaching a fatigue threshold.

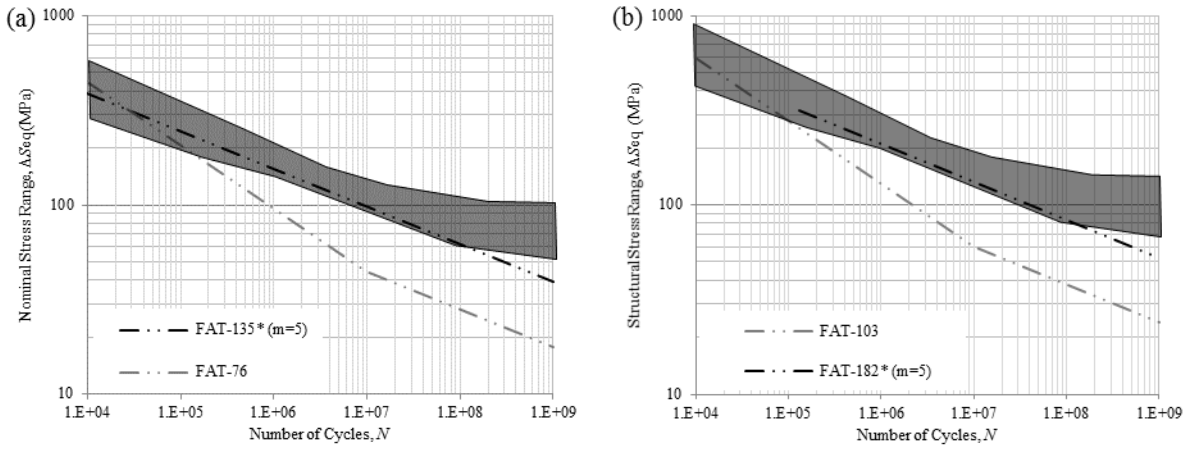

Figure 5.11: Results of the analysis of other spans and influence lines for Type-X: (a) nominal stress; (b) structural stress

The analysis results for the treated Type-L specimens are presented in Figure 5.12. The FAT-41 and 82 curves for the nominal stress approach (FAT-76 and 151 for the structural stress approach) represent design curves for the as-welded weld toe and as-welded weld root, respectively. Two other curves with $m = 5$ are also plotted in this figure including FAT-77* and FAT-143* which represent the treated weld toe. These curves were obtained based on the effective notch stress FAT-339* curve by considering the structural and effective notch stress coefficients (1.85 and 4.38, respectively).

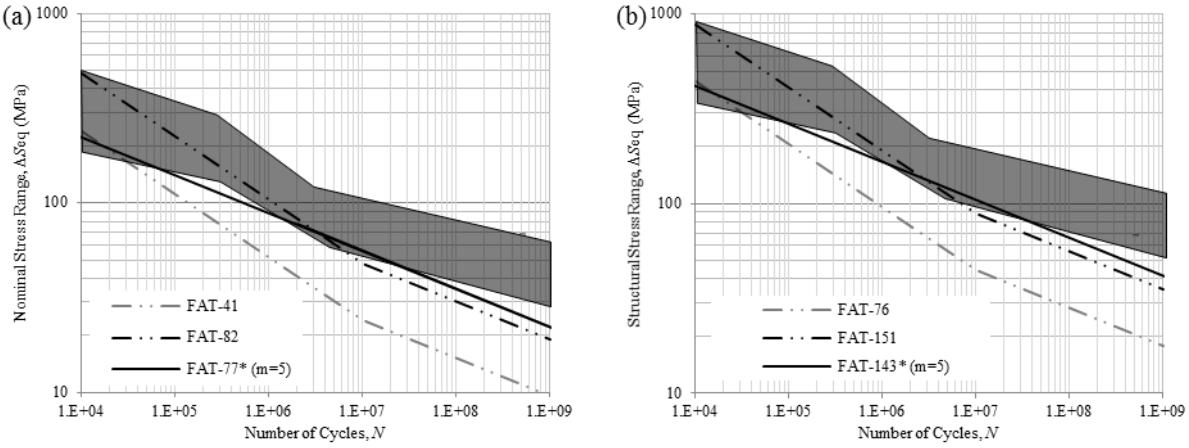

Figure 5.12: Results of analyses of other spans and influence lines for Type-L: (a) nominal stress; (b) structural stress

The results show that both of the nominal stress FAT-77* and structural stress FAT-143* design curves lie below the VA loading envelopes for the most part and provide a good design basis for the studied

load carrying weld toes. By comparing the VA loading envelopes and the design curves for root failures (FAT-82 and 151), it can be concluded that the failure mode changes from the failure at the treated toe for $N < 10^5$ cycles to the secondary mode of failure for $N > 10^6$. Consequently, a significant fatigue life improvement can be claimed due to the HFMI treatment for $N > 10^6$ cycles. The VA loading envelopes exhibit a change of slope at around 100 million load cycles. This change in the slope, that is not as significant as the change observed for Type-X specimens, may suggest approaching a fatigue threshold.

The analysis results for the treated weld toes for both types of specimens are presented in Figure 5.13 in terms of the effective notch stress range. Considering the width of the VA envelopes, the suggested FAT-339* design curve provides a good basis for the fatigue design of treated weld toes. Similar to the previous conclusions, significant fatigue life improvements can be expected due to HFMI treatment for $N > 10^6$.

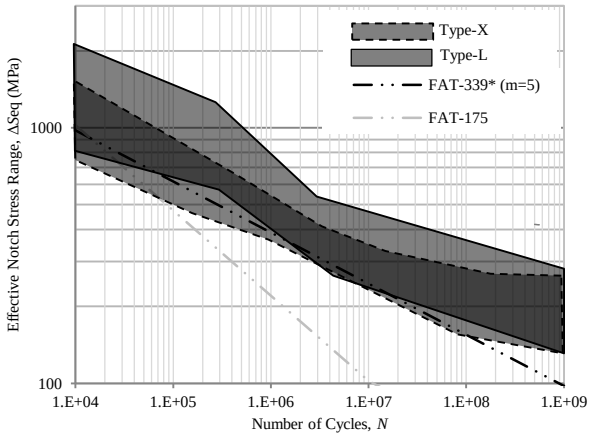

Figure 5.13: Results of analyses of other spans and influence lines for Type-X and L: effective notch stress

By considering the VA loading envelopes in Figure 5.11 to Figure 5.13, it can be concluded that the in-service VA loading characteristics have a significant influence on the analytical VA loading *S-N* curve. The shapes of the curves, however, followed a general *S*-shaped trend with two flatter parts in the low and high cycle domains with a steeper transitioning part in the middle. The flatter design *S-N* curve in the low cycle domain was found to have resulted from the severe overloads that were present in the VA load history, while the flatter portion in the high cycle domain is due to approaching a fatigue threshold. Overall, the *S-N* design curves with $m = 5$ were found to be the reasonably accurate design tools in all cases.

5.5.2 Scale Effect and Overload Studies

Among the factors that influence the VA results and were studied in [11], two factors were chosen for further investigation. These factors included increasing the plate thickness and introducing a particularly heavy truck at a regular frequency in the traffic history.

A new VA loading envelope was generated by increasing the thickness of the loaded plate from 9.5mm to 25mm. All other parameters for the weld detail, material properties, and the residual stress distribution were kept identical to the previous studies. The effects of varying these parameters were previously studied and discussed in detail in [3]. This change in the thickness resulted in an increase in the stress concentration factor (SCF) along the crack path. As presented in Figure 5.14(a), the result of this analysis is a slight downward shift in the VA loading envelope.

Another new VA loading envelope was produced with an overload truck which was introduced every1000th truck. As explained in [11], the overload truck had an axle configuration identical to the CAN/CSA-S6 CL-625 truck and a gross vehicle weight (GVW) of 93.75 kN. As shown in Figure 5.14(b), the addition of this overload truck resulted in a downward shift, more significant than the downward shift that resulted from the thickness increase, in the VA loading envelope.

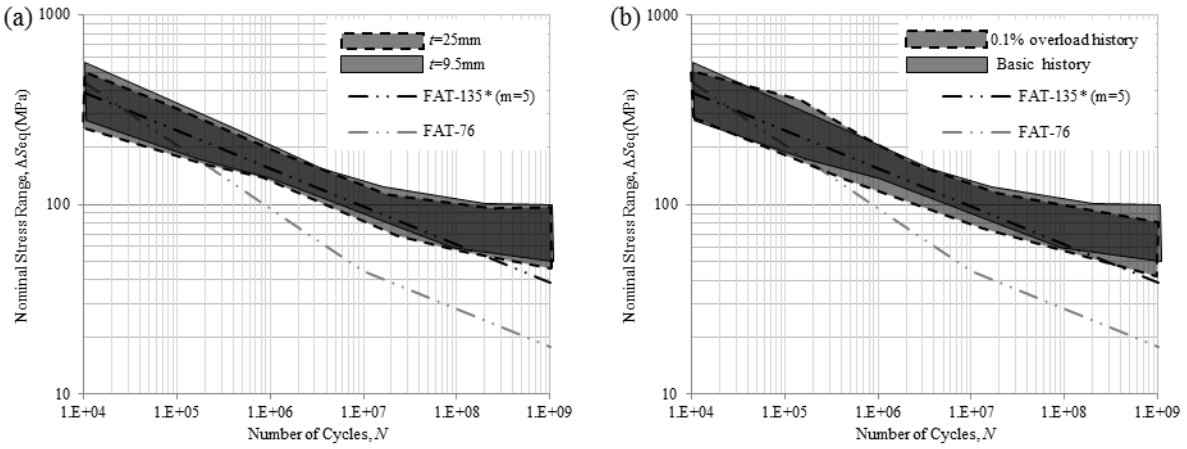

Figure 5.14: Thickness effect and overload study results: (a) thickness study; (b) overload study

5.5.3 Deign Recommendations

Based on the results presented in this chapter, the following recommendations were made regarding the fatigue design of HFMI treated weld toes.

- A set of single-sloped *S-N* design curves with $m = 5$ for the nominal, structural and effective stress design approaches are recommended for the prediction and design of the fatigue performance of the treated weld toes.
- A complete fatigue analysis of the welded joints with treated weld toes can only be performed by analysing the treated weld toe and other possible failure modes including the possible failures in weld root, weld throat, and base metal.
- A reliable and significant fatigue strength improvement cannot be expected under VA loading for $N < 10^6$.
- The repeating overloads play a key role in determining the effectiveness of the treatment. The test results also showed that a local stress approach is required for determining the maximum allowable stress. Within the scope of the current study, it is suggested the maximum structural tensile stress be limited to $1.15f_y$ (where f_y is the nominal yield strength of the loaded plate).

5.6 Conclusions

The influence of the HFMI treatment on the fatigue performance of structural welds under in-service variable amplitude (VA) loading conditions was predicted using a strain-based fracture mechanics (SBFM) model. The SBFM model predictions were validated by comparing the results to the fatigue test results two different types of test specimens under various loading conditions. Both as-welded and treated weld toes were considered. The model predictions were then used to generate the structural and effective notch stress *S-N* design curves which then can be used to predict the fatigue behaviour of the treated weld toes in other welded details.

A good agreement was also observed between the analytical and experimental *S-N* design curves when $m = 5$ was used to calculate the equivalent stress range under VA loading. Application of the SBFM model to consider several in-service loading histories that encompassed a wider range of influence lines and bridge spans showed that the predicted benefit of the HFMI treatment was highly dependent on the loading characteristics. Periodic tensile overloads were shown to be detrimental on the achieved level of the fatigue improvement. Increasing the plate thickness and the introduction periodic overload trucks in the analysis also resulted in a reduction in the fatigue performance of treated welds. It was concluded that the tensile overloads should be limited based on the local stress. It was then recommended to limit the maximum structural tensile stress to 1.15 times the yield strength of the material.

A set of design recommendations concerning the fatigue behaviour of treated weld toes in the middle to ultrahigh cycle domains were made based on the analytical results. A set of single-sloped *S-N* design curves were proposed for the nominal, structural, and the effective notch stress design of the treated weld toes. Finally, it was emphasized that a complete fatigue analysis of a welded joint with treated weld toes requires accounting for all of the possible failure modes.

Chapter 6

Summary, Conclusions, and Recommendations for Future Work

6.1 Summary and Conclusions

The summary and conclusions presented in this chapter is divided according to the four main areas of this research work including: (i) inhibiting distortion-induced fatigue damage in steel girders, (ii) high cycle fatigue behaviour of impact treated welds under in-service variable amplitude (VA) loading conditions, (iii) testing and measurements to determine model parameters for fatigue analysis, and (iv) fracture mechanics analysis of the as-received and impact treated welds.

6.1.1 Inhibiting Distortion-induced Fatigue Damage in Steel Girders

A web stiffener detail was fatigue tested under different cyclic loading conditions. As-welded specimens were tested, along with specimens retrofitted by grinding / rewelding and needle peening. The idea of retrofitting web stiffener ends in steel bridge girders susceptible to distortion-induced fatigue using adhesively-bonded fibre reinforced polymer (FRP) angles was also investigated. The following conclusions are drawn based on the results of these tests and the related analysis:

- The structural (hot-spot) stress approach was found to be a suitable method to identify the critical locations and predict the service life of as-welded and retrofitted fatigue specimens. When expressed in terms of the extrapolated structural (hot-spot) stress range, the fatigue lives for all the tested specimens lay above the FAT-100 design curve.
- The specimens retrofitted by grinding and rewelding had slightly lower fatigue lives than the as-received specimens. However, the initial design fatigue capacity (FAT-100) was restored in all cases. The shorter fatigue life was explained by the presence of higher tensile residual stresses that result from the multiple welding passes and the fact that the extra welding passes shortened the web gap in the repaired specimens, thus increasing the local stresses.
- Given that the structural stress ranges were higher than the material yield strength in most of the cases, the cyclic plasticity induced at these stress ranges resulted in residual stress relaxation. Thus, retrofitting by needle peening did not result in a significant increase in fatigue life for the tested stress ranges. It is expected that peening would be more effective at lower stress ranges. This conclusion was subsequently confirmed by fracture mechanics analysis.

- Implementing the FRP retrofit method resulted in significant fatigue life increases, with the amount depending primarily on the imposed loading range. The proposed retrofit method was found to be significantly more efficient than two other conventional repair methods. While the other methods focused on improving the local fatigue properties at the weld toe, the FRP retrofit method significantly reduced the stresses in the web gap region.
- Debonding within the adhesive-steel interface was found to be the most common failure mode when the FRP retrofit method was used, followed by failure of the FRP angles.
- The structural stress design curve was successfully used to estimate the fatigue life of the retrofitted specimens. Using the structural stress method, the efficiency of the FRP retrofit method can be determined using a coarse finite element (FE) model before implementation and by direct field measurements after implementation. This feature enables bridge owners to design FRP retrofits, predict their effectiveness, and evaluate them after implementation.
- The effects of a number of the varied geometric and mechanical parameters on the efficiency of the FRP retrofit method were studied using a finite element analysis. Greater improvements, in terms of reducing the structural stress, were achieved when stiffer FRP angles were used. Additionally, using a ductile structural adhesive is recommended to reduce the stresses in the adhesive layer and thus avoid sudden failures due to severe overloads.

6.1.2 High Cycle Fatigue Behaviour of Impact Treated Welds Under In-service VA Loading Conditions

A comprehensive variable amplitude (VA) fatigue testing program and analysis was conducted to address a number of concerns raised regarding the effectiveness of high frequency mechanical impact (HFMI) treatments for bridge welds in the high cycle domain. Different welded joint types representing load carrying and non-load carrying welds in steel structures were studied under two simulated in-service VA loading histories typical for highway bridges. Various approaches to predict the fatigue performance of the treated joints, especially in the long life domain, were evaluated using the generated test data. The results were compared with the current design recommendations and provisions. The following conclusions are drawn based on these experiments and analyses:

- For the specimens with non-load carrying welds (Type-X specimens), the HFMI treatment resulted in a significant fatigue strength improvement in all cases. The failure mode did not change after applying the treatment and consisted of weld toe failure in all cases.

- For the specimens with load carrying welds (Type-L specimens), treating the weld toe resulted in shifting the failure location from the weld toe to the weld root in most cases. Still, significant fatigue life improvements were achieved. The FAT-82 design curve is recommended for the nominal stress design of the treated Type-L detail.
- Constant amplitude fatigue limits (CAFL) of 110 and 48 MPa (nominal stress) for the treated Type-X and Type-L specimens, respectively, were found to be reasonable.
- The current design provisions to account for the benefit of impact treatment were found to be rather conservative. Based on a statistical analysis of the test results, $m = 5$ is recommended to determine the equivalent stress range for treated weld toes. Consequently, FAT-180* with $m = 5$ is proposed for the structural stress design of treated Type-X details, and FAT-339* with $m = 5$ is proposed for the effective notch stress design of treated weld toes.
- Within the scope of this study, which considered realistic loading histories for steel bridges, a frequent occurrence of load cycles with high mean stresses (high R ratios), as seen in the investigated VA2 loading history, did not seem to be a crucial factor.
- It is recommended that a local, e.g. structural stress, approach be used, rather than the nominal stress approach, to determine the magnitude of the maximum allowable overload (or underload) stress for impact treated welds beyond which the treatment effectiveness is significantly reduced due to residual stress relaxation. Based on the results of this study, it is recommended the maximum structural stress be limited to 1.15 times the yield strength.

6.1.3 Testing and Measurements to Determine Model Parameters for Fatigue Analysis

Several input parameters for the strain-based fracture mechanics model were determined through a comprehensive materials testing program, finite element (FE) analysis, and direct measurements. A recently developed experimental technique to derive the crack closure parameters and the effective crack growth curve with smooth specimen tests was employed for this phase of the research. The following conclusions were drawn based on these experiments and measurements:

- The crack growth parameters derived from the smooth specimen tests were found to be in good agreement with the results of direct crack growth tests on compact tension (CT) specimens.
- Microhardness measurements were conducted on untreated and treated heat affect zone (HAZ) material. HFMI treatment resulted in a significant increase in the near-surface hardness. The hardness decreased rapidly below the surface to that of the as-welded HAZ at a depth of ~1.2

mm. Compressed grain boundaries observed in the images of the near surface microstructure of the impact treated welds confirmed the effect of the treatment in this region.

- The as-received and impact treated weld toe geometries were measured using silicon impressions and also using a 3D laser scanner. The finite element (FE) method was then used to determine the stress concentration factors (SCFs) at the weld toes. In general, it was found that the two techniques for measuring weld toe geometry gave similar results. It is believed that the laser scanning technique had not been used previously. It has the advantage of being rapid and it is archivable, resulting in an electronic record of the weld toe geometry after treatment. In general, impact treatment results in a slight reduction of the SCF at the weld toe.
- X-ray diffraction measurements revealed that the impact treatment resulted in a significant change in the residual stress distribution through the specimen thickness. FE analysis was also used to evaluate the residual stress profiles induced by peening treatments, and the results were found to compare well with the residual stress measurements.

6.1.4 Fracture Mechanics Analysis of the As-Received and Impact Treated Welds

A strain-based fracture mechanics (SBFM) model was used to study the influence of HFMI treatment on the fatigue performance of structural welds under in-service variable amplitude (VA) loading conditions. The model predictions were validated by comparing the results to the fatigue test results of two different types of test specimens under various loading conditions. The model predictions were then used to generate design curves. Based on this work, the following conclusions are drawn:

- Generally, a good agreement was observed between the model predictions and the test results. The SBFM model closely predicted the fatigue behaviour of the as-welded specimens of both specimen types. While a very good agreement was also observed between the analytical and experimental results for the constant amplitude (CA) fatigue tests, the specimens fatigue lives under VA loadings were conservatively underpredicted to some extent in the long life regime. However, several important trends were still correctly predicted by the model.
- A good agreement was observed between the analytical and experimental *S*-*N* design curves when $m = 5$ was used to calculate the equivalent stress range under VA loading.
- The SBFM model was used to study the fatigue behaviour of treated welds under several other in-service loading histories. It was shown showed that the predicted benefit of the HFMI

treatment was highly dependent on the loading characteristics. In particular, periodic tensile overloads were shown to decrease the achieved level of the fatigue improvement.

- A set of single-sloped *S-N* design curves with $m = 5$ were proposed for the nominal, structural, and the effective notch stress design of the treated weld toes. These curves include FAT^{*}-135 and FAT^{*}-182 for the nominal and structural stress design of non-load carrying treated weld toes (respectively), FAT^{*}-77 and FAT^{*}-143 for the nominal and structural stress design of load carrying treated weld toes (respectively), and FAT^{*}-339 for the effective notch stress design of treated weld toes.
- It is recommended the maximum structural stress be limited to 1.15 times the yield strength.
- It is highlighted that a complete fatigue analysis of a welded joint with treated weld toes requires accounting for all of the possible failure modes, including weld root and base metal failure.

6.2 Recommendations for Future Work

The following sections list recommendations for future work resulting from the research presented in this thesis, again subdivided into the same four themes as the summary and conclusions.

6.2.1 Inhibiting Distortion-induced Fatigue Damage in Steel Girders

- Further research is recommended to assess the performance of the FRP retrofit on full-scale girders, including laboratory testing of full-scale girder specimens, FE analysis of actual bridges, and field trials.
- Further work is needed to develop guidelines for the fatigue verification and design of the FRP angle and adhesive. The effectiveness of the FRP angle retrofit at extreme high and low temperatures needs to be studied, as the adhesive properties may vary disadvantageously under severe temperature conditions.
- An analytical and experimental study of debonding in the adhesive layer is recommended.
- The proposed FRP retrofit method reduces the stresses in the web gap region, and thus, has the potential to be used in conjunction with other fatigue improvement techniques which focus on improving the local fatigue properties at the weld toe. Impact treatments are known to be highly effective in extending the fatigue lives of welded components, and are found to be particularly effective at low stress ranges. Future study of this possibility is recommended.

6.2.2 High Cycle Fatigue Behaviour of Impact Treated Welds under In-service VA Loading Conditions

- Further research in the field of high cycle fatigue behaviour is recommended including considering other common weld joints and other relevant VA histories. In particular, VA histories with severe compressive underloads are recommended for future study.
- The fatigue tests reported in this thesis were conducted on mild steel samples with a plate thicknesses of 9.5 mm (3/8”). Further research is recommended to investigate scale and material strength effects on the results and conclusions of the presented research.

6.2.3 Testing and Measurements to Determine Model Parameters for Fatigue Analysis

- Conducting a similar materials testing program on other steels is recommended for further validation of the methodology described in this thesis and also to contribute to the available data for various steel grades and applications. Further investigation of the correlation between the hardness of the steel and the crack closure parameters is also recommended.
- Further extension of the FE analysis of HFMI treatment is recommended. A 2D dynamic FE analysis of multiple indentations can simulate the HFMI treatment process more precisely. Residual stresses due to welding can also be added to the model for further accuracy. Such an FE model could be used to develop an empirical model or another way to quantify the benefits of applying residual stress-based post-weld treatments. Having a simple empirical model for quantifying the benefit of applying residual stress-based post-weld treatments under load will help in determining the fatigue life of repaired components. For instance, using such a model and considering the geometry of the welded component, a reasonably accurate on-site estimate can be made for a treatment-induced beneficial residual stress magnitude and distribution by measuring the groove depth left by an HFMI treatment tool.
- It is expected that an optimum indentation depth exists for each steel type beyond which further treatment does not result in increasing the beneficial near surface compressive residual stresses. Further FE and experimental investigations of this idea is recommended.

6.2.4 Fracture Mechanics Analysis of the As-Received and Impact Treated Welds

- Further investigation of the systematic under-prediction for the treated welds under VA loading is recommended. In particular, the effect of assuming a plane strain state should be further

studied. The effects of varying the crack front ratio for different treatment and fatigue testing conditions should also be considered in using the fracture mechanics model.

- The strain-based fracture mechanics model is a powerful tool that facilitates simulation of the fatigue behaviour of various welded details under any loading condition. Further development of this model is recommended. For example, the model can be modified to consider all modes of fatigue failure (including toe, root, and subsurface failures) simultaneously.

References

Chapter 1

[1] R.J. Connor, J.W. Fisher, Identifying effective and ineffective retrofits for distortion fatigue cracking in steel bridges using field instrumentation, J. Bridge Eng. 11 (2006) 745-752.

[2] M. Hirt, J.P. Lebel, Steel bridges: conceptual and structural design of steel and steel-concrete composite bridges, EPFL Press, 2013.

[3] Canadian Standards Association, G40.20-13/G40.21-13 - General requirements for rolled or welded structural quality steel / Structural quality steel, CSA, 2013.

[4] A. Hobbacher, IIW recommendations for fatigue design of welded joints and components, WRC Bulletin 520, The Welding Research Council, New York, 2009.

[5] P.J. Haagensen, S.J. Maddox, IIW recommendations on post weld fatigue life improvement of steel and aluminium structures, International Institute of Welding, Paris, 2013.

[6] Canadian Standards Association (CSA), Canadian highway bridge design code (2006).

[7] K. Ghahremani, S. Walbridge, T. Topper, Inhibiting distortion-induced fatigue damage in steel girders by using FRP angles, J. Bridge Eng. DOI: 10.1061/(ASCE)BE.1943-5592.0000678 (2014).

[8] K. Ghahremani, S. Walbridge, T. Topper, Fatigue retrofitting of web stiffeners in steel bridges using pultruded FRP sections , Structures Congress 2014 – Proc. 2014 Structures Congress (2014) 376-385.

Chapter 2

[1] R.J. Connor, J.W. Fisher, Identifying effective and ineffective retrofits for distortion fatigue cracking in steel bridges using field instrumentation, J. Bridge Eng. 11 (2006) 745-752.

[2] H. Hassel L., A. Hartman S., C. Bennett R., A. Matamoros B., Distortion-induced fatigue in steel bridges: causes, parameters, and fixes (2010) 471-483.

[3] Y. Zhao, K.W.M. Roddis, Fatigue behavior and retrofit investigation of distortion-induced web gap cracking, J. Bridge Eng. 12 (2007) 737-745.

[4] K. Ghahremani, A. Sadhu, S. Walbridge, S. Narasimhan, Fatigue testing and structural health monitoring of retrofitted web stiffeners on steel highway bridges, Transportation Research Record (2013) 27-35.

[5] J. Fisher, J. Jian, D. Wagner, B. Yen, Distortion-induced fatigue cracking in steel bridges, National Cooperative Highway Research Program Report # 336 (1990).

[6] A. Hartman, C. Bennett, A. Matamoros, S. Rolfe, Innovative retrofit technique for distortion-induced fatigue cracks in steel girder web gaps, Bridge Structures. 9 (2013) 57-71.

[7] E. Niemi, W. Fricke, S.J. Maddox, Fatigue analysis of welded components: designer's guide to the structural hot-spot stress approach, CRC Boca Raton, Fla., 2006.

[8] R. Sen, L. Liby, G. Mullins, K. Spillett, Strengthening steel composite beams with CFRP laminates, Proceedings of the Materials Engineering Conference. 2 (1996) 1601-1607.

[9] R. Sen, L. Liby, G. Mullins, Strengthening steel bridge sections using CFRP laminates, Compos. Part B:Eng. 32 (2001) 309-322.

[10] Y.J. Kim, K.A. Harries, Fatigue behavior of damaged steel beams repaired with CFRP strips, Eng. Struct. 33 (2011) 1491-1502.

[11] T.C. Miller, M.J. Chajes, D.R. Mertz, J.N. Hastings, Strengthening of a steel bridge girder using CFRP plates, J. Bridge Eng. 6 (2001) 514-522.

[12] P. Colombi, A. Bassetti, A. Nussbaumer, Analysis of cracked steel members reinforced by pre-stress composite patch, Fatigue and Fracture of Engineering Materials and Structures. 26 (2003) 59-66.

[13] S.C. Jones, S.A. Civjan, Application of fiber reinforced polymer overlays to extend steel fatigue life, J. Composite Constr. 7 (2003) 331-338.

[14] S. Walbridge, K. Soudki, F. Vatandoost, Fatigue retrofitting of welded steel cover plates using Pre-stressed carbon fibre reinforced polymer strips, Structural Engineering International: Journal of the International Association for Bridge and Structural Engineering (IABSE). 21 (2011) 279-284.

[15] B.N. Kaan, F. Alemdar, C.R. Bennett, A. Matamoros, R. Barrett-Gonzalez, S. Rolfe, Fatigue enhancement of welded details in steel bridges using CFRP overlay elements, J. Composite Constr. 16 (2012) 138-149.

[16] A.M. Okeil, Y. Bingol, M.R. Ferdous, Novel technique for inhibiting buckling of thin-walled steel structures using pultruded glass FRP sections, J. Composite Constr. 13 (2009) 547-557.

[17] D. Fernando, T. Yu, J.G. Teng, X.L. Zhao, CFRP strengthening of rectangular steel tubes subjected to end bearing loads: Effect of adhesive properties and finite element modelling, Thin-Walled Structures. 47 (2009) 1020-1028.

[18] S. El-Tawil, E. Ekiz, S. Goel, S.-. Chao, Retraining local and global buckling behavior of steel plastic hinges using CFRP, Journal of Constructional Steel Research. 67 (2011) 261-269.

[19] J.G. Teng, T. Yu, D. Fernando, Strengthening of steel structures with fiber-reinforced polymer composites, Journal of Constructional Steel Research. 78 (2012) 131-143.

[20] A.M. Okeil, G. Broussard, Efficiency of inhibiting local buckling using pultruded FRP sections (2012), Proc., 91st Transportation Research Board Annual Meeting, Transportation Research Board, Washington, DC.

[21] A. Shaat, A.Z. Fam, Slender steel columns strengthened using high-modulus CFRP plates for buckling control, J. Composite Constr. 13 (2009) 2-12.

[22] K.A. Harries, A.J. Peck, E.J. Abraham, Enhancing stability of structural steel sections using FRP, Thin-Walled Structures. 47 (2009) 1092-1101.

[23] D. Schnerch, M. Dawood, S. Rizkalla, E. Sumner, K. Stanford, Bond behavior of CFRP strengthened steel structures, Adv. Struct. Eng. 9 (2006) 805-817.

[24] D. Schnerch, K. Stanford, E.A. Sumner, S. Rizkalla, Strengthening steel structures and bridges with high-modulus carbon fiber-reinforced polymers: Resin selection and scaled monopole behavior, Transportation Research Record (2004) 237-245.

[25] K. Ghahremani, S. Walbridge, Fatigue testing and analysis of peened highway bridge welds under in-service variable amplitude loading conditions, Int. J. Fatigue. 33 (2011) 300-312.

[26] P.J. Haagensen, S.J. Maddox, IIW recommendations on post weld fatigue life improvement of steel and aluminium structures, International Institute of Welding, Paris, 2013.

[27] Fibergrate, Engineering specifcation pultruded Dynaform fiberglass structural shapes (2012).

[28] Sika, Product data sheet for Sika AnchorFix-3CA/ Sika AnchorFix-4CA (2012).

[29] Sika, Product data sheet for SikaFast-3131S (2012).

Chapter 3

[1] J.D. Harrison, Further techniques for improving the fatigue strength of welded joints, Brit Weld J. 11 (1966) 642-647.

[2] S.J. Maddox, Improving the fatigue strength of welded joints by peening, Metal Construction. 17 (1985) 220-224.

[3] S. Roy, J.W. Fisher, B.T. Yen, Fatigue resistance of welded details enhanced by ultrasonic impact treatment (UIT), Int. J. Fatigue. 25 (2003) 1239-1247.

[4] X. Cheng, J.W. Fisher, H.J. Prask, T. Gnäupel-Herold, B.T. Yen, S. Roy, Residual stress modification by post-weld treatment and its beneficial effect on fatigue strength of welded structures, Int. J. Fatigue. 25 (2003) 1259-1269.

[5] K. Ghahremani, S. Walbridge, Fatigue testing and analysis of peened highway bridge welds under in-service variable amplitude loading conditions, Int. J. Fatigue. 33 (2011) 300-312.

[6] B. Vilhauer, C.R. Bennett, A.B. Matamoros, S.T. Rolfe, Fatigue behavior of welded coverplates treated with Ultrasonic Impact Treatment and bolting, Eng. Struct. 34 (2012) 163-172.

[7] H.C. Yildirim, G.B. Marquis, Overview of fatigue data for high frequency mechanical impact treated welded joints, Weld. World. 56 (2012) 82-96.

[8] H.C. Yildirim, G.B. Marquis, A round robin study of high-frequency mechanical impact (HFMI)-treated welded joints subjected to variable amplitude loading, Weld. World. 57 (2013) 437-447.

[9] R. Tehrani Yekta, K. Ghahremani, S. Walbridge, Effect of quality control parameter variations on the fatigue performance of ultrasonic impact treated welds, Int. J. Fatigue. 55 (2013) 245-256.

[10] G. Marquis, Z. Barsoum, Fatigue strength improvement of steel structures by high-frequency mechanical impact: Proposed procedures and quality assurance guidelines, Weld. World. 58 (2014) 19-28.

[11] K. Ghahremani, M. Safa, J. Yeung, S. Walbridge, C. Haas, S. Dubois, Quality assurance for high frequency mechanical impact (HFMI) treatment of welds using 3d laser scanning technology, Weld. World. 56 (2014) 391-400.

[12] S. Roy, J.W. Fisher, Modified AASHTO design S-N curves for post-weld treated weld details, Journal of Bridge Structures - Assessment, Design and Construction. 2 (2006) 207-222.

[13] Y. Kudryavtsev, J. Kleiman, A. Lugovskoy, L. Lobanov, V. Knysh, O. Voitenko, G. Prokopenko, Rehabilitation and repair of welded elements and structures by Ultrasonic Peening, Weld. World. 51 (2007) 47-53.

[14] S.J. Maddox, M.J. Doré, S.D. Smith, A case study of the use of ultrasonic peening for upgrading a welded steel structure, Weld. World. 55 (2011) 56-67.

[15] K. Ghahremani, S. Walbridge, Predicting the effect of post-weld treatments applied under load on the fatigue performance of welds in existing steel bridges, Proc., 8th International Conference on Short and Medium Span Bridges (2012) 1141-1151.

[16] K. Ghahremani, S. Walbridge, Fatigue Testing and Analysis of As-Welded and Retrofitted Web Stiffeners in Steel Highway Bridges, Structures Congress 2012 - Proc. 2012 Structures Congress (2012) 648-656.

[17] H.C. Yildirim, G.B. Marquis, Fatigue strength improvement factors for high strength steel welded joints treated by high frequency mechanical impact, Int. J. Fatigue. 44 (2012) 168-176.

[18] K. Ghahremani, A. Sadhu, S. Walbridge, S. Narasimhan, Fatigue testing and structural health monitoring of retrofitted web stiffeners on steel highway bridges, Transportation Research Record (2013) 27-35.

[19] E. Mikkola, M. Doré, M. Khurshid, Fatigue strength of HFMI treated structures under high R-ratio and variable amplitude loading, Procedia Engineering. 66 (2013) 161-170.

[20] Canadian Standards Association (CSA), Welded steel construction (metal arc welding): CSA standard W59-03;, 2003.

[21] American Welding Society (AWS), Structural welding code: AWS standard D1.1/D1.1M, 2004.

[22] P.J. Haagensen, S.J. Maddox, IIW recommendations on post weld fatigue life improvement of steel and aluminium structures, International Institute of Welding, Paris, 2013.

[23] M. Khurshid, Z. Barsoum, G. Marquis, Behavior of compressive residual stresses in high strength steel welds induced by high frequency mechanical impact treatment, J. Pressure Vessel Technol. Trans. ASME. 136 (2014).

[24] C.M. Sonsino, S.J. Maddox, A. Hobbacher, Fatigue life assessment of welded joints under variable amplitude loading - State of present knowledge and recommendations for fatigue design regulations, Weld. World. 48 (2004) 87-102.

[25] H. Agerskov, Fatigue in steel structures under random loading, Journal of Constructional Steel Research. 53 (2000) 283-305.

[26] M.A. Miner, Cumulative damage in fatigue, Journal of Applied Mechanics. 12 (1945) A159-A164.

[27] G. Marquis, Failure modes and fatigue strength of improved HSS welds, Eng. Fract. Mech. 77 (2010) 2051-2062.

[28] American Association of State Highway and Transportation Officials (AASHTO), LRFD bridge construction specifications, Washington (DC), 2008.

[29] A. Hobbacher, IIW recommendations for fatigue design of welded joints and components, WRC Bulletin 520, The Welding Research Council, New York, 2009.

[30] E. Niemi, W. Fricke, S.J. Maddox, Fatigue analysis of welded components: designer's guide to the structural hot-spot stress approach, CRC Boca Raton, Fla., 2006.

[31] Ministry of Transportation of Ontario, Truck Weight Survey (1995).

[32] K. Ghahremani, S. Walbridge, T. Topper, Inhibiting distortion-induced fatigue damage in steel girders by using FRP angles, J. Bridge Eng. DOI: 10.1061/(ASCE)BE.1943-5592.0000678 (2014).

[33] Canadian Standards Association (CSA), Canadian highway bridge design code: CAN/CSA-S6-06, 2006.

[34] E. Niemi, G. Marquis, Introduction to the structural stress approach to fatigue analysis of plate structures, Proc. the IIW Fatigue Seminar (2002) 73-90.

[35] D. Radaj, C.M. Sonsino, W. Fricke, Recent developments in local concepts of fatigue assessment of welded joints, Int. J. Fatigue. 31 (2009) 2-11.

[36] W. Fricke, Recommended hot-spot analysis procedure for structural details of ships and FPSOs based on round-robin FE analyses, Int. J. Offshore Polar Eng. 12 (2002) 40-47.

[37] O. Doerk, W. Fricke, C. Weissenborn, Comparison of different calculation methods for structural stresses at welded joints, Int. J. Fatigue. 25 (2003) 359-369.

[38] P. Dong, A structural stress definition and numerical implementation for fatigue analysis of welded joints, Int. J. Fatigue. 23 (2001) 865-876.

[39] A. Chattopadhyay, G. Glinka, M. El-Zein, J. Qian, R. Formas, Stress analysis and fatigue of welded structures, Weld. World. 55 (2011) 2.

[40] R. Tovo, P. Lazzarin, Relationships between local and structural stress in the evaluation of the weld toe stress distribution, Int. J. Fatigue. 21 (1999) 1063-1078.

Chapter 4

[1] M. El-Zeghayar, T.H. Topper, F.A. Conle, J.J.F. Bonnen, Modeling crack closure and damage in variable amplitude fatigue using smooth specimen fatigue test data, Int. J. Fatigue. 33 (2011) 223-231.

[2] M. El-Zeghayar, T.H. Topper, K.A. Soudki, A model of crack opening stresses in variable amplitude loading using smooth specimen fatigue test data for three steels, Int. J. Fatigue. 33 (2011) 1337-1350.

[3] Canadian Standards Association, G40.20-13/G40.21-13 - General requirements for rolled or welded structural quality steel / Structural quality steel, CSA, 2013.

[4] K. Ghahremani, S. Walbridge, Fatigue testing and analysis of peened highway bridge welds under in-service variable amplitude loading conditions, Int. J. Fatigue. 33 (2011) 300-312.

[5] American Society for Testing and Materials, ASTM E647 - 13 Standard test method for measurement of fatigue crack growth rates, ASTM, 2013.

[6] M.A. Pompetzki, R.H. Saper, T.H. Topper, Software for high frequency control of variable amplitude fatigue tests, Can. Metall. Q. 25 (1986) 181-194.

[7] American Society for Testing and Materials, ASTM E8/E8M Standard test methods for tension testing of metallic materials, ASTM, 2013.

[8] M. Khalil, T.H. Topper, Prediction and correlation of the average crack-opening stress with service load cycles, Int. J. Fatigue. 25 (2003) 661-670.

[9] T.H. Topper, T.S. Lam, Effective strain-fatigue life data for variable amplitude fatigue, Int. J. Fatigue. 19 (1997) S137-S143.

[10] T.S. Lam, T.H. Topper, F.A. Conle, Derivation of crack closure and crack growth rate data from effective-strain fatigue life data for fracture mechanics fatigue life predictions, Int. J. Fatigue. 20 (1998) 703-710.

[11] T.H. Topper, D.L. Du Quesnay, M.A. Pompetzki, R. Jurcevic, A crack closure based model for mean stress and overload effects on fatigue damage, International Symposium on Fatigue Damage Measurement and Evaluation under Complex Loadings (1991).

[12] D.L. DuQuesnay, T.H. Topper, M.T. Yu, M.A. Pompetzki, The effective stress range as a mean stress parameter, Int. J. Fatigue. 14 (1992) 45-50.

[13] A.A. Dabayeh, T.H. Topper, Changes in crack-opening stress after underloads and overloads in 2024-T351 aluminium alloy, Int. J. Fatigue. 17 (1995) 261-269.

[14] D.L. DuQuesnay, Fatigue damage accumulation in metals subjected to high mean stress and overload cycles, Fatigue Damage Accumulation in Metals Subjected to High Mean Stress and Overload Cycles (1991).

[15] M. Khalil, T.H. Topper, Prediction of crack-opening stress levels for 1045 as-received steel under service loading spectra, Int. J. Fatigue. 25 (2003) 149-157.

[16] W. Elber, The significance of fatigue crack closure, Damage tolerance in aircraft structures, ASTM STP 486 (1971).

[17] M.H. El Haddad, K.N. Smith, T.H. Topper, Fatigue crack propagation of short cracks, J. Eng. Mater. Technol. Trans. ASME. 101 (1979) 42-46.

[18] A.J. McEvily, Current aspects of fatigue. Fatigue crack propagation of short cracks, Fatigue 1977 Conference (1977) 1-9.

[19] American Society for Testing and Materials, ASTM E3 - 11 Standard guide for preparation of metallographic specimens, ASTM, 2011.

[20] American Society for Testing and Materials, ASTM E384 Standard Test method for knoop and vickers hardness of materials, ASTM, 2011.

[21] R. Tehrani Yekta, K. Ghahremani, S. Walbridge, Effect of quality control parameter variations on the fatigue performance of ultrasonic impact treated welds, Int. J. Fatigue. 55 (2013) 245-256.

[22] R. Tehrani Yekta, Acceptance criteria for ultrasonic impact treatment of highway steel bridges, University of Waterloo MASc. Thesis (2012).

[23] K. Ghahremani, M. Safa, J. Yeung, S. Walbridge, C. Haas, S. Dubois, Quality Assurance for High Frequency Mechanical Impact (HFMI) Treatment of Welds Using 3D Laser Scanning Technology, Welding in the World (2014).

[24] Creaform, Handy scan 3D handheld 3D Scanner, Technical Specification (2013).

[25] K. Ghahremani, S. Walbridge, Fatigue testing and finite element analysis of bridge welds retrofitted by peening under load, Structures Congress 2012 – Proc. 2012 Structures Congress (2012) 648-656.

[26] K. Ghahremani, Predicting the effectiveness of post-weld treatments applied under load, University of Waterloo MASc. Thesis (2010).

[27] American Society for Testing and Materials, ASTM E915 Standard test method for verifying the alignment of x-ray diffraction instrumentation for residual stress measurement, ASTM, 2010.

Chapter 5

[1] K. Ghahremani, S. Walbridge, Fatigue testing and analysis of peened highway bridge welds under in-service variable amplitude loading conditions, Int. J. Fatigue. 33 (2011) 300-312.

[2] S. Walbridge, Fatigue analysis of post-weld fatigue improvement treatments using a strain-based fracture mechanics model, Eng. Fract. Mech. 75 (2008) 5057-5071.

[3] R. Tehrani Yekta, K. Ghahremani, S. Walbridge, Effect of quality control parameter variations on the fatigue performance of ultrasonic impact treated welds, Int. J. Fatigue. 55 (2013) 245-256.

[4] D.L. DuQuesnay, Fatigue damage accumulation in metals subjected to high mean stress and overload cycles, Fatigue Damage Accumulation in Metals Subjected to High Mean Stress and Overload Cycles (1991).

[5] M. Khalil, T.H. Topper, Prediction of crack-opening stress levels for 1045 as-received steel under service loading spectra, Int. J. Fatigue. 25 (2003) 149-157.

[6] A.A. Dabayeh, A.J. Berube, T.H. Topper, An experimental study of the effect of a flaw at a notch root on the fatigue life of cast Al 319, Int. J. Fatigue. 20 (1998) 517-530.

[7] G. Shen, G. Glinka, Determination of weight functions from reference stress intensity factors, Theor. Appl. Fract. Mech. 15 (1991) 237-245.

[8] A. Bäumel, T. Seeger, Materials data for cyclic loading – supplement 1, Elsevier Science Publishing Company, New York:, 1990.

[9] K. Ghahremani, A. Sadhu, S. Walbridge, S. Narasimhan, Fatigue testing and structural health monitoring of retrofitted web stiffeners on steel highway bridges, Transportation Research Record (2013) 27-35.

[10] P. Dong, A structural stress definition and numerical implementation for fatigue analysis of welded joints, Int. J. Fatigue. 23 (2001) 865-876.

[11] R. Coughlin, S. Walbridge, Fatigue testing and analysis of aluminum welds under in-service highway bridge loading conditions, J. Bridge Eng. 17 (2012) 409-419.

[12] Ministry of Transportation of Ontario, Truck weight survey (1995).

[13] Canadian Standards Association (CSA), Canadian highway bridge design code (2006).